



Rodrigo Luís Formosinho Castello Branco

**Development of Momentum Flux Parameters and
Stability Analysis of a 1D Two-Fluid Model for Vertical
Annular Flows**

Dissertação de Mestrado

Dissertation presented to the Programa de Pós-Graduação em Engenharia Mecânica of PUC-Rio in partial fulfillment of the requirements for the degree of Mestre em Engenharia Mecânica.

Advisor: Prof. Angela Ourivio Nieckele

Co-Advisor: Dr. João Neuenschwander Escosteguy
Carneiro

Rio de Janeiro
February 2022



Rodrigo Luís Formosinho Castelo Branco

**Development of Momentum Flux Parameters and
Stability Analysis of a 1D Two-Fluid Model for Vertical
Annular Flows**

Dissertation presented to the Programa de Pós-Graduação em Engenharia Mecânica of PUC-Rio in partial fulfillment of the requirements for the degree of Mestre em Engenharia Mecânica. Approved by the Examination Committee.

Prof. Angela Ourivio Nieckele

Advisor

Departamento de Engenharia Mecânica – PUC-Rio

Dr. João Neuenschwander Escosteguy Carneiro

Co-advisor

ISDB FlowTech

Dr. Roel Belt

Total France

Prof. Igor Braga De Paula

Departamento de Engenharia Mecânica – PUC-Rio

Rio de Janeiro, February 25th, 2022

Rodrigo Luís Formosinho Castello Branco

The author graduated in Mechanical Engineering from the Pontifícia Universidade Católica do Rio de Janeiro (PUC-Rio) in 2019. Has since been working as a graduate student at the Computational Fluid Dynamics Group of the Department of Mechanical Engineering of PUC-Rio under the supervision of Prof. Angela Ourivio Nieckele. The lines of research include 1D and 3D modeling of multiphase flows and hydrate plug removal simulations.

Bibliographic data

Castello Branco, Rodrigo Luís Formosinho

Development of momentum flux parameters and stability analysis of a 1D Two-Fluid Model for vertical annular flows / Rodrigo Luís Formosinho Castello Branco ; advisor: Angela Ourivio Nieckele ; co-advisor: João Neuenschwander Escosteguy Carneiro. – 2022.

151 f. : il. color. ; 30 cm

Dissertação (mestrado)—Pontifícia Universidade Católica do Rio de Janeiro, Departamento de Engenharia Mecânica, 2022.

Inclui bibliografia

1. Engenharia Mecânica – Teses. 2. Modelo de Dois-Fluidos 1D. 3. escoamento anular vertical. 4. Parâmetro de fluxo de momentum. 5. Análise de estabilidade. 6. Avaliação de relações de fechamento. I. Nieckele, Angela Ourivio. II. Carneiro, João Neuenschwander Escosteguy. III. Pontifícia Universidade Católica do Rio de Janeiro. Departamento de Engenharia Mecânica. IV. Título.

CDD: 621

Acknowledgments

I would like to thank my advisors, Professor Angela Ourivio Nieckele and Dr. João Neuenschwander Escoteguy Carneiro, for their support and friendship over the course of the years; for the great opportunity of working with them, knowledge, and countless revisions of the manuscript.

To the friends I've made in undergrad and graduate school of Mechanical Engineering at PUC-Rio, Vitor Heitor, Murilo Oliveira, Mateus Aguiar, and Rafael Rosa, for the companionship and our inspiring conversations over the years. Also, to my great friends from CIEI, some of whom I've known for most of my life!

To my family, for all their love, support, and care. To my parents and my sister for being there for me every day of my life, and especially during these difficult times.

Lastly, I'd like to thank the Brazilian Research Council (CNPq) and PUC-Rio, for their support, which has been paramount for the completion of this work. This study was financed in part by the Coordenação de Aperfeiçoamento de Pessoal de Nível Superior - Brasil (CAPES) – Finance Code 001.

Abstract

Castello Branco, Rodrigo Luís Formosinho; Nieckele, Angela O. (advisor), Carneiro, João, N.E. (co-advisor). **Development of Momentum Flux Parameters and Stability Analysis of a 1D Two-Fluid Model for Vertical Annular Flows.** Rio de Janeiro, 2022. 151p. Master dissertation – Department of Mechanical Engineering, Pontifical Catholic University of Rio de Janeiro.

The 1D Two-Fluid model has been widely used in industrial simulations to predict two-phase flows in pipelines. Recent advances of the *Regime Capturing* methodology allow for the detection of flow pattern transitions from the onset and development of interfacial instabilities. However, due to the averaging processes required to reduce the dimensionality of the problem, the loss of information renders the model ill-posed, i.e., short wavelengths disturbances are amplified at an unbounded rate and unphysical solutions are obtained. Closure relations play a key role in this problem, since they are required to close the 1D system. Further, the reintroduction of the missing physics may stabilize the flow and render the model well-posed. The present work proposes a model for the liquid momentum flux parameter based on the liquid film velocity profile that is dependent on the local flow quantities. Linear Stability Theory (LST) can be used to assess the influence of closure parameters in the growth of disturbances and to evaluate the hyperbolicity of the model. A viscous approach of the differential Kelvin-Helmholtz and a discrete von Neumann stability analyses are performed to evaluate commonly employed closure models and the proposed formulations for the liquid momentum flux parameter. Numerical simulations are performed, and numerical dispersion relations are extracted from the results to verify the predictions against LST data. A rigorous numerical evaluation of the novel momentum flux parameter models against a large experimental database taken from the literature is carried out. Results show that the proposed models outperform the standard constant C_L values for both pressure drop and liquid film thickness. The models also showed better overall consistency throughout the extensive experimental database.

Keywords

1D Two-Fluid Model, Vertical Annular Flows, Momentum Flux Parameters, Stability Analysis, Assessment of closure models

Resumo

Castello Branco, Rodrigo Luís Formosinho; Nieckele, Angela O. (orientador), Carneiro, João, N.E. (co-orientador). **Desenvolvimento de Parâmetros de Fluxo de Quantidade de Movimento e Análise de Estabilidade do Modelo de Dois-Fluidos 1D para escoamento Anular Vertical**. Rio de Janeiro, 2022. 151p. Dissertação de Mestrado – Departamento de Engenharia Mecânica, Pontifícia Universidade Católica do Rio de Janeiro.

O modelo de Dois-Fluidos 1D vem sendo usado de forma abrangente em simulações industriais para prever escoamentos bifásicos em dutos. Avanços recentes na metodologia de *Regime Capturing* permitem a detecção das transições entre padrões de escoamento através do crescimento de instabilidades interfaciais. Contudo, devido aos procedimentos de média necessários para a redução da dimensionalidade do problema, perdas de informação tornam o modelo mal posto, i.e., perturbações de comprimentos de onda curtos são amplificadas a taxas ilimitadas e soluções não físicas são obtidas. Relações de fechamento possuem um papel chave nesse problema, uma vez que estas são necessárias para fechar o sistema 1D e reintroduzem os mecanismos físicos perdidos que podem estabilizar o escoamento e tornar o modelo bem-posto. O presente trabalho propõe um modelo para o parâmetro de fluxo de quantidade de movimento da fase líquida (ou fator de forma), baseado na distribuição da velocidade do filme, que depende das grandezas locais do escoamento. A Teoria de Estabilidade Linear (LST) pode ser usada para avaliar a influência dos parâmetros de fechamento no crescimento de perturbações e na hiperbolicidade do modelo. A abordagem viscosa da análise de estabilidade diferencial de Kelvin-Helmholtz e a análise discreta de von Neumann são realizadas para avaliar relações de fechamento comumente utilizadas na literatura, bem como as formulações propostas para o parâmetro de fluxo. Simulações numéricas são realizadas, e relações de dispersão numéricas são extraídas dos resultados para verificar as previsões com os dados da LST. Uma avaliação numérica rigorosa dos novos modelos do parâmetro de fluxo com um grande banco de dados experimental é realizada. Os resultados mostraram que as correlações propostas superam os valores padrão constantes de fator de forma para avaliações de gradiente de pressão e espessura do filme de líquido. Os modelos também mostraram melhor consistência ao longo do extenso banco de dados.

Palavras-chave

Modelo de Dois-Fluidos 1D, Escoamento Anular Vertical, Parâmetro de fluxo de *momentum*, Análise de estabilidade, Avaliação de relações de fechamento.

List of Tables

Table 7.1: Experimental configurations and physical properties of the fluids.	91
Table 7.2: Experimental database.	93
Table 7.3: Percentage of cases within the 10% error margin for pressure gradient.....	113
Table 7.4: Percentage of cases within the 10% error margin for film thickness.	116
Table 7.5: Percentage of cases within the 30% error margin for group velocity.	126
Table 7.6: Average error for all quantities.	127
Table 7.7: Combined error.	128
Table 7.8: Simulation time test.	128

List of Figures

Figure 1.1 - Flow configurations for vertical and horizontal pipes (Brennen, 2005).....	19
Figure 3.1 – Geometric Parameters.	37
Figure 3.2 – Flow pattern stability map with varying CL and CG values (Montini, 2011).	45
Figure 4.1 – Coordinate system for the liquid film MFP integration.....	48
Figure 4.2 –Experimental data of velocity profiles compared against the standard UVP (Vassalo, 1999).	49
Figure 4.3 –Comparison of the standard UVP and a modified UVP against the experimental data of Ashwood et al. (2015).	50
Figure 4.4 - CL maps for Model I (left) and Model II (right).	57
Figure 4.5 –CL variation with the liquid Reynolds number for both models.	57
Figure 4.6 Comparison between the experimental CL estimate and the developed models.....	57
Figure 5.1 - Mesh layout (Scalar and vector control volumes).....	59
Figure 6.1- Propagation of a disturbance in horizontal flow (Montini, 2011).	72
Figure 6.2 - Dispersion relation for different stability conditions.	78
Figure 6.3 - Dispersion relation of the discrete stability analysis.	84
Figure 6.4 – Spatiotemporal wave evolution data, where dashed lines represent the linear growth region.	89
Figure 6.5 – Extraction of spatial growth rates from wave amplitude data.	89
Figure 7.1 – Flow pattern maps of the investigated databases. Selected cases are highlighted in red.	92
Figure 7.2 – Influence of surface tension in the amplification rates of all configurations. $\Delta P_{dynl} = 0$; $Cl = 1$, $l = G, L$; $Ulf = UL$	95

Figure 7.3 – Influence of interfacial friction factors f_i in the amplification rates of all configurations. $PiG \neq PiL$; $\Delta P_{dynl} = 0$; $Cl = 1$, $l = G, L$; $Ulf = UL$	97
Figure 7.4 - Influence of the liquid film velocity model Ulf in the maximum amplification rates and dominant frequencies of all configurations. ...	98
Figure 7.5 – Influence of the dynamic pressure model. Case II-Zhao-2. $fiII$; $Ulf = UL$; $PiG = PiL$; $Cl = 1$, $l = G, L$	99
Figure 7.6 - Influence of the WfL constant in the growth rates. Case II-Zhao-2. $fiII$; $Ulf = UL$; $PiG \neq PiL$; $Cl = 1$, $l = G, L$	100
Figure 7.7 – Stability maps showing the IKH limit of well/ill-posed for all configurations. $fiII$; $Ulf = UL$; $PiG = PiL$; $\Delta P_{dynl} = 0$, $l = G, L$	101
Figure 7.8- Influence of the momentum flux parameter in the growth rates. Case I-Kaji-1. $fiII$; $Ulf = UL$; $PiG = PiL$; $\Delta P_{dynl} = 0$, $l = G, L$	102
Figure 7.9 - Influence of the momentum flux parameter in stability properties. All cases. $fiII$; $Ulf = UL$; $PiG \neq PiL$; $\Delta P_{dynl} = 0$, $l = G, L$	103
Figure 7.10- Comparison between linear stability analysis and numerical stability properties obtained from simulations. Case II-Zhao-2. $fiII$; $Ulf = UL$; $PiG \neq PiL$; $\Delta P_{dynl} = 0$, $l = G, L$	104
Figure 7.11- Timestep convergence test for pressure gradient and mean liquid film thickness. Case III-ForeDukler-3.....	106
Figure 7.12- Spatial variation of the instantaneous liquid film thickness and the correspondent CL values calculated by (a) Model I and (b) Model II. Case II-Zhao-2.	107
Figure 7.13- Spatiotemporal variation of the instantaneous liquid film thickness for a constant $CL = 1.05$ and the proposed models. Case II-Zhao-2.	108
Figure 7.14- Temporal data of the pressure field and mean pressure. Case II-Zhao-2.....	110
Figure 7.15- Grid resolution tests for pressure gradient, normalized by the experimental value. Dashed lines indicate 20% error margins.	110
Figure 7.16- Experimental versus Numerical comparisons for pressure gradient. All cases.	111

Figure 7.17- Grid resolution tests for mean film thickness normalized by the experimental value. Dashed lines indicate 20% error margins.	114
Figure 7.18- Experimental versus Numerical comparisons for mean film thickness.	115
Figure 7.19- Experimental versus Numerical comparisons of databases III and VI for mean film thickness - CL 1.05, 1.10, Model I and Model II.	117
Figure 7.20- Temporal liquid film thickness data at $x = 0.62\text{m}$. II-Zhao-2 case.....	119
Figure 7.21- Temporal liquid film thickness data at $x = 2.00\text{ m}$. II-Zhao-2 case.....	120
Figure 7.22- Temporal liquid film thickness data at $x = 7.5\text{m}$. IV-Fershtman-1 case.	121
Figure 7.23- Power Spectral Density (PSD) function of the liquid film height timeseries. II-Zhao-2 case.....	123
Figure 7.24- Development of the Power Spectral Density (PSD) dominant frequency along the domain. II-Zhao-2 case.....	124
Figure 7.25- Grid resolution tests for group velocity, normalized by the experimental value. Dashed lines indicate 20% error margins.	125
Figure 7.26- Experimental versus numerical graph for Group velocity	126
Figure B.1- Time signal delay from two probe positions. Fontalvo (2016).	146
Figure B.2- Cross-correlation signal. Fontalvo (2016).....	147
Figure B.3- PSD spectrum and dominant frequency. Fontalvo (2016)....	147
Figure C.1- Stability Analysis: Dynamic Pressure model test.	148
Figure C.2- Stability Analysis: Momentum flux parameter test. II-Zhao-2	149
Figure C.3- Stability Analysis: Momentum flux parameter test. III-ForeDukler-3.....	149
Figure C.4- Stability Analysis: Momentum flux parameter test. IV-Fershtman-1	150
Figure C.5- Numerical Analysis: Experimental vs Numerical plot for instantaneous liquid film thickness at the probe location closest to the exit.....	151

List of Symbols

A	Cross section area
a	Numerical discretization coefficients
\mathcal{A}	Integral term of the MFP models
\mathfrak{A}	Auxiliary constant for the liquid film velocity
B	Integral term of the MFP models
\mathfrak{B}	Auxiliary constant for the liquid film velocity
b	Source coefficient for discretized equations
b_1	Determinant of solution matrix coefficient
b_2	Determinant of solution matrix coefficient
b_{TVD}	Source coefficient for the TVD discretization
b_{jump}	Source coefficient for pressure jump
b_i	Source coefficient for the interfacial shear
b_{wL}	Source coefficient for the wall shear
b_{dyn}	Source coefficient for the dynamic pressure
b_g	Source coefficient for the gravitational term
C	Integral term of the MFP models
c_1	Determinant of solution matrix coefficient
c_2	Determinant of solution matrix coefficient
C_ℓ	Momentum flux parameter
Co	Courant number
C_w	Group velocity
D	Pipe internal diameter
D_ℓ	Diameter of phase ℓ
$D_{h\ell}$	hydraulic diameter for phase ℓ
E	Amplitude factor
F	Mass flux
\tilde{F}	Pseudo mass flux

\mathcal{F}	Force term
f	Friction factor
G	Amplification factor
g	Gravitational constant
h_L	Liquid film thickness
$h_{L,i}$	Instantaneous Liquid film thickness
h_L^+	Liquid film thickness in dimensionless wall units
i	Imaginary number
K	von-Kármán constant
k_r	Wavenumber
k_i	Spatial growth rate
L	Pipe length
ℓ	Mixing length
M	Solution matrix
N	Number of control volumes
N_μ	Viscosity number
P	Average pressure
$P_{i\ell}$	Phase interface average pressure
\mathcal{P}	Combined dynamic pressure term
\mathbb{P}	Auxiliary constant for the liquid film velocity
\mathbb{Q}	Auxiliary constant for the dynamic pressure derivatives
r	TVD gradient parameter
r_c	Radius of curvature
r_{hl}	Distance between the centerline and the liquid film
Re	Reynolds number
Re_c	Critical Reynolds number
Re_{crit}	Critical Reynolds number for the formation of entrainment
res	Residual for the system of equations
S	Perimeter
S_p	Source term dependent on ϕ
S_c	Source term

ST_w	Surface tension factor
t	Time coordinate
T_{ref}	Reference temperature for isothermal flows
tol	Tolerance
u	Velocity
u^+	Dimensionless average velocity
u_τ	Friction velocity
U	Average velocity
U_{lf}	Liquid film velocity
U_{wave}	Wave velocity
W_f	Empirical constant for the dynamic pressure term
x	Axial coordinate
y	Distance from the wall
y^+	Dimensionless wall units
y_{sub}^+	Limit of the viscous sublayer in wall units
y_{up}^+	Limit of the turbulent layer in wall units
\forall	Volume
∂	Partial derivative

Greek Symbols

α	Volume fraction
β	Pipe inclination
γ	Under-relaxation factor
δx	Vector control volume length
Δx	Scalar control volume length
Δt	Timestep
ΔP_{dyn}	Dynamic pressure term
ε	Amplitude of a perturbed quantity
κ	Interface curvature
κ_1	Axial component of the curvature
κ_2	Radial component of the curvature

λ	Eigenvalues of the equation system
μ	Dynamic viscosity
μ_t	Turbulent viscosity
ν	Kinematic viscosity
ρ	Density
σ	Surface tension
τ	Shear stress
τ^+	Non dimensional shear stress
ϕ	Generic flow quantity
φ	Vector of independent variables
ψ	Flux limiter function
Ψ	Flux limiter function of the TVD scheme
ω_R	Angular frequency
ω_i	Temporal growth rates

Subscripts

i	Related to the interface
L	Related to the liquid phase
G	Related to the gas phase
ℓ	Related to phase (G or L)
$s\ell$	Related to a superficial quantity
m	Related to the mixture
n	Related to the neighboring coefficients
E	Related to the east node
W	Related to the west node
e	Related to the east face
w	Related to the west face
P	Related to the principal node
N	Related to the last control volume
ref	Reference quantity
0	Related to an initial condition

U_ℓ Related to the velocity equation of phase ℓ

α_G Related to the volume fraction equation

Superscripts

+ Non dimensional quantities in terms of wall units

o Quantities evaluated in the previous timestep

* Quantities evaluated in the previous iteration

\sim Quantities obtained from a nodal point interpolation

– Mean value of a quantity

\wedge Perturbation of a quantity

U_ℓ Related to the velocity equation of phase ℓ

α_G Related to the volume fraction equation

P Related to the pressure equation

Table of Contents

1	INTRODUCTION	18
1.1	Objectives.....	21
1.2	Structure of the Dissertation.....	22
2	LITERATURE REVIEW	23
2.1	Summary	33
3	MATHEMATICAL MODEL.....	35
3.1	Geometric Parameters	36
3.2	Boundary and initial conditions	38
3.3	Closure Models.....	38
3.3.1	Density.....	39
3.3.2	Wall shear stress	39
3.3.3	Interfacial shear stress	39
3.3.4	Phase and interface pressure difference	41
3.3.5	Interface pressure jump.....	42
3.3.6	Momentum flux parameter	44
4	A MODEL FOR THE MOMENTUM FLUX PARAMETER.....	47
4.1	Velocity profile models for annular flows	48
4.2	MFP pre-integrated models	52
4.3	MFP simplified models.....	58
5	NUMERICAL METHODOLOGY.....	59
5.1	Gas Volume Fraction	60
5.2	Velocities	62
5.3	Pressure.....	65
5.4	Boundary conditions	67
5.5	Mesh and Time step.....	68
5.6	Numerical execution procedure.....	68
6	THE STABILITY-HYPERBOLICITY PROBLEM OF THE 1D TWO-FLUID MODEL	70
6.1	Linear Stability Analysis.....	71
6.2	Differential Stability Analysis	73
6.3	Discrete Stability Analysis.....	78

6.4	Closure Models.....	84
6.4.1	Phase and interface pressure difference	85
6.4.2	Shear Stresses	86
6.4.3	Momentum Flux Parameters	87
6.5	Numerical Stability Analysis	88
7	RESULTS AND DISCUSSION.....	90
7.1	Case Selection	90
7.2	Stability Analysis Results	93
7.2.1	The effect of surface tension.....	94
7.2.2	Interfacial friction factor	96
7.2.3	Dynamic pressure term	98
7.2.4	Momentum flux parameter	101
7.2.5	Comparison with simulations.....	103
7.3	Impact of the Momentum Flux Parameter in Simulation Results.....	105
7.3.1	Numerical parameters	105
7.3.2	The effect of wave development	106
7.3.3	Pressure gradient	109
7.3.4	Film thickness	113
7.3.5	Frequency.....	122
7.3.6	Group velocity	124
7.3.7	Global evaluation of numerical predictions	127
8	CONCLUSION.....	129
	References.....	132
	Appendix A	145
	Appendix B	146
	Appendix C	148

1 INTRODUCTION

Multiphase flows are of great importance in various areas of the industry and consist of the flow of two or more fluids or phases, separated by interfaces. They are found in several industrial processes such as refrigeration, pipeline transport of oil & gas, boiling water nuclear reactors, etc. A very common scenario of multiphase flow is a two-phase gas-liquid flow in pipelines.

Understanding the dynamics of two-phase flows in pipelines is an ever-present challenge in offshore natural gas production systems, considering the increasing lengths of the pipeline systems as the exploration of oil and gas fields achieve greater depths and the uneven terrain upon where these structures are built. These conditions impose a significant need for detailed mathematical and numerical studies in order to accurately model and maintain the necessary equipment.

The complexity of the physical phenomena and the variety of length scales involved require a compromise between accuracy and computing effort, when developing predictive models. A prominent challenge in predicting two-phase flows in pipes is the tracking of the phases in the domain, which can be distributed in different patterns depending on the operating conditions of the flow (temperature, pressure, and flowrate), fluid properties (density, viscosity, and surface tension) and the pipeline geometry.

Some of the most common flow configurations for vertical geometries include annular, slug, churn, bubbly and dispersed, as shown in Figure 1.1, and for horizontal geometries there are stratified, stratified wavy, bubble, slug, plug, annular and dispersed flow. The behavior of flow patterns is heavily reliant on the liquid and gas superficial velocities, which in turn affects the dynamics of the interface, and interfacial instability is a key mechanism through which the transition between flow configurations occurs. In stratified flow, for instance, an increase in the gas superficial velocity leads to a transition to stratified wavy flow, whereas an increase in the liquid superficial velocity induces the formation of slug flow.

In gas production wells and transport pipelines, it is common for the gas current to be accompanied by a liquid mixture of gas condensate, oil and water. In situations where the gas flowrates are elevated (e.g., in new wells) a prominent

flow regime in vertical pipes is annular flow. It consists of an inner gas core flowing circumscribed by a thin liquid film in contact with the pipe walls, as the gas drags the liquid mixture and both phases flow concurrently.

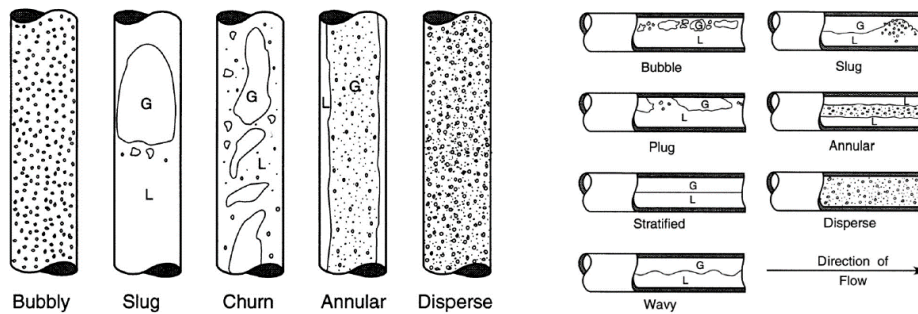


Figure 1.1 - Flow configurations for vertical and horizontal pipes (Brennen, 2005).

The dynamics of the liquid film are important to accurately predict the behavior of annular flows. Due to the gas-liquid relative velocity, a common phenomenon is the appearance of interfacial waves in the liquid film, and these waves can be sub-categorized into ripples – small amplitude and high frequency – and disturbance waves – large amplitude and low frequency. They act as a source of surface roughness to the gas flow and therefore play a role in the interfacial drag and pressure drop. A major problem in gas exploration is the gradual decrease in operating pressure, which results in lower gas flowrates and reduces its ability to drag the liquid film upwards against gravitational forces. The resulting accumulation of liquid at the entrance of the well and impairment of further production is a known phenomenon called liquid loading (Belt, 2007; Alves, 2014).

Moreover, the interaction of disturbance waves with the gas current is known to cause the entrainment of droplets in the gas core (Hall-Taylor *et al.* 2014), which is a relevant mechanism affecting the liquid distribution and also has implications for heat transfer applications, as steam-vapor droplet annular flow is characterized by high convective heat transfer. The dynamics of the liquid film is an important and largely investigated element of rod bundle coolant subchannels in boiling water reactors (BWR). Part of this effort revolves around a phenomenon called dry-out (Kumar *et al.*, 2016). If the flow achieves a critical heat flux, the excessive heating can evaporate the liquid film, and the reduced heat transfer coefficient of the resulting misty gas flow can substantially increase the temperature of the fuel rods (Saxena & Prasser, 2020).

To accurately predict multiphase flows in pipes, a sophisticated numerical methodology is required. There is a wide variety of mathematical models available in the literature that are divided into two categories: time and phase average-based

method, and direct interface tracking methods. In the interface tracking category, also referred to as the one-fluid model, one set of conservation equations are solved for the entire domain, with an additional treatment being performed to track the fluid interface. In the VOF (Hirt & Nichols, 1981) and Level-Set (Osher & Sethian, 1988) methods for example, this is achieved by solving an additional transport equation for a marker function.

In the time and phase average category, a set of averaged conservation equations are solved to obtain an accurate solution of the macroscopic behavior of the flow. This is a reasonable approximation as the microscopic dynamics of flows are usually irrelevant for most engineering problems. Statistical properties are employed to model those complex microscopic phenomena. For example, in disperse phase flows, it is necessary to determine the average particle size, collective drag law for multiparticle systems, rates of nucleation, evaporation or condensation (Ishii & Mishima, 1984). Within this class, three main models stand out: the homogeneous, the drift-flux, and the two-fluid model. In particular, the two-fluid model solves one set of conservation equations for each of the phases, and their interaction is modeled through the interfacial terms. For pipe flows, a common approximation is to consider the relevant characteristics of the flow to vary mainly in the axial direction, which allows for an area averaging process in the cross-section of the pipe, rendering the model one-dimensional.

The one-dimensional two-fluid model is widely used in the literature to tackle two-phase flow problems in industrial applications, it is both a robust and time efficient tool to employ in pipeline flows that extend several kilometers. Additionally, the use of the 1D two-fluid model with sufficiently fine meshes allows for the capture of interfacial wave evolution in the domain, opening the possibility to simulate various flow regimes using a single numerical framework (Nieckele & Carneiro, 2017). This approach was originally employed to detect the onset of slug-flows from a stratified configuration and is thus referred to as Slug Capturing (Issa & Kempf, 2003). Later on, this methodology has been extended to what is referred to as *Regime Capturing*, which allows detection of several other flow patterns in horizontal and vertical geometries (Bonnizi *et al.*, 2009) (Nieckele & Carneiro, 2017).

A common issue with the one-dimensional approach is that the averaging processes remove information about the flow field and momentum transfer from the system of equations, rendering it ill-posed for certain configurations, e.g., when the relative velocity between the gas and liquid phase exceeds a certain value in horizontal flow (Liao *et al.*, 2008); for vertical geometries, the 1D two fluid model is

known to be unconditionally ill-posed (Banerjee & Chan, 1980). Ill-posedness is characterized by the unbounded growth of high frequency perturbations, which in turn contaminates the physical instabilities rendering the solution meaningless, and it manifests as the inability to obtain a mesh convergent solution.

One may argue that for practical mesh sizes, the numerical discretization scheme may be enough to dampen the disturbances, rendering the model numerically well-posed. However, methodologies within the *Regime Capturing* approach rely on their ability to detect the naturally occurring growth of interfacial instabilities into waves, which may require very fine spatial and temporal discretization. There is considerable effort in the literature to develop modifications to the standard model to ensure its hyperbolicity by reinjecting information that was lost in the averaging process through closure models, which may aid the damping of short wavelength perturbations. The development of accurate closure relations is an active challenge in one-dimensional modeling. Several formulations have been presented over the years with varying rates of success. A promising closure model that has gained attention in recent works is the momentum flux parameter, or shape factor, that introduces the effect of a nonuniform velocity profile into the governing equations.

Linear stability theory is often employed to assess the dynamics of instabilities by analyzing the characteristics of the system of equations. To obtain a comprehensive understanding of the effects of closure relations in the model, an assessment through the optics of a stability analysis is positive and it can be performed in addition to numerical grid convergence tests and comparisons with experimental data.

1.1 Objectives

The objectives of this work are to improve the regime capturing methodology within the two-fluid model by evaluating different closure models through the optics of linear stability theory on their ability to stabilize the flow. Additionally, it is noted that a promising challenge in closure modelling is the reintroduction of information regarding the velocity distribution in the pipeline cross-section through the momentum flux parameter. The present work expands on this area of research by developing momentum flux parameter models for the liquid phase in vertical annular flows. The novel formulations are evaluated in their ability to ensure well-posedness to the system through a linear stability analysis, and in their contribution to the physical accuracy of the model through simulation tests against an extensive

experimental database.

1.2 Structure of the Dissertation

A literature review of the main experimental and numerical advancements in two-phase annular flows is carried out in Chapter 2. Chapter 3 outlines the mathematical model for the 1D Two-Fluid Model, boundary conditions for the physical phenomenon and closure relations.

In Chapter 4, a closure relation that aims to model the liquid film velocity distribution in the cross-section of the pipe is devised. Chapter 5 describes the methodology for the numerical simulations of two-phase flows with the 1D Two-Fluid Model. Chapter 6 presents the mathematical and discrete formulations of the Linear Stability Analysis performed in this work. Chapter 7 shows the main results of the present work, i.e., the stability analyses and discussions of the impact of closure models from a hydrodynamic stability standpoint. Further, the numerical results are discussed, which constitute of a rigorous grid sensitivity test and comparisons against an extensive experimental database. Lastly, the conclusion and suggestions for future works are carried out in Chapter 8.

2 LITERATURE REVIEW

Upward vertical annular flow has gained a lot of attention in the literature due to its complex nature and has been the object of a large stream of experimental studies. It consists of a turbulent gas flow in the core region of the pipe, circumscribed by a thin liquid film flowing in the pipe wall. For higher superficial velocities, the gas shear induces the appearance of wavy structures in the gas/liquid interface. Hall-Taylor *et al.* (1963) performed one of the earliest experimental works that examined the conditions by which interfacial waves occur through measurements of wave velocity, separation, and frequency. Wolf *et al.* (2001) have shown that interfacial waves tend to form close to the inlet, where the liquid phase is introduced. After a transitional region of approximately 10 diameters from the liquid injection point, the waves become circumferentially coherent (Zhao *et al.* 2013). This transitional period allows for the growth of those interfacial structures into what are known as disturbance or roll waves.

Disturbance waves are large amplitude and low frequency waves, which travel with a higher velocity than the overall liquid film (Alekseenko *et al.*, 2013; Hall-Taylor *et al.*, 2014) and tend to appear when a critical gas flow rate is achieved. The height of these waves is known to be about as three/four times that of the liquid film (Hewitt & Nicholls, 1969). Photographic studies have shown that those heights undergo large variations (Hewitt *et al.*, 1990; Badie *et al.*, 2001), rendering the behavior of roll waves three dimensional in nature. They also move with an approximately constant wave velocity (Azzopardi, 1997). Several researchers have performed studies on roll waves over the years (Hall Taylor *et al.*, 1963; Chu & Dukler, 1974; Azzopardi, 1986).

Interfacial waves are known to have a profound effect on interfacial shear stress, thereby increasing the pressure drop in the flow (Wang *et al.*, 2004). Early works such as Wrobel & McManus (1961) have shown that the accurate understanding of wave structure and behavior leads to more accurate interfacial shear modeling.

Furthermore, a secondary irregular wavy structure known as ripples are present in the wavy annular film. They are characterized by low amplitudes, high frequencies, and travel more slowly in a three-dimensional manner over the film

(Schubring & Shedd 2008). Ripples are said to always be generated in the wake of disturbance waves and are absorbed by subsequent disturbance wave structures (Alekseenko *et al.*, 2009). Additionally, the onset of entrainment and deposition is largely known to be caused by the detachment of droplets from the crests of disturbance waves (Azzopardi, 1997). This is caused by the complex interaction between the gas core flow, ripples, and disturbance waves (Woodmansee & Hanratty, 1969; Alekseenko *et al.*, 2013). Recent works employing non-intrusive measurement techniques have been able to obtain three-dimensional interfacial wave data. Fershtman *et al.* (2020) performed a three-dimensional reconstruction of the interface, allowing for the identification of three types of wave formations, namely ripples, disturbance waves, and rogue waves. They describe rogue waves as infrequent solitary disturbance waves flowing in a ripple dominated interface.

The wave dynamics also affect the liquid film and gas core velocity profiles. Several authors have investigated the velocity profile shapes in vertical annular flow. Gill *et al.* (1964) have carried out measurements of the gas velocity distribution for air-water flow, where a clear parabolic shape is observed. The influence of the gas and liquid flow rate were also investigated and showed that an increase in the gas flowrate raises the magnitude of the profile, while preserving the shape, and an increase in liquid flowrate alters the parabolic shape. Azzopardi & Teixeira (1994) performed velocity profile measurements for both single phase air flow and two-phase air-water flow. Reasonable agreement was obtained with the 1/7 power-law profile.

Vassalo (1997) obtained the liquid velocity distribution on several configurations and compared results to the *universal velocity profile* (UVP), obtaining reasonable agreement. Ashwood *et al.* (2015) measured the liquid velocity profile shape on a square cross-section configuration, where results did not agree well to the UVP. They propose a novel velocity profile correlation that adjusts to their experimental data. Cioncolini *et al.* (2015) evaluated the results presented in Ashwood *et al.* and proposed new bounds for the viscous sublayer, buffer and turbulent layers based on the data.

There are several parameters that can be used to characterize interfacial waves in annular flow, such as structural quantities, e.g., wave height, base height, spacing; and dynamic features such as wave and film velocity, entrainment and deposition rates, frequency (Wang *et al.*, 2004). Those parameters change continuously along the flow development. Thus, to obtain accurate theoretical models for the physics of annular flow systems, detailed axial measurements of

the local flow features of the liquid film are paramount.

Fore & Dukler (1995) investigated the entrainment and deposition of droplets in the liquid film to determine the physical mechanism of momentum transfer from the process of droplet deposition.

Wolf *et al.* (2001) performed air-water annular flow experiments on a 31.8 mm internal diameter configuration. They have observed that the complex changes in the film begin to occur within a range of 50D, and entrainment begin to develop between 100-300D.

Hazuku *et al.* (2008) have performed an extensive experimental study of the liquid film behavior, providing a large dataset of statistical quantities such as maximum, average, and sublayer film thickness, wave frequency, interfacial shear stress, etc.

Belt *et al.* (2010) performed an experimental study of vertical annular flow in a 0.05m diameter test section. Statistical data for several characteristics of disturbance waves, such as height, length, velocity, frequency is obtained. They observe that disturbance waves are located randomly in space, within a Gamma distribution. They speculate that this behavior indicates that the distribution of disturbance waves in space is a result of several processes of coalescence between pre-existing waves.

Zhao *et al.* (2013) have performed experiments for air-water annular flow in a short 2m test section to investigate the three-dimensional behavior of the interfacial structures. They evaluate the spectral content of the interface and the shifts in dominant frequencies with axial development.

Wang *et al.* (2021) investigated the wave characteristics in high liquid flow rate upward annular flow. Liquid superficial velocities range from 0.02 m/s to 2 m/s. They perform a comprehensive review of existing models for predicting statistical data in wispy annular flow.

The advancement of high computational power hardware in recent years has allowed for the development of highly detailed three-dimensional numerical studies of multiphase flows in pipelines. This approach may tackle some of the limitations of instantaneous measurements in experimental studies, such as the availability of data on only slices of the domain.

Although 2D approaches have been applied for modeling annular flow in earlier stages (Han & Gabriel, 2007), the three-dimensional nature of physical phenomena such as droplet entrainment and turbulence has led to the adoption of a 3D computational fluid dynamics (CFD) approach. For these types of simulations, authors would typically use a VOF or Level-Set approach. Rodriguez (2009)

performed an axisymmetric, periodic direct numerical simulation (DNS) of annular flow in a short domain using the Level-Set method. Liné *et al.* (2013) performed fully three-dimensional simulations of the development of horizontal slug flow from an initially stratified configuration with the Level-Set method. The goal of these works was to extract the three-dimensional fields to assess and aid in the improvement of simplified models for 1D simulations. Kumar *et al.*, (2016) performed 3D laminar vertical annular flow simulations with VOF to capture the physical mechanisms of droplet entrainment from the interfacial waves. A flow pattern map containing information regarding the physical mechanisms responsible for transition from annular to droplet annular flow is devised. Fan *et al.* (2019) employed the VOF method with the Reynolds Averaged Navier Stokes (RANS) turbulence modeling to predict the wave dynamics of downward annular flow, comparing their results to the work of Alekseenko *et al.* (2015). Fan *et al.* (2020) performed an experimental and 3D CFD study of downward annular flow with a novel turbulence damping model for RANS. They evaluated the predicted wave structures against the measured data and found good qualitative agreement. Rocha (2020) performed 3D simulations of slug flow in horizontal pipes with the VOF method and obtained several correlations for closure models for 1D methodologies from the three-dimensional data. Saxena & Prasser (2020) employed the VOF method with both Large Eddy Simulation (LES) and unsteady-RANS turbulence models to simulate annular flow in a double sub-channel geometry of a fuel rod bundle in BWRs. They found that the time averaged liquid film thickness data with the LES model best agreed with experimental data.

For large scale industrial simulations, however, the feasibility of three-dimensional approaches breaks down as the computational power required for such tasks becomes unattainable. Additionally, for most engineering applications, the microscopic details of the flow are irrelevant, and average and statistical quantities of the flow are sufficient to yield accurate predictions. For that purpose, one-dimensional simulations are widely employed. The time and phase average class of numerical methods is very popular for the development of 1D formulations. As previously mentioned, three main models stand out: the homogeneous, the drift-flux, and the two-fluid model.

The homogeneous model solves one set of conservation equations for the mixture, i.e., it considers that both phases act as a single fluid, flowing with the same velocity. Although this method provides simpler and more computationally efficient predictions, it is heavily reliant on empirical correlations. The drift-flux approach models the relative motion between the phases by introducing

constitutive relations corrected by empirical correlations. In this model, good agreement can be obtained when there is strong coupling between the phases. In separated flow such as stratified or annular, the drift-flux model offers inaccurate predictions.

Lastly, the two-fluid model solves one set of mass, momentum, and energy equations for each of the phases present. The coupling between the phases is modeled through the interfacial transfer terms. This constitutes a more accurate and sophisticated description of the flow, as it models the velocity fields separately. The standard two-fluid model was first introduced in the work of Ishii (1975) for applications in the nuclear industry, having since then been adopted by numerical codes in the oil & gas industry to solve pipeline flows. Prominent multiphase commercial codes that employ this method include CATHARE (Micaelli, 1987), OLGA (Bendiksen *et al.*, 1991), LedaFlow (Danielson *et al.*, 2005) and ALFAsim (Pasqualetto *et al.*, 2019).

Continuous effort has been made to accurately predict the slug flow regime in pipelines, which led to several approaches within the two-fluid framework. *Unit-Cell* (Dukler & Hubbard, 1975) and *Slug-Tracking* (Nydal, 2012) approaches have been developed to work-around the small length and time scales of slug flows, avoiding the resolution required to capture small scale phenomena. They rely on empirical closure relations, which limits the generality of the models (Nieckele & Carneiro, 2017). For example, the *Unit-Cell* methodology requires flow pattern criteria to decide whether slug flow is locally present in the pipe and constitutive relations to determine the average characteristics of the slugs and bubbles. In *Slug-Tracking*, the criteria for slug generation are imposed by a predetermined model, e.g., based on a flow pattern map. Slugs are tracked using a Lagrangian reference frame, and the information is injected into the mass and momentum flux calculations at the position of the bubbles' nose and tail (Bendiksen, 1984). The *Slug-Capturing* methodology (Issa & Kempf, 2003), however, captures the slug formation automatically from the natural growth of hydrodynamic instabilities into waves on stratified flows. Therefore, the model does not require empirical correlations, as the formation and propagation of slugs are predicted, not imposed (Nieckele & Carneiro 2017). This methodology has been expanded to more complex applications such as slug flow with droplet entrainment and deposition modeling (Bonnizi, 2003; Siqueira, 2019) and three phase flow (Bonnizi & Issa, 2003; Moraes *et al.*, 2020).

In recent years, there has been significant advancement in generalizing this methodology to other flow pattern transitions, such as the transition to slug,

annular, bubbly flows in horizontal pipes (Bonnizi *et al.*, 2009). Emamzadeh & Issa (2013) investigated the transition from stratified to annular flow in horizontal pipes. Nieckele *et al.* (2013) employed this methodology to explore the initiation and development of slug flow and provided detailed predictions of statistical parameters of slugs in horizontal pipes. Han & Guo (2015) explored the onset of hydrodynamic and terrain-induced slugs in a pipeline-riser system. Fontalvo *et al.* (2016) used the *Regime Capturing* technique to predict the interfacial wave behavior of vertical annular flows and validated their models against the experimental data due to Zhao *et al.* (2013). Pasqualetto *et al.* (2017) performed numerical studies of stratified flows with high viscosity oils, capturing the transition to stratified wavy. They have tested existing interfacial shear stress correlations against experimental data. Nieckele & Carneiro (2017) expanded the methodology with predictions of horizontal stratified and slug flow as well as vertical annular and slug flows. They tested numerical spatial and temporal discretization schemes and coined the term *Regime Capturing* to characterize this new methodology. Good agreement was found against the reference data. Ferrari *et al.* (2017) proposed a five equation 1D two-fluid model for *Slug Capturing*. The fifth equation performs the advection of the gas volume fraction. They successfully validate the methodology against slug formation and propagation tests in horizontal geometries. Leporini *et al.* (2021) expanded on the work of Ferrari *et al.*, evaluating the novel method with pure vertical hydrodynamic slug flow cases. Good agreement was obtained against experimental data, particularly for slug mean frequency and mean velocity.

The use of very small grid cells in *Regime Capturing* methods is in itself a starting point on a discussion of stability and ill-posedness of the 1D two-fluid model. As mentioned, the averaging processes remove information from the system of equations and renders the model ill-posed for certain configurations. In practical terms, ill-posedness manifests as an inability to obtain a mesh convergent solution.

In fact, the standard 1D two-fluid model is known to be unconditionally ill-posed for vertical geometries, and care must be taken when using high resolution meshes to capture regime transitions. A common strategy as a workaround is to limit temporal and spatial refinement, which is especially desirable for long pipeline simulations where computational power is demanding. In these cases, the numerical schemes provide a stabilizing effect that renders the model numerically well posed. In *Regime Capturing* methodologies, however, this pragmatic solution is limited to configurations where the flow transition does not depend on the growth

of instabilities. For example, Issa & Galleni (2015) found that for vertical slug flows, even in an ill-posed system, a mesh independent solution can be attained for a range of practical mesh sizes, $\Delta x/D \leq 0.1$.

Therefore, a study on the hyperbolicity of the differential formulation of the two-fluid model is paramount to understand and solve the underlying problems that lead to ill-posedness. The theoretical background on the stability-hyperbolicity of the 1D Two-Fluid model will be explored in more detail in further chapters. In short, the characteristics are the roots of a linear representation of the system of partial differential equations (PDEs). They dictate the rate with which information propagates in space and time and are key to the determination of a system's hyperbolicity: if the characteristics are real, the system is hyperbolic/well-posed; if one of them is complex, the system is elliptic/ill-posed (Prosperetti & Tryggvason, 2007).

There are different ways to test the hyperbolicity of a model. A basic test is the analysis of characteristics, where a linearized system is obtained, and the characteristic roots are extracted. This approach has been used by Issa & Kempf (2003) and Bonnizi (2003) with the basic 1D Two-Fluid Model and it has shown that the problem is conditionally well-posed (real roots) if the hydrostatic pressure profile is imposed. Other works have performed characteristic analyses on the Two-Fluid Model within the Regime Capturing approach (Carneiro, 2006; Fontalvo, 2016; Pasqualetto, 2017).

The mechanism through which ill-posedness manifests is an unbounded growth of small wavelength perturbations in the system, which hinders the physical representation of the problem. Linear Stability Theory (LST) deals with the emergence of these small-scale disturbances in an otherwise undisturbed flow. The well-known Method of Small Disturbances introduces infinitesimal perturbations into stable flow fields and quantifies the growth or decay of these perturbations under a system of mathematical or discrete equations. The result is a dispersion relation that correlates the growth rates with a frequency or wavelength spectrum. In ill-posed systems, the growth rate will increase radically for critical frequencies/wavelengths. The Inviscid and Viscous Kelvin-Helmholtz analyses are employed to the differential system of equations to evaluate the stability of the mathematical system. The von Neumann analysis, however, is applied to the discrete system, and accounts for the numerical effects of the discretization schemes, e.g., numerical viscosity. Considerable effort has been made to explore the hyperbolicity through a stability lens. Several authors have employed the IKH analyses to analyze the behavior of small imposed sinusoidal

interfacial waves in stratified flows and derive a criterion for the onset of ill-posedness (Milne-Thomson, 1968; Kordyban & Ranov, 1970; Taitel & Dukler, 1976).

Barnea & Taitel (1988) evaluated the stability of co-current and counter-current annular flow and proposed a simple transient formulation that neglects the Kelvin-Helmholtz contribution to instability. Barnea & Taitel (1993) devised inviscid and viscous formulations for the Kelvin-Helmholtz instability applied to stratified flow. They produced a stability map for varying liquid and gas superficial velocities, showing the neutral-stability regions for both formulations, and how they intersect with flow pattern transition, as interpreted in the work of Barnea (1991).

Liao *et al.* (2008) performed a discrete stability analysis on a stratified configuration using the two-fluid model with three spatial discretization schemes, namely the 1st order and 2nd order Upwind, Central Difference and the QUICK scheme. They observe differences in stability from the different Upwind schemes, where the 1st order Upwind excessively damps the solution, and the 2nd order Upwind is inaccurate due to its unstable nature. They assert that the instabilities due to ill-posedness trigger the unbounded growth of round-off errors, effectively rendering the physical solution unusable.

Fullmer *et al.* (2014) performed differential and discrete stability analyses to assess the inclusion of stabilizing parameters such as pressure jump due to surface tension, dynamic pressure, numerical viscosity, etc. under Kelvin-Helmholtz instability conditions. They propose a criterion for assessing the suitability of the numerical scheme for simulations of stratified flows. They assert that artificial viscosity can over-stabilize the system, particularly in coarser meshes, and that a physical dissipation mechanism, i.e., Reynolds stresses, may be a more scientific approach.

Galleni & Issa (2015) present the differential and discrete stability analyses to study the ill-posedness of slug flow in vertical pipes. They state that the discretization of the equations introduces a cut-off limit to the growth of instabilities, which renders the system numerically well posed for practical mesh sizes. For mesh sizes $\Delta x/D \ll 0.1$ the ill-posedness will eventually manifest.

Sanderse *et al.* (2017) performs a stability analysis through an automated von Neumann method that does not require the standard analytical derivations. Additionally, they introduced the so-called Discrete Flow Pattern Map, that determines the degree to which the effective stability regions differ from the differential theoretical regime. They observe that flows within the well-posed unstable region can develop to become ill-posed, which may limit the application

of the *Regime Capturing* techniques.

Kushnir *et al.* (2017) evaluates the introduction of closure relations and their influence on the stability of stratified flows. They argue that the tuning of these parameters may allow the two-fluid model to accurately reproduce the long wave neutral stability curve.

In fact, the effect of closure models on the well-posedness of the system is a very important object of study. Several authors have devised formulations that compensate for some physical parameters that were missing from the standard model. These closure models are, to some degree, specific to a certain flow pattern, or are restricted to a particular range, e.g., Reynolds number. For instance, the interfacial shear stress is a very important closure relation. It is defined in terms of the Fanning friction factor, $\tau_i = 1/2 f_i \rho_G |U_G - U_{lf}|(U_G - U_{lf})$, where f_i is the interfacial friction factor, ρ_G is the gas density, U_G is the gas phase velocity, and U_{lf} is the liquid film interface velocity. The adequate modeling of τ_i is one of the most challenging tasks in the development of the Two-Fluid model (Pasqualetto, 2017), as it characterizes the momentum exchange between the gas core and the liquid film. Thus, it must account for the effect of interfacial waves in the flow, although the underlying physical mechanisms are not yet fully understood. Several authors have devised formulations for the interfacial friction factor f_i for annular flow. Wallis (1969) proposed a widely used correlation, using an analogy of single-phase flow to incorporate turbulence in rough pipes, though its validity is limited to a small range of film thickness values. Whalley & Hewitt (1978) expanded on the work of Wallis and included a term to consider the density ratio in their formulation. Fore *et al.* (2000), also based on the Wallis correlation, included a dependence in the gas Reynolds number. Belt *et al.* (2009), however, argued that a dependence on Reynolds number is unphysical. They also propose a formulation that correlates the sand-grain roughness to the frontal area of the disturbance waves. Aliyu *et al.* (2017) proposed a correlation based on the gas Reynolds and Froude numbers. Ju *et al.* (2019) developed a correlation based on the liquid and gas Weber numbers. They argue that the dependence of existing correlations on film thickness adds additional uncertainty to the model. Ribeiro *et al.* (2021) performed an assessment of existing correlations with high liquid viscosity test cases, comparing results of pressure drop, film thickness and gas void fraction. They conclude that the Belt *et al.* correlation performed best for 100 mPa s viscosity liquids, whereas a correlation proposed by Moeck (1970) obtained more accurate results for the 200 mPa s viscosity case.

There has also been some effort to accurately model the liquid film interfacial velocity. It is common to approximate it as the liquid phase velocity U_L . Fowler & Lisseter (1992) proposed an approximation of $U_{lf} = 2U_L$. Belt *et al.* (2009) correlated the liquid film velocity with the characteristic velocity of disturbance waves, and Berna *et al.* (2014) proposed a novel expression for the wave velocity. Wang *et al.* (2020) argue that existing wave velocity correlations would greatly underpredict the experimental data for wispy annular flow. They then propose a novel correlation based on high liquid film velocity annular flow data.

The difference between the average phase and interfacial pressure $\Delta P_k = (P_k - P_{k_i})$, is modeled in horizontal pipe as a quantity proportional to the hydrostatic pressure variation in the cross-section. For vertical flows, this difference is often modelled as a dynamic pressure. Bestion (1990) proposed a dynamic pressure term proportional to the difference between the gas and liquid volume fraction and velocities for separated flows. Fowler & Lisseter (1992) devised a dynamic pressure model from the Bernoulli equation, as a function of the wave velocity. Fontalvo *et al.* (2020) coupled the wave velocity correlation due to Berna *et al.* with the Fowler & Lisseter dynamic pressure model for vertical annular flow configurations, which yielded very good agreement with experimental data.

We note that the 1D Two-Fluid formulation due to Fowler & Lisseter accounts for the shape of the velocity profile in the liquid film. The standard area averaged model assumes that both liquid and gas velocity profiles are flat. The accounting for the profile shape can be done through the momentum flux parameter, or profile shape factor, C_ℓ (where the subscript ℓ represents either the liquid phase L or the gas phase G) which will be explored in more detail in a later chapter. It is defined as $C_\ell = A \int u_\ell^2 dA / [(\int u_\ell dA)(\int u_\ell dA)]$, where u_ℓ is the phase velocity. Several authors have explored the influence of the momentum flux parameter (Song & Ishii, 2000; Montini, 2011). Song & Ishii (2001a) have shown that the incompressible 1D two-fluid model is stable to the short wavelength perturbations if appropriate shape factors are used. They have devised shape factors for the liquid phase from parabolic velocity profiles for different flow patterns and argue that the parameter holds constant throughout the domain. For annular flow, a value of approximately 1.05 was calculated.

Issa & Montini (2010) analyzed the shape factor for horizontal flows and concluded through a stability analysis that liquid factor, C_L , greater than unity has a positive effect towards the well-posedness of the system, whereas a C_G has an

opposite effect.

Montini (2011) tested a range of momentum flux parameter values for various horizontal flow test cases, and proposed values that would ensure well-posedness from a stability sense for these cases. A C_L of 1.65 was shown to render nearly the entire slug-flow area in a horizontal flow pattern map well-posed. However, care must be taken in ensuring the physical validity of the values chosen. As noted in Montini (2011), the shape factors that maximize well-posedness in a flow pattern map greatly overpredict the physically accurate values obtained from integration of velocity profiles.

Fontalvo *et al.* (2020) evaluated different momentum flux parameter values for annular flow, and concluded that a value close to unity, 1.05, yielded the closest agreement to statistical experimental data. Castello Branco *et al.* (2021) expanded on this work by evaluating closure relation through the lens of LST, aiming to understand their impact on wave formation. Results have shed some light into both linear and nonlinear behaviors of the momentum flux parameter in numerical simulations. Both works suggest that the hypothesis of a constant values defined *a priori* should be assessed further. It is expected that the parameter should depend on the local flow field

Some works have tackled this issue by using pre-integrated models from velocity profiles to generate an instantaneous C_ℓ ($\ell = L, G$) value. Kushnir *et al.* (2017) devised a pre-integrated model based on a parabolic velocity profile to calculate the shape factors for stratified flows. Bonzanini *et al.* (2019) used the pre-integrated model proposed by Biberg (2007) to predict the instantaneous shape factors for stratified and slug flow configurations. Further, we note that the application of variable shape factors in upwards annular flow have not yet been explored in the literature.

2.1 Summary

This literature review chapter explored the main advancements in characterization of vertical annular flows through experimental studies, highlighting works that provide useful statistical quantities and temporal data that can be used to validate numerical methodologies (e.g., Fore & Dukler, 1995; Wolf *et al.*, 2001; Hazuku *et al.* 2008; Belt *et al.*, 2010; Zhao *et al.*, 2013; Wang *et al.*, 2021). Further, recent three-dimensional CFD studies are briefly discussed, where promising works that obtained qualitatively similar results to experimental data are highlighted (e.g., Kumar *et al.*, 2016; Fan *et al.*, 2019; Fan *et al.*, 2020; Saxena & Prasser,

2020).

The well-known one-dimensional approaches employed in industrial applications are discussed, with particular emphasis to the Two-Fluid Model. The *Regime Capturing* Methodology is outlined and an exposition of its capability to accurately predict the transition of flow regimes is given. A stream of works that have successfully employed it in test cases are listed and reviewed (e.g., Issa & Kempf, 2003; Bonnizi, 2003; Bonnizi & Issa, 2003; Nieckele *et al.*, 2013; Han & Guo, 2015; Pasqualetto *et al.*, 2017; Nieckele & Carneiro, 2017; Fontalvo *et al.*, 2020). The stability-hyperbolicity problem of the 1D Two-Fluid Model is also briefly discussed. The use of Linear Stability Theory as a tool to explore the effects of closure relations is also discussed, and promising works in the field are highlighted (Barnea & Taitel, 1993; Liao *et al.*, 2008; Fullmer *et al.*, 2014; Galleni & Issa, 2015; Sanderse *et al.*, 2017).

Finally, a discussion on development of closure relations is performed, and we identify a gap in the literature in the development of instantaneous momentum flux parameter correlations based on pre-integrated models for vertical annular flows.

3 MATHEMATICAL MODEL

The present work focuses on the study of vertical upward annular flow in pipelines. As previously mentioned, oil and gas wells and pipelines – in practical applications – can extend to several kilometers, which allows for the common approximation to consider that most variations of relevant flow quantities occur in the axial direction. This justifies the use of one-dimensional approaches to model flows in pipelines. Moreover, one of the more important phenomena of annular flow, namely the development of large interfacial waves, is known to behave in a circumferentially coherent manner far from the inlet, i.e., the disturbance waves vary mostly axially (Zhao *et al.*, 2013).

The Two-Fluid Model (Ishii, 1975; Ishii & Mishima, 1984) is employed here to solve a two-phase annular flow within the *Regime Capturing* methodology, i.e., the development of the interfacial structures is naturally predicted from the growth of small instabilities of the system of equations. We argue that this methodology is superior to those employed in current commercial codes, such as *Slug Tracking* and *Unit-Cell*, in which, for example, slug frequencies and lengths must be defined *a priori*. The ongoing development of physically based closure models has expanded the use of *Regime Capturing* to more complex configurations, such as vertical annular flows, where the standard model is ill-posed.

The standard three-dimensional model is obtained through phase averages of the Navier-Stokes equations. Volumetric averages are obtained for each phase as in the following equation

$$\langle \phi_\ell \rangle = \frac{\int_{\mathcal{V}_\ell} \phi_\ell d\mathcal{V}}{\int_{\mathcal{V}_\ell} d\mathcal{V}} \quad (3.1)$$

where ϕ is a generic flow quantity, \mathcal{V} is the occupied volume and the subscript ℓ is a reference to the phase ($\ell = G$ or L , i.e., gas or liquid phase). The volume fraction of phase ℓ is defined as

$$\alpha_\ell = \frac{\mathcal{V}_\ell}{\mathcal{V}} \quad (3.2)$$

with the following restriction

$$\alpha_L + \alpha_G = 1 \quad (3.3)$$

The one-dimensional model is obtained by performing an area average in the cross-section of the pipe. The area average is defined as

$$\bar{\phi} = \frac{1}{A} \int_A \phi \, dA \quad (3.4)$$

The brackets and bar are omitted for simplicity in the following equations. The conservation equations for an isothermal flow are defined as in Ishii & Hibiki (2011) for the gas and liquid phases, and the phases are coupled through interfacial transfer terms. The gas and liquid mass conservation equations are

$$\frac{\partial(\alpha_G \rho_G)}{\partial t} + \frac{\partial(\alpha_G \rho_G U_G)}{\partial x} = 0 \quad (3.5)$$

$$\frac{\partial(\alpha_L \rho_L)}{\partial t} + \frac{\partial(\alpha_L \rho_L U_L)}{\partial x} = 0 \quad (3.6)$$

where ρ and U are the density and phase velocity, respectively. t and x are the time and spatial axial coordinates. The linear momentum equations for upward vertical flow are defined as

$$\begin{aligned} \frac{\partial(\alpha_G \rho_G U_G)}{\partial t} + \frac{\partial(C_G \alpha_G \rho_G U_G^2)}{\partial x} = & -\alpha_G \frac{\partial P_{G_i}}{\partial x} \\ & - \frac{\partial \alpha_G (P_G - P_{G_i})}{\partial x} - \alpha_G \rho_G g - \frac{\tau_i S_i}{A} \end{aligned} \quad (3.7)$$

$$\begin{aligned} \frac{\partial(\alpha_L \rho_L U_L)}{\partial t} + \frac{\partial(C_L \alpha_L \rho_L U_L^2)}{\partial x} = & -\alpha_L \frac{\partial P_{L_i}}{\partial x} \\ & - \frac{\partial \alpha_L (P_L - P_{L_i})}{\partial x} - \alpha_L \rho_L g - \frac{\tau_w S_L}{A} + \frac{\tau_i S_i}{A} \end{aligned} \quad (3.8)$$

where C_ℓ is the momentum flux parameter of phase ℓ , P_ℓ represents the average phase pressure, P_{ℓ_i} represents the phase interface pressure, g is the gravity acceleration, τ_w and τ_i are the wall and interfacial shear stresses. S_L and S_i are the liquid phase wetted perimeter and interface perimeter. These parameters are defined in the next sections.

3.1 Geometric Parameters

For an annular flow pattern, the geometrical configuration illustrated in Figure 3.1 is considered

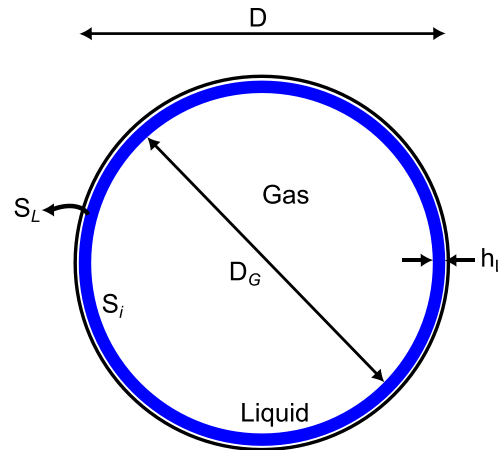


Figure 3.1 – Geometric Parameters.

where D is the pipe diameter and h_L the liquid film thickness. The gas diameter is

$$D_G = D - 2h_L \quad (3.9)$$

The liquid wetted perimeter S_L is equal to the pipeline perimeter, and the interface perimeter is S_i

$$S_L = \pi D \quad ; \quad S_i = \pi(D - 2h_L) \quad (3.10)$$

The phase hydraulic diameters can be written as a function of the areas and perimeters

$$D_{h_G} = \frac{4A_G}{S_i} \quad ; \quad D_{h_L} = \frac{4A_L}{S_L} \quad (3.11)$$

where A_G and A_L are the cross-section phase areas.

$$A_G = \frac{\pi}{4} D_G^2 \quad ; \quad A_L = \frac{\pi}{4} D^2 - A_G \quad (3.12)$$

The liquid film thickness can be related to the gas volumetric fraction with the following equation

$$h_L = \frac{D}{2} (1 - \sqrt{\alpha_G}) \quad (3.13)$$

The Reynolds numbers can be defined based on the phase velocity or phase superficial velocity

$$U_{s_\ell} = \alpha_\ell U_\ell \quad (3.14)$$

The Reynolds numbers for each phase and interface are defined as

$$Re_{sL} = \frac{\rho_L |U_{sL}| D}{\mu_L} ; \quad Re_{sG} = \frac{\rho_G |U_{sG}| D}{\mu_G} \quad (3.15)$$

$$Re_L = \frac{\rho_L |U_L| D_{hL}}{\mu_L} ; \quad Re_G = \frac{\rho_G |U_G| D_G}{\mu_G} \quad (3.16)$$

$$Re_i = \frac{\rho_G |U_G - U_L| D_{hi}}{\mu_G} \quad (3.17)$$

3.2 Boundary and initial conditions

Boundary and initial conditions must be defined in order to numerically solve the system of equations. In the inlet boundary conditions, the liquid and gas superficial velocities are imposed. The equilibrium film height is calculated from the superficial velocities and geometrical parameters. In the outlet boundary condition, the pressure is imposed.

Further, as initial conditions, the boundary values are prescribed to the entire computational domain.

3.3 Closure Models

Due to the averaging process of the 1D Two-Fluid Model, several parameters must be defined/modeled to close the one-dimensional system of equations and compensate the loss of information. These parameters are referred to as closure relations, and are defined below:

- Interfacial shear stress τ_i
- Wall shear stress τ_w
- The difference between phase and interface pressures ($P_\ell - P_{\ell i}$)
- The pressure jump over the interface ($P_{iG} - P_{iL}$)
- Momentum flux parameters C_ℓ
- Fluid densities ρ_L and ρ_G .

These parameters are modeled with simplified analytical or empirical formulations, that are, at times, limited to a particular flow configuration of interest. Significant effort has been made to develop physically accurate closure models to reintroduce information that has been lost during the averaging processes. Moreover, the effect of these parameters on the hyperbolicity of the system is of paramount importance and is the object of study of the present work.

3.3.1 Density

In most applications, the liquid phase can be approximate as constant. On the other hand, the gas density dependence in pressure is more significant and it is modelled here by the ideal gas law, as in many recent studies with gas-liquid two-phase flows (Issa & Kempf, 2003; Carneiro *et al.*, 2011; Pasqualetto, 2017; Fontalvo *et al.*, 2020).

$$\rho_G = \frac{P_G}{R_G T_{ref}} \quad (3.18)$$

where P_G is the gas bulk pressure, R_G is the gas constant, and T_{ref} is the reference temperature for isothermal flows. Since the pressure variation in the gas cross-section is small, the gas pressure is approximated by the interfacial gas pressure $P_G = P_{G_i}$.

3.3.2 Wall shear stress

The wall shear stress in the RHS of liquid momentum equation is defined in terms of a Fanning friction factor for the liquid phase, f_L :

$$\tau_w = \frac{1}{2} \rho_L f_L U_L |U_L| \quad (3.19)$$

Note that the modulus of the liquid velocity was employed here, to change the direction of the shear stress, in the event of a reverse flow.

Based on the recommendations of Inácio *et al.* (2012), Berna *et al.* (2014), Alves *et al.* (2012) and Fontalvo *et al.* (2020), the liquid friction factor correlation for vertical flows is defined as in Kosky & Staub (1971):

$$f_L = \begin{cases} \frac{16}{Re_{sL}} & Re_{sL} < 50 \\ \frac{12.7937}{Re_{sL}^{-0.9428}} & 50 \leq Re_{sL} < 1483 \\ \frac{0.081}{Re_{sL}^{-0.25}} & 1483 \leq Re_{sL} \end{cases} \quad (3.20)$$

3.3.3 Interfacial shear stress

The interfacial shear stress in the RHS momentum equations for the gas and liquid is also defined in terms of the Fanning friction factor as

$$\tau_i = \frac{1}{2} \rho_G f_i (U_G - U_{lf}) |U_G - U_{lf}| \quad (3.21)$$

where f_i is the interfacial friction factor and U_{lf} is the liquid film velocity at the interface.

Several correlations are available in the literature to model the interfacial friction factor, with varying rates of complexity. In general, most of the available correlations attempt to model the friction factor as a function of the single-phase gas flow friction factor and the liquid film thickness. The effect of the liquid film is modeled by assuming an interface roughness effect on the gas, similar to that of a solid rough wall. The elements of the interface roughness in annular flow are the interfacial waves, however, the difficulty to predict the wave heights has led many authors to propose correlations based on the film thickness (Sun *et al.*, 2018). Fontalvo *et al.* (2020) evaluated some prominent formulations based on the recommendations of Alves *et al.* (2017):

- (i) Wallis (1969) (Modified)

$$f_i = f_{iI} = \frac{0.079}{Re_{sG}^{0.25}} [1 + 180(1 - \sqrt{\alpha_G})] \quad (3.22)$$

- (ii) Whalley & Hewitt (1978)

$$f_i = f_{iII} = \frac{0.079}{Re_{sG}^{0.25}} \left[1 + 12 \left(\frac{\rho_L}{\rho_G} \right)^{1/3} (1 - \sqrt{\alpha_G}) \right] \quad (3.23)$$

- (iii) Belt *et al.* (2009)

$$f_i = f_{iIII} = 2 [3.413 \times 10^{-4} + 0.579(1 - \sqrt{\alpha_G})] \quad (3.24)$$

The liquid film velocity at the interface U_{lf} in Eq. (3.21) is usually approximated as the liquid phase velocity U_L . The present work evaluates other propositions based on works from the literature. Fowler & Lisseter (1992) suggested $U_{lf} = 2 U_L$, and Belt *et al.* (2009) recommend considering the wave velocity. Here, the wave velocity proposed by Berna *et al.* (2014) is employed.

- (a) U_{lf} model 1

$$U_{lf} = U_L \quad (3.25)$$

- (b) U_{lf} model 2

$$U_{lf} = 2 U_L \quad (3.26)$$

(c) U_{lf} model 3

$$U_{lf} = U_{wave} \quad (3.27)$$

The correlation for the wave velocity U_{wave} proposed by Berna *et al.* (2014) presents good agreement to experimental data, and it is given by

$$U_{wave} = \frac{\sqrt{\rho_G} U_{sG} + \sqrt{\rho_L} U_{sL}}{\sqrt{\rho_G} + \sqrt{\rho_L}} \frac{50 Re_{sL}^{0.16}}{Re_{sG}^{0.38} ST_w^{0.13}} \quad (3.28)$$

where ST_w and N_μ are the surface tension factor and viscosity number.

$$ST_w = 0.25 \quad \text{if } N_\mu > \frac{1}{15}$$

$$ST_w = \frac{0.028}{N_\mu^{0.8}} \quad \text{if } N_\mu \leq \frac{1}{15} \quad ; \quad N_\mu = \frac{\mu_L}{\sqrt{\rho_L} \sigma (\sigma / [g (\rho_L - \rho_G)])}^{0.5} \quad (3.29)$$

3.3.4 Phase and interface pressure difference

The relation $P_\ell - P_{\ell_i}$, in the momentum equations corresponds to the difference between the average phase pressure and its interface value. For horizontal flows, this difference is attributed to a hydrostatic effect (Issa & Kempf, 2003; Carneiro, 2006; Fontalvo, 2016), and its present in the equations is modeled as

$$-\frac{\partial \alpha_\ell (P_\ell - P_{\ell_i})}{\partial x} = -\rho_\ell \alpha_\ell \cos \beta \frac{\partial h_L}{\partial x} \quad (3.30)$$

For the vertical case, however, the hydrostatic effect is not present. This poses a significant problem for the stability of the system, as the absence of the hydrostatic pressure term renders the standard model unconditionally ill-posed. An alternative is to model the pressure term as a dynamic pressure based on the phase and interface relative velocity. Earlier works in this front date back to Stuhmiller (1977), and several authors have since improved upon the dynamic pressure formulation (e.g., Okawa & Kataoka, 2000). A general form of the term can be defined as (Fowler & Lisseter, 1992):

$$\Delta P_{dyn_\ell} = P_\ell - P_{\ell_i} = W_{f_\ell} \rho_{ref} (U_L - U_i)^2 \quad (3.31)$$

where W_{f_ℓ} is an empirical parameter, ρ_{ref} is a reference density and U_i is the interface velocity. Barbeau (2008) performed numerical analyses including a

dynamic pressure model, and concluded that for vertical flows, the dynamic pressure term is the only stabilizing term that maintains well-posedness.

Three models from the literature were selected to be evaluated. The Fowler & Lisseter (1992) model considers the liquid dynamic pressure term only, i.e., $W_{fG} = 0$. From recommendations in the literature (see Trapp, 1986; Serizawa & Kataoka, 1987), they define the liquid empirical parameter as $W_{fL} = 0.02$ for long waves. The reference density as $\rho_{ref} = \rho_L$ and the interface velocity is modeled as twice the value of the liquid phase velocity, $U_i = 2U_L$.

Bestion (1990) models the dynamic pressure of both phases, defining the reference density as a combined average $\rho_{ref} = \rho_m$, where

$$\rho_m = \frac{\alpha_L \alpha_G \rho_L \rho_G}{\alpha_G \rho_L + \alpha_L \rho_G} \quad (3.32)$$

and same empirical constant $W_{f\ell} = 1.2$ is employed for both phases, and the interface velocity is approximated as the gas core velocity $U_i = U_G$.

Lastly, Fontalvo *et al.* (2020) proposed a model based on the Fowler & Lisseter, however, the interface velocity carries the wave velocity model proposed in Berna *et al.* (2014), i.e., $W_{fL} = 0.02$; $\rho_{ref} = \rho_L$ and $U_i = U_{wave}$. The three models can be resumed as:

(i) Fowler & Lisseter (1992):

$$W_{fG} = 0 \ ; \ W_{fL} = 0.02 \ ; \ \rho_{ref} = \rho_L \ , \ U_i = 2 U_L \quad (3.33)$$

(ii) Bestion (1990):

$$W_{f\ell} = 1.2 \ , \text{with } \ell = G \ \text{and } L \ ; \ \rho_{ref} = \rho_m \ , \ U_i = U_G \quad (3.34)$$

(iii) Fontalvo *et al.* (2020)

$$W_{fG} = 0 \ ; \ W_{fL} = 0.02 \ ; \ \rho_{ref} = \rho_L \ , \ U_i = U_{wave} \quad (3.35)$$

3.3.5 Interface pressure jump

The interfacial pressure term in the momentum equations accounts for the pressure jump over the interface due to the gas-liquid surface tension. In a stability sense, surface tension acts as a stabilizing force in the system. The physical mechanism behind it is that the molecular interactions between the two phases

produce a counteracting force to the stretching of the surface through the increase in its curvature. This in turn limits the deformation that it undergoes due to external forces. The pressure difference is defined by the Young-Laplace equation

$$P_{iG} - P_{iL} = \sigma \kappa \quad (3.36)$$

where σ is the surface tension between the phases and κ is the curvature, which is defined as the inverse of the radius of curvature r_c :

$$\kappa = 1/r_c \quad (3.37)$$

For a very large curvature radius, i.e., flat surfaces, the effect of surface tension is negligible. For annular flow, however, two curvature radii are present, a transversal and an axial component. The axial component is responsible for the stabilization of the system of equation, contributing to well-posedness. The curvature is redefined in terms of both components

$$\kappa = \kappa_1 + \kappa_2 \quad (3.38)$$

where κ_1 and κ_2 represent the axial and longitudinal contributions, respectively. The axial curvature value can be estimated based on the liquid film thickness (Inada *et al.*, 2004; Carneiro, 2006)

$$\kappa_1 = \frac{\partial^2 h_L}{\partial x^2} = \frac{\partial h_L}{\partial \alpha_L} \frac{\partial^2 \alpha_L}{\partial x^2} + \left(\frac{\partial^2 h_L}{\partial \alpha_L^2} \right) \left(\frac{\partial \alpha_L}{\partial x} \right)^2 \quad (3.39)$$

where

$$\frac{\partial h_L}{\partial \alpha_L} = \frac{D}{4} \frac{1}{\sqrt{\alpha_G}} \quad ; \quad \frac{\partial^2 h_L}{\partial \alpha_L^2} = \frac{D}{8} \frac{1}{\alpha_G^{3/2}} \quad (3.40)$$

And the transversal component can be written as

$$\kappa_2 = \frac{2}{D - 2h_L} = \frac{2}{D \sqrt{\alpha_G}} \quad (3.41)$$

Several works have investigated the effect of surface tension effects on the flow. Montini (2010) performed a Kelvin-Helmholtz stability analysis of the system with the surface tension term and observed that it introduces a cut-off for short wavelength perturbations. However, numerical results showed that a mesh converged solution was not attained. Similarly, Inácio *et al.* (2012) showed that the

pressure jump increases the well-posed region in a stability map *only* when short wavelengths are captured.

3.3.6 Momentum flux parameter

In the standard Two-Fluid Model, the averaging process removes information regarding the velocity distribution in the cross-section, as only mean values are present in the formulation. It is akin to assuming that the velocity profile is completely flat for both phases, which may arguably be a reasonable approximation for the turbulent gas core flow. However, the complex changes occurring in the liquid film (i.e., formation of waves of various sizes) would clearly result in large variations in the velocity distribution.

The multiplying parameter C_ℓ in the convective term in the LHS of the momentum equations aims to restore some of that information. It is defined as

$$C_\ell = \frac{\overline{\langle u_\ell^2 \rangle}}{\langle u_\ell \rangle^2} = \frac{\langle \alpha_\ell u_\ell^2 \rangle}{\alpha_\ell U_\ell^2} = \frac{(1/A_\ell) \int_{A_\ell} u_\ell^2 d A_\ell}{\left[(1/A_\ell) \int_{A_\ell} u_\ell d A_\ell \right]^2} \quad (3.42)$$

which removes a common approximation that $\overline{\langle u_\ell^2 \rangle} = \langle u_\ell \rangle^2$.

The momentum flux parameter was first introduced by Song & Ishii (2000, 2001b), and they considered the parameter to be invariant in the flow direction, and a constant value based on inlet conditions and flow geometry was proposed. The procedure was to determine the gas and liquid momentum flux parameters from power law velocity and void fraction profiles. For annular flow, the calculated liquid momentum flux parameter C_L was approximately 1.05, and the gas momentum flux parameter C_G was approximately 1.02. They performed a characteristics analysis and showed that for the standard model, i.e., $C_L = 1$ and $P_\ell = P_{\ell i}$, the model is ill-posed for all conditions except equal phase velocities $U_G = U_L$, i.e., no acting interfacial shear. The introduction of a non-uniform velocity profile in the liquid phase ($C_L > 1$) had a positive effect towards stabilizing the system. It has been noted, however, that a $C_G > 1$ has the opposite effect, and decreases that well-posedness region (Song, 2003). We note that even though the gas momentum flux parameter destabilizes the flow, no evaluation of its effect on the accuracy of the model was carried out. Considering the turbulent nature of the gas core flow, the gas shape factor would realistically take a small value (equivalent to a turbulent power-law profile) such as 1.02. However, following the recommendations of the literature, the present work does not explore C_G .

Montini (2011) performed an extensive analysis of the influence of the shape factors for horizontal flow through an analysis of characteristics and has shown that an aggressive increase in the liquid shape factor, i.e., $C_L = 1.65$, value may render the entire slug flow region in the flow pattern map well-posed (Figure 3.2). They have also observed the destabilizing effect of the C_G value. Furthermore, numerical solutions were obtained by employing a C_L value that would position the pair of superficial velocities just inside the well-posed region. Mesh convergence was attained for these cases, whereas the standard model evaluated in Bonnizi (2003) for the same configurations did not converge.

However, the C_L values required to ensure well-posedness in these cases greatly overestimated the physical velocity profiles, and a careful analysis must be performed to ensure that physically sound hypotheses are being formulated when providing an *a priori* estimate for the shape factors.

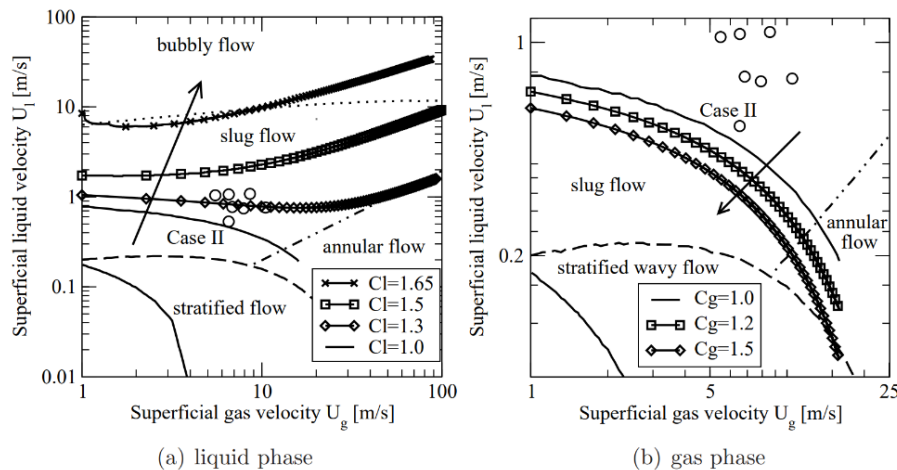


Figure 3.2 – Flow pattern stability map with varying C_L and C_G values (Montini, 2011).

For example, according to Inada *et al.* (2004), for high gas velocities, the velocity profile in the liquid film can be approximated as linear (i.e., Couette flow), which results in a $C_L = 1.33$ value. For low gas velocities, a parabolic profile with zero velocity at the wall and zero derivative at the interface is a reasonable approximation, which results in a C_L value of 1.20. For a turbulent velocity profile, the 1/7 power-law velocity profile renders a shape factor of $C_L = 1.02$. Several authors have numerically evaluated the introduction of the liquid momentum flux parameter, with varying rates of success (e.g., Inácio *et al.*, 2012). Fontalvo *et al.* (2020) tested C_L values of 1.00, 1.05, 1.20 and 1.33 against experimental data, and observed that the 1D Two-Fluid Model with $C_L = 1.05$ and a dynamic pressure model yielded the best agreement with experimental data.

The C_L has been shown to hold significant stabilizing properties. A $C_L > 1$ effectively decreases the relative velocity between the phases, which in turn diminishes the interfacial shear and increases the liquid film height.

4 A MODEL FOR THE MOMENTUM FLUX PARAMETER

The inclusion of a momentum flux parameter in the model equations reintroduces information regarding the flow distribution. It accounts for the non-uniformity of the velocity profile and void fraction in the cross-section. However, by employing a constant value, there is an implicit assumption that this distribution is constant in the axial direction, and it is evident from the formation of interfacial waves that the phase and velocity distributions vary throughout the domain.

Recent studies (Kushnir *et al.*, 2017; Bonzanini *et al.*, 2019) have employed pre-integrated models for a local estimation of the liquid and gas momentum flux parameter from theoretical velocity profiles. For annular flows, however, this has not been sufficiently explored. The current chapter aims to devise a model to better introduce information regarding the liquid velocity profiles into the standard Two-Fluid Model. A good starting point for the derivation is the definition of the phase momentum flux parameter

$$C_\ell = \frac{(1/A_\ell) \int_{A_\ell} u_\ell^2 d A_\ell}{\left[(1/A_\ell) \int_{A_\ell} u_\ell d A_\ell \right]^2} \quad (4.1)$$

Adapting the equation above for the liquid momentum flux parameter, considering the coordinate system of Figure 4.1, yields

$$C_L = \frac{\frac{1}{A_L} \int_{r_{hl}}^R u_L^2 r dr}{2 \pi \left[\frac{1}{A_L} \int_{r_{hl}}^R u_L r dr \right]^2} \quad (4.2)$$

where r_{hl} is the distance from the pipe centerline to the liquid film ($r_{hl} = R - h_L$) and $R = D/2$ is the pipeline radius. However, it is more convenient to use a coordinate system based on the distance from the wall y ($r = R - y$). Therefore, the integral can be rewritten in terms of y as

$$C_L = \frac{A_L \int_0^{h_L} u_L^2 (R - y) dy}{2 \pi \left[\int_0^{h_L} u_L (R - y) dy \right]^2} \quad (4.3)$$

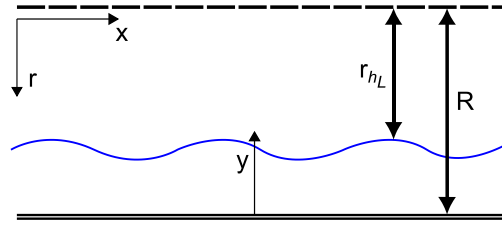


Figure 4.1 – Coordinate system for the liquid film MFP integration.

Furthermore, we define nondimensional quantities y^+ , u^+ , R^+ and h_L^+ in terms of a friction velocity $u_\tau = \sqrt{\tau_w/\rho_L}$ and kinematic viscosity $\nu_L = \mu_L/\rho_L$ as

$$u^+ = \frac{U_L}{u_\tau} ; \quad y^+ = y \frac{u_\tau}{\nu_L} ; \quad R^+ = \frac{R u_\tau}{\nu_L} ; \quad h_L^+ = \frac{h_L u_\tau}{\nu_L} \quad (4.4)$$

which results in

$$C_L = \frac{A_L u_\tau^2}{2 \pi \nu_L^2} \frac{\int_0^{h_L^+} (u^+)^2 (R^+ - y^+) dy^+}{\left[\int_0^{h_L^+} u^+ (R^+ - y^+) dy^+ \right]^2} \quad (4.5)$$

To integrate the momentum flux parameter, a model for the velocity profile must be provided.

4.1 Velocity profile models for annular flows

The prediction of a physically sound velocity distribution for the liquid phase is an ongoing study in the literature. A relation for turbulent liquid shear stress for thin liquid films can be applied for the continuous layer of the liquid film in annular flows as

$$\tau = \mu_t \frac{\partial u_L}{\partial y} \quad (4.6)$$

where μ_t is the turbulent viscosity. For annular flows, a common assumption is that the liquid film can be treated as a turbulent boundary layer. Thus, the effective viscosity can be correlated with the liquid viscosity from the Prandtl relationship (Dobran, 1983). For the viscous sublayer ($y^+ \leq y_{sub}^+$)

$$\frac{\mu_t}{\mu_L} = 1 \quad (4.7)$$

and for the turbulent layer ($y_{up}^+ < y^+ < h_L^+$)

$$\frac{\mu_t}{\mu_L} = K y^+ \tag{4.8}$$

where the transition, or buffer layer, is the region between the viscous sub-layer and turbulent layer ($y_{sub}^+ < y^+ < y_{up}^+$).

For thin liquid films, one can reasonably approximate the shear stress in Eq. (4.6) as $\tau = \tau_w$. Integrating Eq. (4.6) using Eqs. (4.7) and (4.8) yields

$$\begin{cases} u^+ = y^+ & , & y^+ \leq y_{sub}^+ \\ u^+ = \frac{1}{K} \ln y^+ + A & , & y^+ \geq y_{up}^+ \end{cases} \tag{4.9}$$

The constant K is the von-Kármán constant ($K = 0.4$) and A is an empirical constant, related to the boundary condition. A common approximation of single-phase flow yields the so-called Universal Velocity Profile (UVP) (Dobran, 1983):

$$\begin{cases} u^+ = y^+ & , & 0 < y^+ \leq y_{sub}^+ \\ u^+ = 5 \ln y^+ - 3 & , & y_{sub}^+ < y^+ < y_{up}^+ \\ u^+ = 2.5 \ln y^+ + 5.5 & , & y_{up}^+ \leq y^+ \leq h_L^+ \end{cases} \tag{4.10}$$

Experimental works have shown that the standard UVP is unable to adequately predict the velocity profile for annular liquid films. Figure 4.2 displays the non-dimensional velocity profile experimental data of Vassalo (1999) for annular flows. It shows that the UVP (continuous line) overpredicts the magnitude of the liquid film velocity profiles and only shows good agreement for the null gas superficial velocity, i.e., single phase liquid flow.

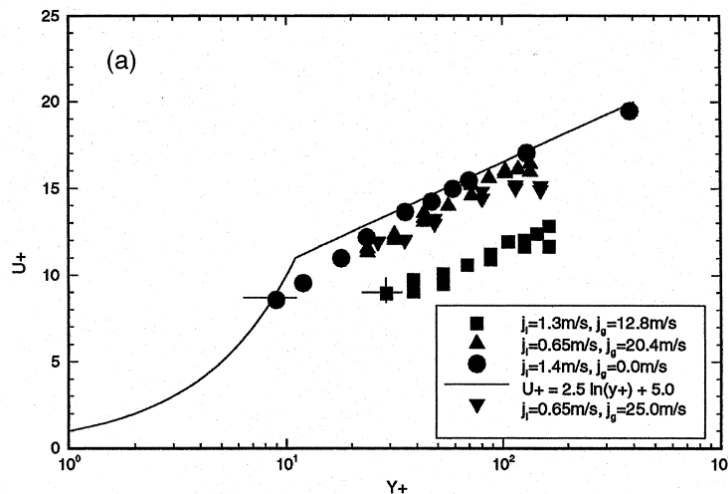


Figure 4.2 –Experimental data of velocity profiles compared against the standard UVP (Vassalo, 1999).

A more recent study performed by Ashwood *et al.* (2015) has shown that the standard velocity profile underpredicts experimental data for annular flow in a square cross-section pipe (see continuous line in Figure 4.3). As can be noted, these separate experimental studies yield conflicting results regarding the accuracy of the UVP for liquid films. Modifications have been proposed to the standard UVP to better predict the velocity profile of wavy liquid films of annular flows. In the work of Ashwood *et al.* (2015), a correction for the constants of the standard UVP is provided to better fit the experimental results (see dashed line in Fig. Figure 4.3).

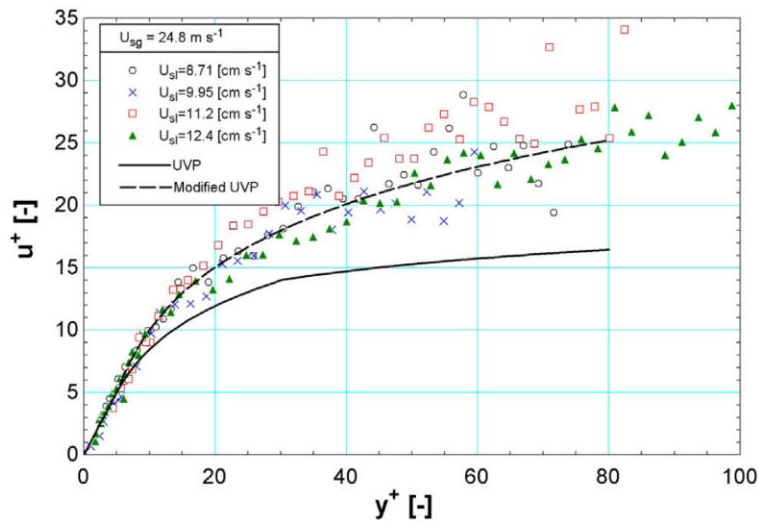


Figure 4.3 –Comparison of the standard UVP and a modified UVP against the experimental data of Ashwood *et al.* (2015).

The modified velocity profile is written below

$$\begin{cases} u^+ = y^+ & , & 0 \leq y^+ \leq y_{sub}^+ \\ u^+ = 7.2 \ln y^+ + 6.6 & , & y_{sub}^+ < y^+ < y_{up}^+ \\ u^+ = 7.38 \ln y^+ - 7.1 & , & y_{up}^+ \leq y^+ \leq h_L^+ \end{cases} \quad (4.11)$$

In these cases, the threshold for the viscous sublayer is $y_{sub}^+ = 5$, and the buffer layer threshold is $y_{up}^+ = 30$, which are typical values for single-phase boundary layer flows. Based on the results of Ashwood *et al.* (2015), Cioncolini *et al.* (2015) proposed new limits for the molecular sublayer, buffer, and turbulent layers, that are arguably more appropriate to shear-driven annular liquid films. In their work, the revised bounds for each region are $y_{sub}^+ = 9$ and $y_{up}^+ = 40$. However, it is yet to be thoroughly assessed with other experimental configurations.

The scarcity of experimental data on liquid film velocity profiles and the underperformance of available models presents a significant obstacle in the development of physically accurate formulations for the momentum flux parameter. In light of this discussion, two velocity profile models are proposed in the present work:

(i) Model I

The first velocity profile model is based on a simplified version of the standard UVP, with a viscous sublayer and a full turbulent layer. The logarithmic profile of the turbulent layer is adjusted in order to couple the velocity distribution in the liquid film with the gas core region through the interfacial shear stress. We argue that imposing a link between the velocity distributions of both phases is consistent with a two-fluid formulation. The proposed velocity profile is defined as

$$\begin{cases} u^+ = y^+ & , & 0 \leq y^+ \leq y_{sub}^+ \\ u^+ = a \ln y^+ + b & , & y_{sub}^+ < y^+ \leq h_L^+ \end{cases} \quad (4.12)$$

where $y_{sub}^+ = 11$. Applying Eq. (4.6) to the interface yields

$$\tau_i = \mu_t \frac{\partial U_L}{\partial y} \quad (4.13)$$

Using the turbulent mixing length approximation for the logarithm portion of the velocity profile

$$\mu_t = \rho_L u_\tau \ell = \rho_L u_\tau A y \quad (4.14)$$

where ℓ represents the mixing length, $A = 0.14$ is an empirical constant. The non-dimensional form of the resulting equation is

$$\tau_i = \rho_L u_\tau^2 A y^+ \frac{\partial u^+}{\partial y^+} \quad (4.15)$$

Defining a nondimensional shear stress as

$$\tau_i^+ = \frac{\tau_i}{\rho_L u_\tau^2} \quad (4.16)$$

and integrating Eq. (4.15) yields the following velocity profile equation

$$u^+ = \frac{\tau_i^+}{A} \ln y^+ + C \quad (4.17)$$

Therefore, the first coefficient is given by

$$a = \frac{\tau_i^+}{0.14} \quad (4.18)$$

The velocity at y_{sub}^+ is known from the linear velocity profile

$$u^+(y_{sub}^+) = y_{sub}^+ \quad (4.19)$$

which yields

$$b = y_{sub}^+ - \frac{\tau_i^+}{0.14} \ln y_{sub}^+ \quad (4.20)$$

(ii) Model II

The second velocity profile model proposed in this work is based on the modifications of the standard UVP proposed in Cioncolini *et al.* (2015). It is defined as

$$\begin{cases} u^+ = y^+ & , & 0 < y^+ \leq y_{sub}^+ \\ u^+ = a \ln y^+ + b & , & y_{sub}^+ < y^+ < y_{up}^+ \\ u^+ = c \ln y^+ + d & , & y_{up}^+ \leq y^+ < h_L^+ \end{cases} \quad (4.21)$$

The first logarithmic profile $u^+ = a \ln y^+ + b$ has the following restrictions

$$u^+(y_{sub}^+) = y_{sub}^+ \quad ; \quad \left. \frac{\partial u^+}{\partial y^+} \right|_{y_{sub}^+} = 1 \quad (4.22)$$

which yield the following coefficients

$$a = y_{sub}^+ \quad ; \quad b = y_{sub}^+ (1 - \ln y_{sub}^+) \quad (4.23)$$

The constant of the logarithmic profile from $y_{up}^+ \leq y^+ < h_L^+$ are determined based on the interface film velocity $u^+(h_L^+)$, and by guaranteeing continuity of velocity at y_{up}^+ , thus

$$c = \frac{a \ln y_{up}^+ + b - u^+(h_L^+)}{\ln y_{up}^+ - \ln h_L^+} \quad ; \quad d = u^+(h_L^+) - c \ln h_L^+ \quad (4.24)$$

4.2 MFP pre-integrated models

With the new velocity profile models for annular flows, one can obtain the momentum flux parameter from Eq. (4.5) as rewritten below

$$C_L = \frac{A_L u_\tau^2}{2\pi v_L^2} \frac{\int_0^{h_L^+} (u^+)^2 (R^+ - y^+) dy^+}{\left[\int_0^{h_L^+} u^+ (R^+ - y^+) dy^+ \right]^2} \quad (4.25)$$

For each model, the velocity profile can be decomposed into its linear and logarithmic components.

(i) Model I

Model I has two profile components, which are decomposed as shown below

$$C_L = \frac{A_L u_\tau^2}{2\pi v_L^2} \frac{\mathcal{A}1 + \mathcal{B}1}{[\mathcal{A}2 + \mathcal{B}2]^2} \quad (4.26)$$

where the coefficients

$$\mathcal{A}1 = \int_0^{y_{sub}^+} y^{+2} (R^+ - y^+) dy^+ \quad ; \quad \mathcal{B}1 = \int_{y_{sub}^+}^{h_L^+} (a \ln y^+ + b)^2 (R^+ - y^+) dy^+ \quad (4.27)$$

$$\mathcal{A}2 = \int_0^{y_{sub}^+} y^+ (R^+ - y^+) dy^+ \quad ; \quad \mathcal{B}2 = \int_{y_{sub}^+}^{h_L^+} (a \ln y^+ + b) (R^+ - y^+) dy^+ \quad (4.28)$$

represent the decomposed integrals for each velocity profile. The results of these integrals are shown below

$$\mathcal{A}1 = y_{sub}^{+3} \left(\frac{R^+}{3} - \frac{1}{4} y_{sub}^+ \right) \quad ; \quad \mathcal{A}2 = y_{sub}^{+2} \left(\frac{R^+}{2} - \frac{1}{3} y_{sub}^+ \right) \quad (4.29)$$

$$\begin{aligned} \mathcal{B}1 = h_L^+ \left\{ (a \ln h_L^+ + b) \left[(a \ln h_L^+ + b) \left(R^+ - \frac{1}{2} h_L^+ \right) - 2a \left(R^+ - \frac{1}{4} h_L^+ \right) \right] \right. \\ \left. + a^2 \left(2R^+ - \frac{1}{4} h_L^+ \right) \right\} \\ - y_{sub}^+ \left\{ (a \ln y_{sub}^+ + b) \left[(a \ln y_{sub}^+ + b) \left(R^+ - \frac{1}{2} y_{sub}^+ \right) \right. \right. \\ \left. \left. - 2a \left(R^+ - \frac{1}{4} y_{sub}^+ \right) \right] + a^2 \left(2R^+ - \frac{1}{4} y_{sub}^+ \right) \right\} \end{aligned} \quad (4.30)$$

$$\begin{aligned} \mathcal{B}2 = h_L^+ \left\{ (a \ln h_L^+ + b) \left(R^+ - \frac{1}{2} h_L^+ \right) - a \left(R^+ - \frac{1}{4} h_L^+ \right) \right\} \\ - y_{sub}^+ \left\{ (a \ln y_{sub}^+ + b) \left(R^+ - \frac{1}{2} y_{sub}^+ \right) - a \left(R^+ - \frac{1}{4} y_{sub}^+ \right) \right\} \end{aligned} \quad (4.31)$$

(ii) Model II

Model II has one linear and two logarithmic velocity profiles. A similar procedure to the first model is taken here, with additional components $\mathcal{C}1$ and $\mathcal{C}2$ that represent the second logarithmic profile of Eq. (4.21).

$$C_L = \frac{A_L u_t^2}{2\pi \nu_t^2} \frac{\mathcal{A}1 + \mathcal{B}1 + \mathcal{C}1}{[\mathcal{A}2 + \mathcal{B}2 + \mathcal{C}2]^2} \quad (4.32)$$

$$\mathcal{A}1 = \int_0^{y_{sub}^+} y^{+2} (R^+ - y^+) dy^+ ; \quad \mathcal{B}1 = \int_{y_{sub}^+}^{h_L^+} (a \ln y^+ + b)^2 (R^+ - y^+) dy^+ \quad (4.33)$$

$$\mathcal{A}2 = \int_0^{y_{sub}^+} y^+ (R^+ - y^+) dy^+ ; \quad \mathcal{B}2 = \int_{y_{sub}^+}^{h_L^+} (a \ln y^+ + b) (R^+ - y^+) dy^+ \quad (4.34)$$

$$\mathcal{C}1 = \int_{y_{up}^+}^{h_L^+} (c \ln y^+ + d)^2 (R^+ - y^+) dy^+ \quad (4.35)$$

$$\mathcal{C}2 = \int_{y_{up}^+}^{h_L^+} (c \ln y^+ + d) (R^+ - y^+) dy^+ \quad (4.36)$$

The resulting integrals are defined as

$$\mathcal{A}1 = y_{sub}^{+3} \left(\frac{R^+}{3} - \frac{1}{4} y_{sub}^+ \right) ; \quad \mathcal{A}2 = y_{sub}^{+2} \left(\frac{R^+}{2} - \frac{1}{3} y_{sub}^+ \right) \quad (4.37)$$

$$\begin{aligned} \mathcal{B}1 = y_{up}^+ \left\{ (a \ln y_{up}^+ + b) \left[(a \ln y_{up}^+ + b) \left(R^+ - \frac{1}{2} y_{up}^+ \right) - 2a \left(R^+ - \frac{1}{4} y_{up}^+ \right) \right] \right. \\ \left. + a^2 \left(2R^+ - \frac{1}{4} y_{up}^+ \right) \right\} \\ - y_{sub}^+ \left\{ (a \ln y_{sub}^+ + b) \left[(a \ln y_{sub}^+ + b) \left(R^+ - \frac{1}{2} y_{sub}^+ \right) \right. \right. \\ \left. \left. - 2a \left(R^+ - \frac{1}{4} y_{sub}^+ \right) \right] + a^2 \left(2R^+ - \frac{1}{4} y_{sub}^+ \right) \right\} \end{aligned} \quad (4.38)$$

$$\begin{aligned}
C1 = h_L^+ \left\{ (c \ln h_L^+ + d) \left[(c \ln h_L^+ + d) \left(R^+ - \frac{1}{2} h_L^+ \right) - 2c \left(R^+ - \frac{1}{4} h_L^+ \right) \right] \right. \\
\left. + c^2 \left(2R^+ - \frac{1}{4} h_L^+ \right) \right\} \\
- y_{up}^+ \left\{ (c \ln y_{up}^+ + d) \left[(c \ln y_{up}^+ + d) \left(R^+ - \frac{1}{2} y_{up}^+ \right) \right. \right. \\
\left. \left. - 2c \left(R^+ - \frac{1}{4} y_{up}^+ \right) \right] + c^2 \left(2R^+ - \frac{1}{4} y_{up}^+ \right) \right\}
\end{aligned} \tag{4.39}$$

$$\begin{aligned}
B2 = y_{up}^+ \left\{ (a \ln y_{up}^+ + b) \left(R^+ - \frac{1}{2} y_{up}^+ \right) - a \left(R^+ - \frac{1}{4} y_{up}^+ \right) \right\} \\
- y_{sub}^+ \left\{ (a \ln y_{sub}^+ + b) \left(R^+ - \frac{1}{2} y_{sub}^+ \right) - a \left(R^+ - \frac{1}{4} y_{sub}^+ \right) \right\}
\end{aligned} \tag{4.40}$$

$$\begin{aligned}
C2 = h_L^+ \left\{ (c \ln h_L^+ + d) \left(R^+ - \frac{1}{2} h_L^+ \right) - c \left(R^+ - \frac{1}{4} h_L^+ \right) \right\} \\
- y_{up}^+ \left\{ (c \ln y_{up}^+ + d) \left(R^+ - \frac{1}{2} y_{up}^+ \right) - c \left(R^+ - \frac{1}{4} y_{up}^+ \right) \right\}
\end{aligned} \tag{4.41}$$

The pre-integrated models defined above allow for the estimation of a liquid momentum flux parameter. The procedure to obtain the C_L values from the local flow quantities is described below.

- i) Obtain the liquid and gas phase velocities.
- ii) Obtain or calculate the liquid film thickness h_L , either from simulation results or from an equilibrium estimate (see Appendix A).
- iii) Calculate the wall and interfacial shear stresses (Eq. (3.19) and (3.21)) and the non-dimensional liquid film height h_L^+ .
- iv) Identify in which region of the velocity profile model the liquid film h_L^+ is located.
- v) Integrate Eq. (4.25) and (4.26) in the range of $y^+ = [0, h_L^+]$ to obtain the C_L value.

Figure 4.4 shows a map of the variation of the liquid momentum flux parameter as a function of the superficial velocities for an annular flow configuration of diameter $D = 34.5\text{mm}$. It illustrates the dependence of the C_L on the phase velocities. In this test, the wall shear stress was obtained from the friction factor model of Kosky & Staub (1971), Eq. (3.20), and the interfacial shear stress was obtained from the friction factor model of Whalley & Hewitt (1978), Eq. (3.23). The liquid film thickness was approximated by the equilibrium film height, described in Appendix A. A clear dependency on the liquid superficial velocity U_{sL} can be observed, with a very small dependency on the gas superficial velocity U_{sG} .

As expected, the low liquid superficial velocities yield higher relative phase velocities, which promotes a thinner liquid film configuration. The resulting velocity profile for thin films are expected to be linear, which leads to higher C_L values. As the liquid superficial velocity increases, the C_L value naturally increases as well.

The results of Figure 4.4 are obtained from the equilibrium state for a particular set of initial conditions. For a numerical simulation, however, the formation of waves will result in large local variations in the liquid phase velocity and void fraction, and the C_L value will naturally oscillate between higher values in the unperturbed region in-between-waves, and lower values in the disturbance waves.

In light of this discussion, Figure 4.5 shows the variation of the liquid momentum flux parameter with the liquid Reynolds numbers Re_L (Eq. (3.16)). This is carried out by fixing the gas superficial velocity, varying only the liquid superficial velocity to obtain the equilibrium configuration. The models show a similar behavior, where for very thin films (low Reynolds number), the C_L value is approximately 1.334, which corresponds to a linear velocity profile, as expected. As Re_L increases, the C_L curves undergo a steep decline, converging to very low values, corresponding to flatter velocity profiles. Model II presents a more significant decline in C_L for low Reynolds numbers, however, both models converge similarly for higher Re_L .

To further illustrate the behavior of the momentum flux parameter models, the data from the Ashwood *et al.* (2015) velocity profiles (Figure 4.3) were integrated to obtain a rough estimate of the experimental momentum flux parameter values. Figure 4.6 presents the experimental integrated profiles and the estimations of the models devised in the present work. Although it is a rough estimation of the velocity profiles, and the experimental set-up is a square duct, a similar trend is obtained by both models

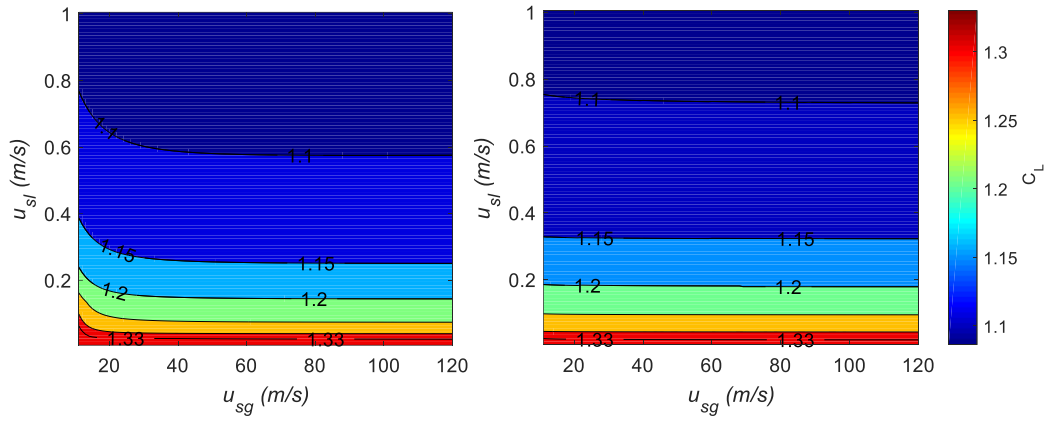


Figure 4.4 - C_L maps for Model I (left) and Model II (right).

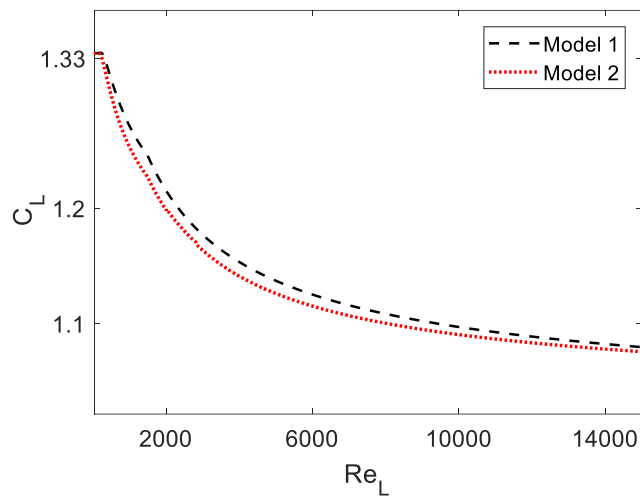


Figure 4.5 - C_L variation with the liquid Reynolds number for both models.

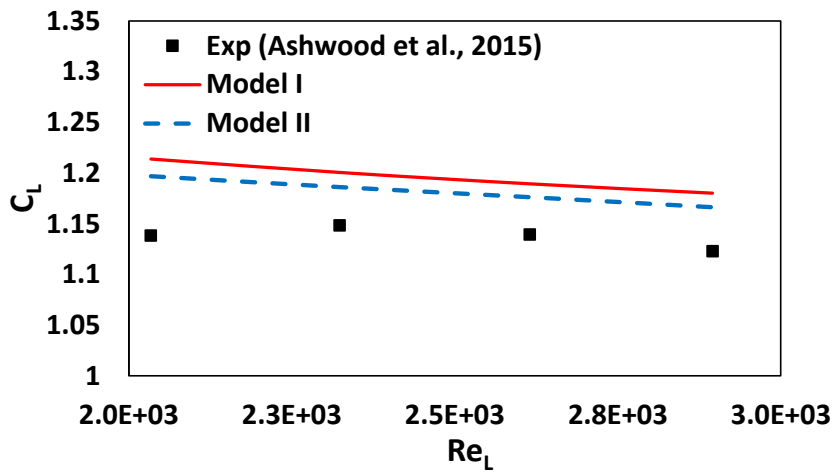


Figure 4.6 Comparison between the experimental C_L estimate and the developed models.

4.3 MFP simplified models

Although the use of pre-integrated models for the momentum flux parameter is more physically sound in comparison to constant C_ℓ values, it comes at an additional computational cost. That is especially the case due to the use of a UVP, where the velocity profile is subdivided in different regions. In a numerical simulation, in order to adequately integrate the profile, several conditional statements must be used, for every computational control volume, at each time step.

A solution to this issue can be through the definition of a simplified model. We observe that the MFP models devised in this work show a dependence on the liquid phase velocity and phase fraction, as expected. Thus, by fitting a power series model in the curves presented in Figure 4.5, i.e., assuming a dependence on the liquid Reynolds number only, a simplified model can be obtained. The model is of the form

$$\begin{cases} C_L = 1.334 & , & Re_L \leq Re_c \\ C_L = mRe_L^n + b & , & Re_L > Re_c \end{cases} \quad (4.42)$$

For Model I, the coefficients are

$$m = 1.3703 \quad ; \quad n = -0.12517 \quad ; \quad b = 0.66361 \quad ; \quad Re_c = 303 \quad (4.43)$$

and for Model II, the coefficients are

$$m = 2.0152 \quad ; \quad n = -0.29273 \quad ; \quad b = 0.97945 \quad ; \quad Re_c = 314 \quad (4.44)$$

5 NUMERICAL METHODOLOGY

The numerical solution of the equations system for the 1D Two Fluid model is performed with the finite volume method (FVM) (Patankar, 1980). In this methodology, the spatial domain is subdivided into control volumes. The transport equations are integrated in time and space at each volume, creating an algebraic system of equations for the set of discrete volumes.

A staggered grid is employed to minimize the instabilities of an oscillating pressure field, according to recommendations of Patankar (1980). Scalar variables (pressure, phase fractions) are stored in the center of the scalar control volumes, i.e., the nodal points, and the velocities are stored in the center of the vector control volumes, i.e., the faces. Figure 5.1 illustrates the layout of the control volumes. The uppercase symbols represent the nodal points P (principal), E (east), W (west), etc. whereas the lowercase symbols (e.g., e , w) represent the volume faces.

At the present work, a uniform mesh spacing was employed, with the control volume face stored half distance from the nodal points. The symbols Δx and δx represent the length of the scalar and vector control volumes, respectively. Since the mesh spacing is constant, $\Delta x = \delta x$.

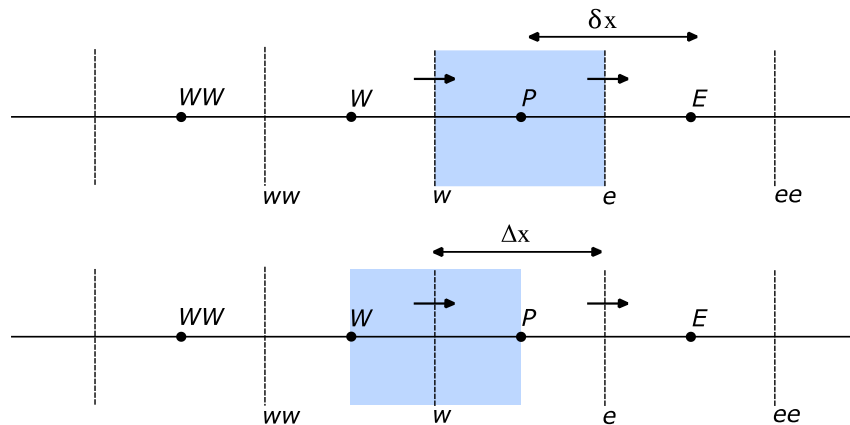


Figure 5.1 - Mesh layout (Scalar and vector control volumes).

The present work expands on an in-house code developed by the Computational Fluid Dynamics Group (DFC) from the Department of Mechanical Engineering of PUC-Rio, by introducing the variable momentum flux parameters

formulation. The discretization of the equations for phase fractions, velocities and pressure are performed following the works of Ortega & Nieckele (2005), Carneiro *et al.* (2011), Siqueira *et al.* (2019) and Fontalvo *et al.* (2020) and are laid out in this section.

5.1 Gas Volume Fraction

The gas volume fraction field is obtained from the gas mass conservation equation. The discrete equation is obtained by time and space integrations in the scalar control volume (where $dV = A dx$), as shown below, where the order of integration is changed depending on the term being integrated as

$$\int_w^e \int_t^{t+\Delta t} \frac{\partial \alpha_G \rho_G}{\partial t} dt A dx + \int_t^{t+\Delta t} \int_w^e \frac{\partial \alpha_G \rho_G U_G}{\partial x} A dx dt = 0 \quad (5.1)$$

The temporal discretization is performed with a first order forward Euler method, which yields

$$\frac{(\rho_G \alpha_G)_P - (\rho_G \alpha_G)_P^o}{\Delta t} A \Delta x + \tilde{F}_{G_e} \alpha_{G_e} - \tilde{F}_{G_w} \alpha_{G_w} = 0 \quad (5.2)$$

where the superscript o denotes the previous time instant, and a subscript is omitted for the current time step, corresponding to $t + \Delta t$. \tilde{F} is a pseudo mass flux evaluated at the faces e and w , defined below

$$\tilde{F}_{G_e} = \hat{\rho}_{G_e} U_{G_e} A \quad ; \quad \tilde{F}_{G_w} = \hat{\rho}_{G_w} U_{G_w} A \quad (5.3)$$

where in order to evaluate the gas density in the faces of the control volume, the Upwind scheme is employed

$$\hat{\rho}_{G_e} = \llbracket \text{sign}(U_{G_e}), 0 \rrbracket \rho_{G_P} - \llbracket \text{sign}(U_{G_e}), 0 \rrbracket \rho_{G_E} \quad (5.4)$$

$$\hat{\rho}_{G_w} = \llbracket \text{sign}(U_{G_w}), 0 \rrbracket \rho_{G_W} - \llbracket \text{sign}(U_{G_w}), 0 \rrbracket \rho_{G_P} \quad (5.5)$$

Following the procedure undertaken in Fontalvo (2016), a TVD Total Variation Diminishing (Versteeg & Malalalsekera, 2007) is employed for the spatial interpolation of the variables in the control volume faces. The TVD consists of a second order scheme that minimizes the numerical diffusion issue of low order schemes. The TVD approximation of the volumetric fraction in the

faces of a control volume are

$$F_{G_e} = \tilde{F}_{G_e} \alpha_{G_e} = \llbracket \tilde{F}_{G_e}, 0 \rrbracket \alpha_{G_P} - \llbracket -\tilde{F}_{G_e}, 0 \rrbracket \alpha_{G_E} - |\tilde{F}_{G_e}| \frac{\Psi(r_{\alpha_{G_e}})}{2} (\alpha_{G_P} - \alpha_{G_E}) \quad (5.6)$$

$$\tilde{F}_{G_w} \alpha_{G_w} = \llbracket \tilde{F}_{G_w}, 0 \rrbracket \alpha_{G_W} - \llbracket -\tilde{F}_{G_w}, 0 \rrbracket \alpha_{G_E} - |\tilde{F}_{G_w}| \frac{\Psi(r_{\alpha_{G_w}})}{2} (\alpha_{G_W} - \alpha_{G_P}) \quad (5.7)$$

where the $\llbracket \cdot \rrbracket$ operator represents the maximum between two quantities. Ψ is the flux limiter function of the TVD scheme, which is dependent on the relation between the Upwind and Downwind gradients r , defined below

$$r_{\alpha_{G_e}} = \llbracket \text{sign}(U_{G_e}), 0 \rrbracket \frac{\alpha_{G_P} - \alpha_{G_W}}{\alpha_{G_E} - \alpha_{G_P}} + \llbracket -\text{sign}(U_{G_e}), 0 \rrbracket \frac{\alpha_{G_{EE}} - \alpha_{G_E}}{\alpha_{G_E} - \alpha_{G_P}} \quad (5.8)$$

$$r_{\alpha_{G_w}} = \llbracket \text{sign}(U_{G_w}), 0 \rrbracket \frac{\alpha_{G_W} - \alpha_{G_{WW}}}{\alpha_{G_P} - \alpha_{G_W}} + \llbracket -\text{sign}(U_{G_w}), 0 \rrbracket \frac{\alpha_{G_E} - \alpha_{G_P}}{\alpha_{G_P} - \alpha_{G_W}} \quad (5.9)$$

The flux limiter function selected in this work is the Van Leer function (Van Leer, 1974), as it has been adopted extensively in the literature, with positive results (Fontalvo *et al.*, 2020; Castello Branco *et al.*, 2021). The Van Leer flux limiter is defined as

$$\Psi(r) = \frac{r + |r|}{1 + r} \quad (5.10)$$

Note that by defining $\Psi(r) = 0$, the first order Upwind scheme is recovered.

The resulting algebraic gas mass conservation equation can be written as

$$a_P \alpha_{G_P} = a_E \alpha_{G_E} + a_W \alpha_{G_W} + b^{\alpha_G} \quad (5.11)$$

where the coefficients a_P , a_E and a_W are

$$a_E = \llbracket -\tilde{F}_{G_e}, 0 \rrbracket ; \quad a_W = \llbracket \tilde{F}_{G_w}, 0 \rrbracket ; \quad a_P^o = \rho_{G_P}^o A \frac{\Delta x}{\Delta t} \quad (5.12)$$

$$a_P = \rho_{G_P} A \frac{\Delta x}{\Delta t} + \llbracket \tilde{F}_{G_e}, 0 \rrbracket + \llbracket -\tilde{F}_{G_w}, 0 \rrbracket$$

and the source term b is defined as

$$b^{\alpha_G} = a_P^o \alpha_{G_P}^o + b_{TVD}^{\alpha_G} \quad (5.13)$$

where the TVD source term is written below

$$b_{TVD}^{\alpha_G} = -|\tilde{F}_{G_e}| \frac{\Psi(r_{\alpha_{G_e}})}{2} (\alpha_{G_P} - \alpha_{G_e}) - |\tilde{F}_{G_w}| \frac{\Psi(r_{\alpha_{G_w}})}{2} (\alpha_{G_W} - \alpha_{G_P}) \quad (5.14)$$

5.2 Velocities

The gas and liquid phase velocities are obtained from the momentum equations, (3.7) and (3.8). A similar procedure to obtain the gas volume fraction from the mass conservation equation is employed here. As previously noted, the control volume for the velocity discretization is face centered. The momentum equations for phase k can be rewritten in a more convenient form as

$$\frac{\partial(\alpha_\ell \rho_\ell U_\ell)}{\partial t} + \frac{\partial(C_\ell \alpha_\ell \rho_\ell U_\ell^2)}{\partial x} = -\alpha_\ell \frac{\partial P}{\partial x} + S_{c_\ell} + S_{p_\ell} U_\ell \quad (5.15)$$

where $P = P_{G_i}$ is the interface gas pressure, S_{c_ℓ} and S_{p_ℓ} are source terms of phase ℓ . The integrated form of Eq. (5.15) is shown below

$$\begin{aligned} \frac{\tilde{\rho}_{\ell_w} \tilde{\alpha}_{\ell_w} U_{\ell_w} - \tilde{\rho}_\ell^o \tilde{\alpha}_{\ell_w}^o U_{\ell_w}^o}{\Delta t} A dx + [C_{\ell_P} F_{\ell_P} U_{\ell_P} - C_{\ell_W} F_{\ell_W} U_{\ell_W}] \\ = -\tilde{\alpha}_{\ell_w} (P_P - P_W) A + (S_{c_\ell} + S_{p_\ell} U_\ell) A dx \end{aligned} \quad (5.16)$$

In the discretized momentum equation, the transient and pressure term are based on the face properties evaluated by a simple interpolation from the nodal points, which for a uniform mesh is

$$\tilde{\rho}_{\ell_w} = \frac{1}{2} (\rho_{\ell_P} + \rho_{\ell_W}) \quad ; \quad \tilde{\alpha}_{\ell_w} = \frac{1}{2} (\alpha_{\ell_P} + \alpha_{\ell_W}) \quad (5.17)$$

and the mass fluxes of phase ℓ evaluated in the nodal points are obtained from an average value of the mass fluxes in the faces of the control volume, as

$$F_{\ell_P} = \alpha_{\ell_P} \rho_{\ell_P} U_{\ell_P} A = \frac{F_{\ell_w} + F_{\ell_e}}{2} \quad (5.18)$$

$$F_{\ell_W} = \alpha_{\ell_W} \rho_{\ell_W} U_{\ell_W} A = \frac{F_{\ell_{ww}} + F_{\ell_w}}{2} \quad (5.19)$$

The face values of the mass fluxes are

$$F_{\ell_e} = \tilde{F}_{\ell_e} \hat{\alpha}_{\ell_e} ; \quad F_{\ell_w} = \tilde{F}_{\ell_w} \hat{\alpha}_{\ell_w} ; \quad F_{k_{ww}} = \tilde{F}_{ww} \hat{\alpha}_{\ell_{ww}} \quad (5.20)$$

where the face volume fraction is determined with the Upwind approximation

$$\hat{\alpha}_{\ell_e} = \llbracket \text{sign}(U_{\ell_e}), 0 \rrbracket \alpha_{\ell_P} - \llbracket \text{sign}(U_{\ell_e}), 0 \rrbracket \alpha_{\ell_E} \quad (5.21)$$

$$\hat{\alpha}_{\ell_w} = \llbracket \text{sign}(U_{\ell_w}), 0 \rrbracket \alpha_{\ell_W} - \llbracket \text{sign}(U_{\ell_w}), 0 \rrbracket \alpha_{G_{\ell_P}} \quad (5.22)$$

The momentum flux term, can be determined in the nodal points with the TVD approximation as

$$F_{\ell_P} U_{\ell_P} = \llbracket F_{\ell_P}, 0 \rrbracket U_{\ell_w} - \llbracket -F_{\ell_P}, 0 \rrbracket U_{\ell_e} - |F_{\ell_P}| \frac{\Psi_P}{2} (U_{\ell_w} - U_{\ell_e}) \quad (5.23)$$

$$F_{\ell_W} U_{\ell_W} = \llbracket F_{\ell_W}, 0 \rrbracket U_{\ell_{ww}} - \llbracket -F_{\ell_W}, 0 \rrbracket U_{\ell_w} - |F_{\ell_W}| \frac{\Psi_W}{2} (U_{\ell_{ww}} - U_{\ell_w}) \quad (5.24)$$

The point values of the momentum flux parameter C_ℓ are obtained from the average of the neighboring faces as shown below

$$C_{\ell_P} = \frac{C_{\ell_e} + C_{\ell_w}}{2} ; \quad C_{\ell_W} = \frac{C_{\ell_{ww}} + C_{\ell_w}}{2} \quad (5.25)$$

The discretized momentum equation can then be rearranged in the form

$$a_{\ell_w} U_{\ell_w} = a_{\ell_{ww}} U_{\ell_{ww}} + a_{\ell_e} U_{\ell_e} + b^{U_\ell} + (1 - \gamma) \frac{a_{\ell_w}}{\gamma} U_{\ell_w}^* - \tilde{\alpha}_{\ell_w} A (P_P - P_W) \quad (5.26)$$

where γ is the under-relaxation factor, that controls the stability of the iterative process. It effectively carries the solution from a previous iteration $U_{\ell_w}^*$ into the current iteration. Its value was kept at $\gamma = 0.7$. The coefficients of Eq. (5.26) are shown below

$$a_{\ell_e} = C_{\ell_P} \llbracket -F_{\ell_P}, 0 \rrbracket ; \quad a_{\ell_{ww}} = C_{\ell_W} \llbracket F_{\ell_W}, 0 \rrbracket ; \quad a_{\ell_w}^o = \tilde{\rho}_{\ell_w}^o \tilde{\alpha}_{\ell_w}^o \frac{A \Delta x}{\Delta t}$$

$$a_{\ell_w} = a_{\ell_w}^o + a_{\ell_e} + a_{\ell_{ww}} + (C_{\ell_P} - 1) F_{\ell_P} - (C_{\ell_W} - 1) F_{\ell_W} + S p_{\ell_w} \Delta x \quad (5.27)$$

The source coefficients are defined as

$$b^{U_\ell} = a_{\ell_w}^o U_{\ell_w}^o + S_{C_{\ell_w}} A \Delta x + b_{TVD}^{U_\ell} \quad (5.28)$$

$$b_{TVD}^{U_\ell} = -C_{\ell_P} |F_{\ell_P}| \frac{\Psi(U_{\ell_P})}{2} (U_{\ell_w} - U_{\ell_e}) - C_{\ell_W} |F_{\ell_W}| \frac{\Psi(U_{\ell_W})}{2} (U_{\ell_{ww}} - U_{\ell_w}) \quad (5.29)$$

where the source terms vary depending upon the phase. They are defined below for each phase as

$$S_{P_{G_w}} = -b_i \quad ; \quad S_{P_{L_w}} = -b_{wL} \quad (5.30)$$

$$S_{C_{G_w}} = b_{gG} + b_i U_{lf_w} + b_{dyn_G} \quad (5.31)$$

$$S_{C_{L_w}} = b_{gL} + b_i (U_{G_w} - U_{lf_w}) + b_{dyn_L} + b_{jump}$$

The terms b_i and b_{wL} are the wall and interfacial shear stress contributions, defined as

$$b_i = \frac{1}{2} f_{i_w} \tilde{\rho}_{G_w} |U_{G_w} - U_{lf_w}| S_{i_w} \quad ; \quad b_{wL} = \frac{1}{2} f_{L_w} \rho_L |U_{L_w}| S_{L_w} \quad (5.32)$$

where U_{lf} is the liquid film velocity, which depend on the correlation employed to determine the interface shear stress. S_L and S_i are the liquid wetted perimeter and the interfacial perimeter, respectively. f_L and f_i are the wall and interfacial friction factors.

The interface pressure jump is

$$b_{jump} = \tilde{\alpha}_{L_w} A \sigma (\kappa_p - \kappa_w) \quad (5.33)$$

and the gravitational terms are defined as

$$b_{gG} = -\tilde{\rho}_G \tilde{\alpha}_G A g \quad ; \quad b_{gL} = -\rho_L \tilde{\alpha}_L A g \quad (5.34)$$

Lastly, the dynamic pressure source can be written as

$$b_{dyn_G} = W_{fG} A \left[\alpha_{G_P} \rho_{ref_P} (U_{LP} - U_{i_P})^2 - \alpha_{G_W} \rho_{ref_W} (U_{LW} - U_{i_W})^2 \right] \quad (5.35)$$

$$b_{dyn_L} = W_{fL} A \left[\alpha_{LP} \rho_{ref_P} (U_{LP} - U_{iP})^2 - \alpha_{LW} \rho_{ref_W} (U_{LW} - U_{iW})^2 \right] \quad (5.36)$$

where W_{fk} and U_i are dependent on the dynamic pressure model. The nodal points liquid and interface velocities are averaged from the face values, i.e., $U_{\ell_P} = (U_{\ell_w} + U_{\ell_e})/2$ and $U_{\ell_W} = (U_{\ell_{ww}} + U_{\ell_w})/2$.

5.3 Pressure

From the summation of the gas and liquid continuity equations, an equation for pressure can be derived. To avoid the predominance of the liquid contribution over the gas in the combined equation (and the convergence issues that come associated with it) the equations are normalized by the reference phase densities (Issa & Kempf, 2003; Bonnizi, 2003). The resulting equation is shown below

$$\frac{\partial \alpha_L}{\partial t} + \frac{\partial(\alpha_L U_L)}{\partial x} + \frac{1}{\rho_G^{ref}} \left\{ \frac{\partial \rho_G \alpha_G}{\partial t} + \frac{\partial(\rho_G \alpha_G U_G)}{\partial x} \right\} = 0 \quad (5.37)$$

where ρ_G^{ref} is the reference gas density. The discrete form of Eq. (5.37) is obtained from a similar procedure employed for the gas volume fraction. The resulting equation is shown below

$$\begin{aligned} & (\alpha_{LP} - \alpha_{LP}^o) A \frac{\Delta x}{\Delta t} + [\hat{\alpha}_{Le} U_{Le} A - \hat{\alpha}_{Lw} U_{Lw} A] \\ & + \frac{1}{\rho_g^{ref}} \left[(\alpha_{GP} \rho_{GP} - \alpha_{GP}^o \rho_{GP}^o) A \frac{\Delta x}{\Delta t} \right. \\ & \left. + (\hat{\rho}_{Ge} \hat{\alpha}_{Le} U_{Ge} A - \hat{\rho}_{Gw} \hat{\alpha}_{Lw} U_{Gw} A) \right] = 0 \end{aligned} \quad (5.38)$$

Here $\hat{\rho}$ and $\hat{\alpha}$ are determined with the Upwind approximation, Eqs. (5.4), (5.5), (5.21) and (5.22).

The dependence on the pressure can be incorporated into Eq. (5.38) by introducing the face evaluated phase velocities from the momentum equation, written as

$$U_{\ell_w} = \hat{U}_{\ell_w} - \frac{\tilde{\alpha}_{\ell_w} A}{a_{\ell_w} / \gamma} (P_P - P_W) ; \quad U_{\ell_e} = \hat{U}_{\ell_e} - \frac{\tilde{\alpha}_{\ell_e} A}{a_{\ell_e} / \gamma} (P_E - P_P) \quad (5.39)$$

\hat{U}_ℓ are pseudo velocities, defined as

$$\hat{U}_{\ell_w} = \frac{\sum_{nb} a_{nb\ell_w} U_{\ell_{nb_w}} + b^{U_{\ell_w}} + (1 - \gamma) a_{\ell_w} / \gamma U_{\ell_w}^*}{a_{\ell_w} / \gamma} \quad (5.40)$$

$$\hat{U}_{\ell_e} = \frac{\sum_{nb} a_{nb\ell_e} U_{\ell_{nb_e}} + b^{U_{\ell_e}} + (1 - \gamma) a_{\ell_e} / \gamma U_{\ell_e}^*}{a_{\ell_e} / \gamma} \quad (5.41)$$

where $a_{nb\ell_w}$ are the neighboring coefficients of the phase- ℓ velocity at the w face, while $a_{nb\ell_e}$ corresponds to the neighboring coefficients of the equation discretized at the e face.

The node evaluated gas density has a dependency on the pressure through the ideal gas equation

$$\rho_{G_P} = \frac{P_P}{RT} = \rho_G^{ref} \frac{P_P}{P^{ref}} \quad (5.42)$$

From Eqs. (5.37) and (5.42), the resulting algebraic equation for pressure becomes

$$a_P P_P = a_W P_W + a_E P_E + b^P \quad (5.43)$$

with the following coefficients

$$a_W = \left(\frac{\hat{\rho}_{G_w}}{\rho_G^{ref}} \hat{\alpha}_{G_w} \frac{\tilde{\alpha}_{G_w} A}{a_{G_w} / \gamma} + \hat{\alpha}_{L_w} \frac{\tilde{\alpha}_{L_w} A}{a_{L_w} / \gamma} \right) A \quad (5.44)$$

$$a_E = \left(\frac{\hat{\rho}_{G_e}}{\rho_G^{ref}} \hat{\alpha}_{G_e} \frac{\tilde{\alpha}_{G_e} A}{a_{G_e} / \gamma} + \hat{\alpha}_{L_e} \frac{\alpha_{L_e} A}{a_{L_e} / \gamma} \right) A$$

$$a_P = a_W + a_E + \frac{\alpha_{G_P}}{P^{ref}} A \frac{\Delta x}{\Delta t}$$

and the source term is defined as

$$\begin{aligned} b^P = & \left[\alpha_{L_P}^o - \alpha_{L_P} + \left(\frac{\rho_{G_P}^o}{\rho_G^{ref}} \alpha_{G_P}^o \right) \right] A \frac{\Delta x}{\Delta t} \\ & + \left(\frac{\hat{\rho}_{G_w}}{\rho_G^{ref}} \hat{\alpha}_{G_w} \hat{U}_{G_w} - \frac{\hat{\rho}_{G_e}}{\rho_G^{ref}} \hat{\alpha}_{G_e} \hat{U}_{G_e} \right) A \\ & + (\hat{\alpha}_{L_w} \hat{U}_{L_w} - \hat{\alpha}_{L_e} \hat{U}_{L_e}) A \end{aligned} \quad (5.45)$$

5.4 Boundary conditions

In the entrance boundary of the domain, there are three known quantities: the gas volume fraction and the gas and liquid superficial velocities. Thus, the liquid volume fraction and phase velocities are readily available. It is worth restating here that a uniform spatial mesh was defined according to the method A of Patankar (1980). Thus, the control volume face is placed half distance between nodes ($\Delta x/2$) and the boundary control volumes size are $\Delta x/2$.

The convective fluxes in the faces of the boundary control volume also require special treatment. The r parameters for the gas density and velocities in the TVD flux limiter function needs to be redefined for the boundary. Following the procedure recommended by Fontalvo (2016) and Versteeg & Malalasekera (2007), the corrected parameters are

$$r_{\alpha_{ww}} = \frac{\alpha_{G_{ww}} - \alpha_{G_o}}{\alpha_{G_w} - \alpha_{G_{ww}}} \llbracket \text{sign}(U_{G_{ww}}), 0 \rrbracket + \frac{\alpha_{G_p} - \alpha_{G_w}}{\alpha_{G_w} - \alpha_{G_{ww}}} \llbracket -\text{sign}(U_{G_{ww}}), 0 \rrbracket \quad (5.46)$$

$$r_{U_{\ell w}} = \frac{U_{\ell_{ww}} - U_{\ell_o}}{U_{\ell_w} - U_{\ell_{ww}}} \llbracket \text{sign}(F_{\ell_w}), 0 \rrbracket + \frac{U_{\ell_e} - U_{\ell_w}}{U_{\ell_w} - U_{\ell_{ww}}} \llbracket -\text{sign}(F_{\ell_w}), 0 \rrbracket \quad (5.47)$$

The values α_o and U_{k_o} can be interpreted as extrapolated mirror values upstream from the boundary. They are defined as

$$\alpha_o = 2\alpha_A - \alpha_P \quad (5.48)$$

$$U_{G_o} = 2U_{G_A} - U_{G_{ww}} ; \quad U_{L_o} = 2U_{L_A} - U_{L_{ww}}$$

where α_A , U_{G_A} and U_{L_A} are the prescribed boundary values. Lastly, at the exit, the pressure value is known. Thus, velocities and volume fractions must be calculated. A linear extrapolation from the first internal neighbors is undertaken as an approximation.

$$\frac{U_{N+1} - U_N}{\Delta x/2} = \frac{U_N - U_{N-1}}{\Delta x} \rightarrow U_{N+1} = \frac{3U_N - U_{N-1}}{2} \quad (5.49)$$

$$\frac{\alpha_N - U_{N-1}}{\Delta x} = \frac{\alpha_{N-1} - \alpha_{N-2}}{\Delta x} \rightarrow \alpha_N = 2\alpha_{N-1} - \alpha_{N-2} \quad (5.50)$$

5.5 Mesh and Time step

A mesh discretization spacing must be defined. As it has been previously discussed, a uniform mesh was defined in the present work, so the mesh spacing can be easily determined from the domain length L and the total number of points N as

$$\Delta x = \frac{L}{N - 1} \quad (5.51)$$

Also, for *Regime Capturing* simulations, refined meshes are required to adequately resolve the natural disturbances of the flow. Therefore, a fine mesh ($\Delta x \sim 0.1D$) is recommended, although a test of mesh independence must always be performed.

An adequate timestep must also be selected. The Courant-Friedrichs-Levy condition correlates the timestep with the mesh spacing and the characteristic velocity of the flow, and it can be written in terms of a Courant number

$$Co = \frac{\max|U| \Delta t}{\Delta x} \quad (5.52)$$

where $\max|U|$ is the maximum flow velocity. The Co number limits the number of control volumes that can be crossed at a given timestep. Therefore, for a given mesh size, if the velocity of the flow increases, the timestep will decrease proportionally. For the simulations of this work, a Courant number of $Co = 0.5$ was selected.

5.6 Numerical execution procedure

The resulting numerical system derived in the previous subsections consist of a set of four discretized differential equations in a control volume. The values in the principal points (P in the scalar control volume and w in the vector control volume) are only a function of its neighbors, which results in tri-diagonal solution matrices. These matrices can be solved using the TDMA algorithm (Patankar, 1980). Because these equations are non-linear and coupled, they

require an iterative solution procedure. A modified PRIME algorithm as proposed by Ortega (2004), based on the original PRIME algorithm (Maliska, 1981), is employed in this work. A description of the solution procedure is outlined below

- i) Set the initial conditions of the flow (i.e., velocity fields, volume fractions and pressure for $t = 0$).
- ii) Use solution from previous time instant as an initial guess for the current timestep.
- iii) Solve Eq. (5.26) for the phase velocity fields using the estimated pressure field.
- iv) Solve Eq. (5.43) for the pressure field.
- v) Solve Eq. (5.39) to explicitly correct the velocity field based on the new pressure field.
- vi) Solve Eq. (5.11) for the gas volume fraction field.
- vii) Check residuals ($res_{tot} < tol$)
 - (a) If the condition is satisfied, go to step (viii).
 - (b) If the condition is *not* satisfied, go to step (iii).
- viii) Check simulation time ($t < t_{final}$)
 - (a) If the condition is satisfied, end simulation.
 - (b) If the condition is *not* satisfied, update the timestep and go to step (ii).

In the procedure described above, the convergence of the iterative process is checked through the residuals of the obtained solution from the TDMA algorithm. We define

$$res_{max} = \max(|a_P \phi_P - a_E \phi_E - a_W \phi_W - b|) \quad (5.53)$$

which represents the maximum residual in the entire domain for a generic flow quantity ϕ . The tolerance stipulated for the simulations performed in this work is of 10^{-7} . If they are not met within a maximum number of iterations (i.e., 20 iterations), the solution has not converged.

6 THE STABILITY-HYPERBOLICITY PROBLEM OF THE 1D TWO-FLUID MODEL

As discussed in previous sections, the standard Two-Fluid Model may be conditionally ill-posed in horizontal geometries, and unconditionally ill-posed in vertical geometries.

The well-posedness of a system is achieved when the PDEs satisfy the Hadamard conditions (Hadamard, 1902):

- A solution exists
- The solution is unique
- The solution continually depends on boundary and initial conditions

If these conditions are not met, the problem is ill-posed. The first and second conditions generally do not generate great difficulties, i.e., the existence of a unique solution (Montini, 2011). The failure to meet the third criterium may manifest as an inability to attain a mesh convergent solution, as any small disturbance superposed with the initial condition may propagate along the physical domain and generate an entirely different solution.

Through the optics of an analysis of characteristics, one must determine the characteristic roots of the system of conservation equations of mass and momentum to be able to define if it is well-posed or ill-posed. To determine the characteristic roots, it is convenient to write the conservation equations in a non-conservative matrix form as

$$\mathbf{A}(\boldsymbol{\varphi}) \frac{\partial}{\partial t} \boldsymbol{\varphi} + \mathbf{B}(\boldsymbol{\varphi}) \frac{\partial}{\partial x} \boldsymbol{\varphi} + \mathbf{C}(\boldsymbol{\varphi}) = 0 \quad (6.1)$$

where $\boldsymbol{\varphi}$ is the vector of unknown independent variables, \mathbf{A} and \mathbf{B} are square n -dimension coefficient matrices, n being the number of independent variables, and \mathbf{C} is the column vector containing the algebraic terms. The system defined in Eq. (6.1) is an initial value problem with constraints in space and time of $0 \leq x \leq L$ and $t \geq 0$, respectively, where L is the domain length.

The initial condition for the system is of the form $\boldsymbol{\varphi}(0, x) = \boldsymbol{\varphi}_0(x)$. The characteristics of the system are then defined as the eigenvalues λ_n that satisfy the characteristic equation

$$\det(\mathbf{B} - \lambda_n \mathbf{A}) = 0 \quad (6.2)$$

Equation (6.2) has n roots associated with the λ_n characteristics. The following criteria can be employed to assess the hyperbolicity of the system

- If all n roots are real and distinct, the system is hyperbolic
- If there are equal roots, the system is parabolic
- If there are complex roots, the system is elliptic

If all the characteristics are real and distinct (hyperbolic system), the problem is well-posed and the information propagates in the real domain. The number of quantities to be prescribed for the initial value problem equals the number of characteristics obtained. Complex characteristics (elliptic system) imply the propagation of information from the complex plan to the real plan, and the problem of initial value is ill-posed. It would be possible to obtain a solution with the prescription of boundary conditions in all space and time (boundary value problem), which would imply the need (simply impossible) to provide information of future times (Prosperetti & Tryggvason, 2007).

For the classical Two-Fluid model, without dynamic pressure and interface pressure jump, and with the momentum flux parameters equal to 1, (Issa & Kempf, 2003; Carneiro, 2006 and Montini, 2011), the criterion to determine if the system is well- or ill-posed is given by

$$(U_G - U_L)^2 \leq \left(\frac{\alpha_L}{\rho_L} + \frac{\alpha_G}{\rho_G} \right) (\rho_L - \rho_G) \frac{\partial h_L}{\partial \alpha_G} g \cos \beta \quad (6.3)$$

Therefore, for vertical geometries, the standard model is well posed only for the condition $U_L = U_G$.

Several authors have observed that the issue of ill-posedness is associated with the unbounded growth of small wavelength perturbations. Thus, the problem can be explored as an issue of stability. This is discussed in the next section.

6.1 Linear Stability Analysis

A simple definition of stability is laid out in Drazin (2002). Qualitatively, the stability of a physical state is a measure of the effect that a small variation in that state at present time has in its conditions at a future time. If the variation in the future is infinitesimally small, the physical state is stable. However, if the variation

in the present state generates a finitely different state in a finite future time, then the state is unstable.

In a numerical system, the onset of instabilities may occur from two sources: an unsteadiness generated by an initial condition that differs slightly from the equilibrium of a quantity in that system, or by the growth of machine round-off and truncation errors. Those mechanisms are inherent of any numerical procedure, and their magnitude will be dependent on the machine precision (e.g., single or double precision), timestep and mesh size. Although they are of an artificial nature, there is a direct analogy between these machine precision errors, that manifest as infinitesimally small disturbances, and physical short-wavelength variations that are always present in any flow (Carneiro, 2006).

Through the optics of Linear Stability Theory (LST), one can define well-posedness in terms of the behavior presented by perturbations in a given system. In a well-posed system, the growth of all resolvable wavelengths must be bounded. If the perturbation decays, the system is well-posed stable (Figure 6.1a); if it grows and the growth rate is bounded, the system is well-posed unstable (Figure 6.1d). The zero-stability condition occurs when the system neither damps nor amplifies the disturbance (Figure 6.1b). If the system is ill-posed, the growth rate of short wavelengths is unbounded, and the disturbance grows unphysically (Figure 6.1c).

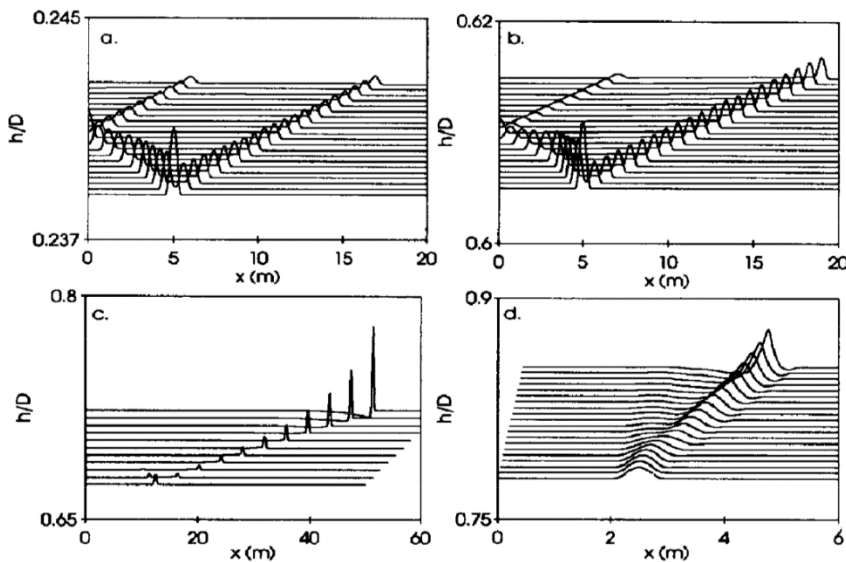


Figure 6.1- Propagation of a disturbance in horizontal flow (Montini, 2011).

The problem of ill-posedness is, however, unrelated to the hydrodynamic stability of the physical flow, but an aspect of the mathematical and numerical models.

The mesh plays an important role in the amplification of numerical

disturbances. The smallest wavelength that a numerical system can resolve is of $2\Delta x$, where Δx is the mesh spacing. This threshold comes from the fact that at least two discrete points are required to resolve one period of oscillation of a wave. Thus, the mesh imposes a cut-off wavelength and essentially cannot see smaller disturbances. The use of increasingly more refined meshes allows for shorter wavelength disturbances to appear, significantly altering the numerical solution. The result is an inability to converge with mesh refinement, a clear characteristic of ill-posedness. On the other hand, a numerical discretization with coarse meshes tends to impose acute numerical diffusion into the system, and the formation of interfacial waves may be excessively damped or may not even occur. With this in mind, some authors have employed a more pragmatic solution to overcome the issue of ill-posedness in vertical flows, which is to employ intermediary meshes ($D \geq \Delta x \geq 0.1D$) with the *Regime Capturing* approach to predict the onset of slug flow (see Issa & Galleni, 2015). In reality, if the numerical model is consistent, its solution should approach that of the system of partial differential equations, for infinitely small meshes and time-steps. Thus, to overcome the issue, physical mechanisms must be reintroduced into the governing equations through closure models. The effect of closure relations on the hyperbolicity of the system can be tracked through linear stability theory.

A linear stability analysis evaluates the stability of a system by imposing perturbations to all of its flow quantities and quantifying the growth rate of these disturbances. Two approaches are commonly employed in the literature: a differential stability analysis, that only addresses the stability of the mathematical system of equation, and a discrete stability analysis, that considers the contribution of numerical effects into the solution. Considering the differential approach, the Two-Fluid Model equation system can be either inviscid (the shear stress terms are zero) or viscous (the wall and interfacial shear stresses must be modeled for closure).

6.2 Differential Stability Analysis

The destabilization of two-phase flows that results in the transition from different flow regimes is usually considered to be generated by the Kelvin-Helmholtz instability mechanism. The critical conditions that trigger ill-posedness are known to coincide with the Inviscid Kelvin-Helmholtz stability criteria (Liao *et al.*, 2008).

A stability analysis applied to the mathematical set of conservation equations allows for the identification of well/ill-posedness regions and generates a

dispersion relation, that correlates the growth rate of instabilities with their respective wavelengths, such that one has information on which waves grow, which waves decay, and at what rate. This further enriches the assessment of closure relation effects on the model, as the exact mathematical mechanism through which they act on wave formation becomes evident.

For the derivation of the differential approach, an appropriate starting point would be the compact matrix system of the conservation equations. Although we have four unknowns (pressure, gas volumetric fraction, gas and liquid velocities), and four equations, it is possible to combine the momentum equations to eliminate pressure in order to render a simpler system of equations, in this case, the unknown vector is defined as

$$\boldsymbol{\varphi} = (\alpha_L, U_G, U_L)^T, \quad (6.4)$$

Thus, the matrix set of conservation equations, must be formed by three equations: mass conservation of gas and liquid and combined momentum equation (gas momentum equation minus liquid momentum equation). Thus, it is convenient to define a combined dynamic pressure term of the form

$$p = \Delta P_{dynL} - \Delta P_{dynG} \quad (6.5)$$

To write the equation in a non-conservative form, one needs to determine the spatial variation of the dynamic pressure and momentum flux parameter, which are

$$\frac{\partial p}{\partial x} = \frac{\partial p}{\partial \alpha_L} \frac{\partial \alpha_L}{\partial x} + \frac{\partial p}{\partial U_L} \frac{\partial U_L}{\partial x} + \frac{\partial p}{\partial U_G} \frac{\partial U_G}{\partial x} \quad (6.6)$$

$$\frac{\partial C_\ell}{\partial x} = \frac{\partial C_\ell}{\partial \alpha_L} \frac{\partial \alpha_L}{\partial x} + \frac{\partial C_\ell}{\partial U_L} \frac{\partial U_L}{\partial x} + \frac{\partial C_\ell}{\partial U_G} \frac{\partial U_G}{\partial x} \quad (6.7)$$

The governing matrix system, rewritten here for clarity, is

$$\mathbf{A} \frac{\partial}{\partial t} \boldsymbol{\varphi} + \mathbf{B} \frac{\partial}{\partial x} \boldsymbol{\varphi} + \mathbf{C} = 0 \quad (6.8)$$

where the coefficient matrices \mathbf{A} , \mathbf{B} and \mathbf{C} are

$$\mathbf{A} = \begin{pmatrix} -1 & 0 & 0 \\ -1 & 0 & 0 \\ \frac{\rho_L U_L}{\alpha_L} + \frac{\rho_G U_G}{\alpha_G} & -\rho_G & \rho_L \end{pmatrix} \quad (6.9)$$

$$\mathbf{B} = \begin{pmatrix} -U_G & \alpha_G & 0 \\ -U_L & 0 & -\alpha_L \\ \left(C_L \frac{\rho_L}{\alpha_L} U_L^2 + C_G \frac{\rho_G}{\alpha_G} U_G^2 \right) + & -2C_G \rho_G U_G + \frac{\partial p}{\partial U_G} & 2C_L \rho_L U_L + \frac{\partial p}{\partial U_L} \\ +\rho_L U_L^2 \frac{\partial C_L}{\partial \alpha_L} - \rho_G U_G^2 \frac{\partial C_G}{\partial \alpha_L} + & +\rho_L U_L^2 \frac{\partial C_L}{\partial U_G} - \rho_G U_G^2 \frac{\partial C_G}{\partial U_G} & +\rho_L U_L^2 \frac{\partial C_L}{\partial U_L} - \rho_G U_G^2 \frac{\partial C_G}{\partial U_L} \\ \frac{\Delta P_L}{\alpha_L} + \frac{\Delta P_G}{\alpha_G} + \frac{\partial p}{\partial \alpha_L} - \sigma \frac{\partial \kappa_2}{\partial \alpha_L} & & \end{pmatrix} \quad (6.10)$$

$$\mathbf{C} = \begin{pmatrix} 0 \\ 0 \\ \mathcal{F} - \frac{\sigma \partial \kappa_1}{\partial x} \end{pmatrix} \quad (6.11)$$

where \mathcal{F} denotes the force term, given by

$$\mathcal{F} = (\rho_L - \rho_G) g + \frac{\tau_L S_L}{\alpha_L A_L} - \frac{\tau_i S_i}{A} \left(\frac{1}{\alpha_L} - \frac{1}{\alpha_G} \right) \quad (6.12)$$

The solution vector can be split into two components, a base value $\bar{\boldsymbol{\varphi}}$ and a perturbed contribution $\hat{\boldsymbol{\varphi}}$, ($\boldsymbol{\varphi} = \bar{\boldsymbol{\varphi}} + \hat{\boldsymbol{\varphi}}$) such that the system can be linearized with respect to $\hat{\boldsymbol{\varphi}}$. The differential formulation takes a disturbed quantity of the form

$$\hat{\boldsymbol{\varphi}} = \boldsymbol{\varepsilon} e^{i(\omega t - kx)} ; \quad \boldsymbol{\varepsilon} = (\varepsilon_\alpha, \varepsilon_{u_G}, \varepsilon_{u_L})^T \quad (6.13)$$

where $\boldsymbol{\varepsilon}$ is the amplitude, ω represents the angular frequency, k represents the wavenumber and $i = \sqrt{-1}$ is the unit imaginary number. The decomposed solution vector is then applied to the matrix system, Eq. (6.8), resulting in

$$\begin{aligned} \bar{\mathbf{A}} \frac{\partial \boldsymbol{\varphi}}{\partial t} + \bar{\mathbf{A}} \frac{\partial \hat{\boldsymbol{\varphi}}}{\partial t} + \hat{\mathbf{A}} \frac{\partial \boldsymbol{\varphi}}{\partial t} + \hat{\mathbf{A}} \frac{\partial \hat{\boldsymbol{\varphi}}}{\partial t} + \bar{\mathbf{B}} \frac{\partial \boldsymbol{\varphi}}{\partial x} + \bar{\mathbf{B}} \frac{\partial \hat{\boldsymbol{\varphi}}}{\partial x} + \hat{\mathbf{B}} \frac{\partial \boldsymbol{\varphi}}{\partial x} + \hat{\mathbf{B}} \frac{\partial \hat{\boldsymbol{\varphi}}}{\partial x} \\ = \bar{\mathbf{C}} + \hat{\mathbf{C}} \end{aligned} \quad (6.14)$$

Eliminating the mean flow and non-linearities from the system yields

$$\bar{\mathbf{A}} \frac{\partial \hat{\boldsymbol{\varphi}}}{\partial t} + \bar{\mathbf{B}} \frac{\partial \hat{\boldsymbol{\varphi}}}{\partial x} = \hat{\mathbf{C}} \quad (6.15)$$

where the temporal and spatial derivatives are

$$\frac{\partial \hat{\varphi}}{\partial t} = i \omega e^{i(\omega t - kx)} \boldsymbol{\varepsilon} \quad ; \quad \frac{\partial \hat{\varphi}}{\partial x} = -i k e^{i(\omega t - kx)} \boldsymbol{\varepsilon} \quad (6.16)$$

The force contribution is rewritten as

$$\mathcal{F} = \bar{\mathcal{F}} + \hat{\mathcal{F}} \quad (6.17)$$

where the perturbed contribution is

$$\hat{\mathcal{F}} = \frac{\partial \mathcal{F}}{\partial \alpha_L} \hat{\alpha}_L + \frac{\partial \mathcal{F}}{\partial U_G} \hat{U}_G + \frac{\partial \mathcal{F}}{\partial U_L} \hat{U}_L \quad (6.18)$$

The linearized perturbation of the curvature term is

$$\hat{\kappa} = \frac{\partial \hat{\kappa}_1}{\partial x} + \frac{\partial \kappa_2}{\partial \alpha_L} \hat{\alpha}_L \quad ; \quad \frac{\partial \hat{\kappa}_1}{\partial x} \cong \frac{D}{4\sqrt{\alpha_G}} \left(\frac{\partial^3 \hat{\alpha}_L}{\partial x^3} \right) \quad ; \quad \frac{\partial \kappa_2}{\partial \alpha_L} = \frac{1}{D \alpha_G^{3/2}} \quad (6.19)$$

With the definition of curvature and force terms, we rewrite the independent variable term \mathcal{C} as

$$\hat{\mathcal{C}} = \hat{\mathbf{D}} \hat{\varphi} \quad (6.20)$$

where

$$\hat{\mathbf{D}} = - \begin{pmatrix} 0 & 0 & 0 \\ \frac{\partial \mathcal{F}}{\partial \alpha_L} & \frac{\partial \mathcal{F}}{\partial U_G} & \frac{\partial \mathcal{F}}{\partial U_L} \end{pmatrix} \quad (6.21)$$

such that the system is rewritten as

$$\left(\bar{\mathbf{A}} \frac{\partial}{\partial t} + \bar{\mathbf{B}} \frac{\partial}{\partial x} - \hat{\mathbf{D}} \right) \hat{\varphi} = 0 \quad (6.22)$$

Notice that for $\hat{\mathbf{D}} = 0$ the inviscid approach of the differential stability analysis is recovered. Lastly, we can define a coefficient matrix \mathbf{M} such that

$$\left[\bar{\mathbf{A}} \frac{\partial}{\partial t} + \bar{\mathbf{B}} \frac{\partial}{\partial x} - \hat{\mathbf{D}} \right] (e^{i(\omega t - kx)} \boldsymbol{\varepsilon}) = 0 \rightarrow \mathbf{M} \boldsymbol{\varepsilon} = 0 \quad (6.23)$$

where

$$\mathbf{M} = \quad (6.24)$$

$$\begin{pmatrix} \omega - k u_G & \alpha_G k & 0 \\ \omega - k u_L & 0 & -\alpha_L k \\ -\omega \left(\frac{\rho_L U_L}{\alpha_L} + \frac{\rho_G U_G}{\alpha_G} \right) & \left(\begin{array}{c} \rho_G \omega - 2 C_G \rho_G u_G k \\ +k \left(\rho_L U_L^2 \frac{\partial C_L}{\partial U_G} - \rho_G U_G^2 \frac{\partial C_G}{\partial U_G} \right) \\ +k \left(\frac{\Delta P_L}{\alpha_L} + \frac{\Delta P_G}{\alpha_G} \right) + k \frac{\partial \wp}{\partial \alpha_L} \\ -k \frac{\sigma}{D \alpha_G^{3/2}} + k^3 \frac{\sigma D}{4\sqrt{\alpha_G}} + i \frac{\partial \mathcal{F}}{\partial \alpha_L} \end{array} \right) & \left(\begin{array}{c} -\rho_L \omega + 2 C_L \rho_L u_L k \\ +k \left(\rho_L U_L^2 \frac{\partial C_L}{\partial U_L} - \rho_G U_G^2 \frac{\partial C_G}{\partial U_L} \right) \\ +k \frac{\partial \wp}{\partial u_L} + i \frac{\partial \mathcal{F}}{\partial u_L} \end{array} \right) \end{pmatrix}$$

For a nontrivial solution to exist, the determinant of \mathbf{M} must be null. The dispersion relation $\omega(k)$ is defined as a second order polynomial

$$A \omega^2 + B \omega + C = 0 \rightarrow \omega = \frac{-B \pm \sqrt{B^2 - 4 A C}}{2 A} \quad (6.25)$$

where the coefficients are defined as

$$A = \left(\frac{\rho_G}{\alpha_G} + \frac{\rho_L}{\alpha_L} \right) ; B = -(b_1 k + b_2 i) ; C = c_1 k^2 - c_2 k i \quad (6.26)$$

$$b_1 = 2 C_G \frac{\rho_G}{\alpha_G} U_G + 2 C_L \frac{\rho_L}{\alpha_L} U_L - \left(\frac{1}{\alpha_G} \frac{\partial \wp}{\partial U_G} - \frac{1}{\alpha_L} \frac{\partial \wp}{\partial U} \right) \quad (6.27)$$

$$+ \rho_G U_G^2 \left(\frac{1}{\alpha_G} \frac{\partial C_G}{\partial U_G} - \frac{1}{\alpha_L} \frac{\partial C_G}{\partial U_L} \right) - \rho_L U_L^2 \left(\frac{1}{\alpha_G} \frac{\partial C_L}{\partial U_G} - \frac{1}{\alpha_L} \frac{\partial C_L}{\partial U_L} \right)$$

$$c_1 = \left(C_L \frac{\rho_L}{\alpha_L} U_L^2 + C_G \frac{\rho_G}{\alpha_G} U_G^2 \right) + \frac{\sigma}{D \alpha_L^{3/2}} - k^2 \frac{\sigma D}{4 \alpha_L^{1/2}} \quad (6.28)$$

$$- \left(\frac{\Delta P_L}{\alpha_L} + \frac{\Delta P_G}{\alpha_G} \right) - \left(\frac{\partial \wp}{\partial \alpha_L} + \frac{U_G}{\alpha_G} \frac{\partial \wp}{\partial U_G} - \frac{U_L}{\alpha_L} \frac{\partial \wp}{\partial U_L} \right)$$

$$+ \rho_L U_L^2 \left(\frac{\partial C_L}{\partial \alpha_L} + \frac{U_G}{\alpha_G} \frac{\partial C_L}{\partial U_G} - \frac{U_L}{\alpha_L} \frac{\partial C_L}{\partial U_L} \right) + \rho_G U_G^2 \left(\frac{\partial C_G}{\partial \alpha_L} + \frac{U_G}{\alpha_G} \frac{\partial C_G}{\partial U_G} - \frac{U_L}{\alpha_L} \frac{\partial C_G}{\partial U_L} \right)$$

$$b_2 = - \left(\frac{1}{\alpha_G} \frac{\partial \mathcal{F}}{\partial U_G} - \frac{1}{\alpha_L} \frac{\partial \mathcal{F}}{\partial U_L} \right) ; c_2 = \left(\frac{\partial \mathcal{F}}{\partial \alpha_L} + \frac{U_G}{\alpha_G} \frac{\partial \mathcal{F}}{\partial U_G} - \frac{U_L}{\alpha_L} \frac{\partial \mathcal{F}}{\partial U_L} \right) \quad (6.29)$$

The negative complex part of $\omega = \omega_R \pm i \omega_i$ is the temporal growth rate of perturbations, and the real part is the frequency. Positive values of $-\omega_i$ indicate that the perturbations are amplified, and therefore the system is unstable (see Figure

6.2). Additionally, if the amplification rate grows unboundedly for short wavelengths, the system is ill-posed. Negative $-\omega_i$ indicate that the perturbations are damped, and therefore the system is stable.

The zero-stability condition occurs when the growth-rate is exactly zero for all wavelengths. This constitutes the Inviscid Kelvin-Helmholtz (IKH) and Viscous Kelvin-Helmholtz (VKH) stability limits. Plotting the zero stability limits for different pairs of superficial velocities, one can obtain a stability map with well-defined regions of well/ill-posedness.

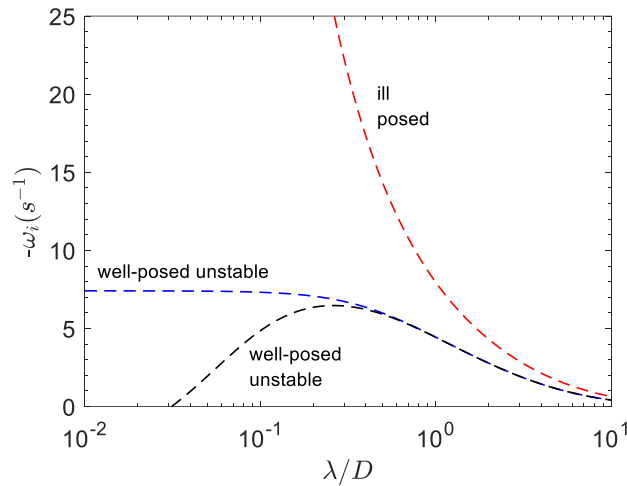


Figure 6.2 - Dispersion relation for different stability conditions.

6.3 Discrete Stability Analysis

As discussed, the discretization of the system of equations has an inherent effect on the solution. The spatial differencing scheme imposes an additional stabilizing effect known as numerical viscosity or numerical diffusion. For example, the First Order Upwind scheme is known to add significant artificial viscosity to the system.

To analyze the stability of the discrete system of equations, a von Neumann analysis is performed (von Neumann & Richmeyer, 1949). The system of partial differential equations is discretized using the Finite Volume Method with a second order TVD van Leer spatial scheme in a staggered grid, i.e., the velocity is stored at the faces of the control volume, and the other fields are stored at the central node. Figure 5.1 illustrates the layout of the mesh. Similar to the differential form, the discrete formulation takes a perturbation defined as

$$\hat{\varphi}_p = \varepsilon E^n e^{ikx} \quad (6.30)$$

where E^n is an amplitude factor at time t^n . We illustrate the procedure by considering the continuity equation of phase ℓ . The equation is discretized in relation to a principal node P , where the control volume size is Δx and the timestep is Δt . The discretized equation for time t^{n+1} is defined in Eq. (6.31) (the superscript $n + 1$ are dropped for clarity)

$$\frac{\Delta x}{\Delta t} (\alpha_{\ell P} - \alpha_{\ell P}^n) + (U_{\ell e} \alpha_{\ell e} - U_{\ell w} \alpha_{\ell w}) = 0 \quad (6.31)$$

The approximation of the east and west face values of the volume fractions are defined in a general form

$$\alpha_{\ell e} = \alpha_{\ell P} - 0.5 \psi(r_{\alpha_{\ell e}}) (\alpha_{\ell P} - \alpha_{\ell E}) \quad ; \quad r_{\alpha_{\ell e}} = \frac{(\alpha_{\ell P} - \alpha_{\ell W})}{(\alpha_{\ell E} - \alpha_{\ell P})} \quad (6.32)$$

$$\alpha_{\ell w} = \alpha_{\ell W} - 0.5 \psi(r_{\alpha_{\ell w}}) (\alpha_{\ell W} - \alpha_{\ell P}) \quad ; \quad r_{\alpha_{\ell w}} = \frac{(\alpha_{\ell W} - \alpha_{\ell WW})}{(\alpha_{\ell P} - \alpha_{\ell W})} \quad (6.33)$$

where $\psi(r)$ is the flux limiter function, which depends on the spatial scheme. For the First Order Upwind scheme $\psi(r) = 1$, for the TVD van Leer scheme (Versteeg and Malalasekera, 2007)

$$\psi(r) = \frac{(r + |r|)}{(1 + r)} \quad (6.34)$$

The perturbations in the adjacent control volumes are

$$\hat{\phi}_E = \hat{\phi}_P e^{i\phi} \quad ; \quad \hat{\phi}_W = \hat{\phi}_P e^{-i\phi} \quad (6.35)$$

where $\phi = k\Delta x$ is the phase angle. Thus, the discrete linearized continuity equation for phase ℓ is

$$\begin{aligned} \varepsilon_{\alpha_{\ell}} \left\{ \frac{\Delta x}{\Delta t} (1 - G^{-1}) \right. \\ \left. + u_{\ell} \left[(1 - e^{-i\phi}) + \frac{1}{2} \psi(\hat{r}_{\alpha_{\ell}}) [(e^{i\phi} - 1) + (e^{-i\phi} - 1)] \right] \right\} \frac{\partial \alpha_{\ell}}{\partial \alpha_L} \\ + \varepsilon_{u_{\ell}} \alpha_{\ell} e^{i\phi/2} (1 - e^{-i\phi}) = 0 \end{aligned} \quad (6.36)$$

where

$$G = \frac{E^{n+1}}{E^n} \quad (6.37)$$

is defined as the amplification factor. For the momentum equation, the same procedure is applied. Here, we consider the face perturbed quantities as $\hat{\varphi}_e = \hat{\varphi}_p e^{i\phi/2}$, $\hat{\varphi}_w = \hat{\varphi}_e e^{-i\phi}$ and $\hat{\varphi}_{ww} = \hat{\varphi}_w e^{-i\phi}$. The discretized perturbed momentum flux parameter is defined as

$$\hat{C}_{\ell p} = \frac{\partial C_{\ell}}{\partial \alpha_L} \hat{\alpha}_{Lp} + \frac{\partial C_{\ell}}{\partial U_G} \hat{U}_{Gp} + \frac{\partial C_{\ell}}{\partial U_L} \hat{U}_{Lp} \quad (6.38)$$

The gas momentum equation is subtracted from the liquid, and the curvature terms are substituted by Eqs. (3.40) and (3.41). The discrete linearized formulation of the resulting equation is then written as

$$\begin{aligned} & \varepsilon_{\alpha_L} \left\{ \left(\frac{\rho_L}{\alpha_L} U_L + \frac{\rho_G}{\alpha_G} U_G \right) (1 - G^{-1}) \right. \\ & \quad + \Lambda \left[\left(C_L \rho_L U_L^2 \left(\frac{1}{\alpha_L} + \frac{1}{C_L} \frac{\partial C_L}{\partial \alpha_L} \right) + C_G \rho_G U_G^2 \left(\frac{1}{\alpha_G} + \frac{1}{C_G} \frac{\partial C_G}{\partial \alpha_L} \right) \right) \right. \\ & \quad \left. - \sigma \left[\frac{1}{D \alpha_G^{1.5}} + \frac{D}{4\sqrt{\alpha_G}} e^{i\phi} \left(\frac{\Delta \phi}{\Delta x} \right)^2 \right] + \left(\frac{\Delta P_{dynL}}{\alpha_L} + \frac{\Delta P_{dynG}}{\alpha_G} \right) + \frac{\partial \wp}{\partial \alpha_L} \right] \\ & \quad \left. + \frac{\partial \mathcal{F}}{\partial \alpha_L} \Delta t \right\} \\ & + \varepsilon_{U_G} \left\{ -\rho_G (1 - G^{-1}) \right. \\ & \quad \left. - C_G \rho_G CFL_G \left(\Delta \Psi + e^{\frac{i\phi}{2}} \Delta \phi \left(1 + U_G \frac{1}{C_G} \frac{\partial C_G}{\partial U_G} \right) \right) \right. \\ & \quad \left. + \Lambda \rho_L U_L^2 \frac{\partial C_L}{\partial U_G} + \frac{\partial \wp}{\partial U_G} \Lambda + \frac{\partial \mathcal{F}}{\partial U_G} \Delta t \right\} \\ & + \varepsilon_{U_L} \left\{ \rho_L (1 - G^{-1}) + C_L \rho_L CFL_L \left(\Delta \Psi + e^{\frac{i\phi}{2}} \Delta \phi \left(1 + U_L \frac{1}{C_L} \frac{\partial C_L}{\partial U_L} \right) \right) - \Lambda \rho_G U_G^2 \frac{\partial C_G}{\partial U_L} \right. \\ & \quad \left. + \frac{\partial \wp}{\partial U_L} \Lambda + \frac{\partial \mathcal{F}}{\partial U_L} \Delta t \right\} = 0 \end{aligned} \quad (6.39)$$

where the auxiliary terms are

$$CFL_{\ell} = \frac{U_{\ell} \Delta t}{\Delta x} \quad (6.40)$$

$$\Delta \Psi = \Delta \phi \left(1 + \frac{\psi_{\phi}(\hat{r})}{2} \Delta \phi e^{i\phi} \right) \quad (6.41)$$

$$\Delta \phi = (1 - e^{-i\phi}) \quad (6.42)$$

$$\Lambda = e^{\frac{i\phi}{2}} \frac{\Delta t}{\Delta x} \Delta \phi \quad (6.43)$$

A matrix \mathbf{M} is defined such that $\mathbf{M} \boldsymbol{\varepsilon} = 0$, where

$$\mathbf{M} = \left(\begin{array}{c} (G^{-1} - 1) - CFL_G \Delta \Psi \\ (G^{-1} - 1) - CFL_L \Delta \Psi \\ -(G^{-1} - 1) \left(\frac{\rho_L}{\alpha_L} U_L + \frac{\rho_G}{\alpha_G} U_G \right) \\ + \Lambda \left(\begin{array}{c} C_L \rho_L U_L^2 \left(\frac{1}{\alpha_L} + \frac{1}{C_L} \frac{\partial C_L}{\partial \alpha_L} \right) \\ + C_G \rho_G U_G^2 \left(\frac{1}{\alpha_G} + \frac{1}{C_G} \frac{\partial C_G}{\partial \alpha_L} \right) \end{array} \right) + \\ \Lambda \left[\frac{\Delta P_{dyn_L}}{\alpha_L} + \frac{\Delta P_{dyn_G}}{\alpha_G} + \frac{\partial \wp}{\partial \alpha_L} \right] + \frac{\partial \mathcal{F}}{\partial \alpha_L} \Delta t \\ - \Lambda \sigma \left[\frac{1}{D \alpha_G^{1.5}} + \frac{D}{4\sqrt{\alpha_G}} e^{i\phi} \left(\frac{\Delta \phi}{\Delta x} \right)^2 \right] \end{array} \right) \left(\begin{array}{c} \alpha_G \Lambda \\ 0 \\ -\rho_G C_G CFL_G \left(\begin{array}{c} \rho_G (G^{-1} - 1) \\ \Delta \Psi + \\ e^{\frac{i\phi}{2}} \Delta \phi \left(1 + U_G \frac{1}{C_G} \frac{\partial C_G}{\partial U_G} \right) \end{array} \right) \\ + \Lambda \rho_L U_L^2 \frac{\partial C_L}{\partial U_G} + \Lambda \frac{\partial \wp}{\partial U_G} + \frac{\partial \mathcal{F}}{\partial U_G} \Delta t \end{array} \right) \left(\begin{array}{c} 0 \\ -\alpha_L \Lambda \\ -\rho_L (G^{-1} - 1) \\ \Delta \Psi + \\ + \rho_L C_L CFL_L \left(\begin{array}{c} e^{\frac{i\phi}{2}} \Delta \phi \left(1 + U_L \frac{1}{C_L} \frac{\partial C_L}{\partial U_L} \right) \end{array} \right) \\ - \Lambda \rho_G U_G^2 \frac{\partial C_G}{\partial U_L} + \Lambda \frac{\partial \wp}{\partial U_L} + \frac{\partial \mathcal{F}}{\partial U_L} \Delta t \end{array} \right) \quad (6.44)$$

Lastly, the characteristic equation is solved for the amplification factor G as defined below

$$A G^2 + B G + C = 0 \rightarrow G = \frac{-B \pm \sqrt{B^2 - 4 A C}}{2 A} \quad (6.45)$$

The coefficients are

$$A = \left(\frac{\rho_G}{\alpha_G} + \frac{\rho_L}{\alpha_L} \right) ; \quad B = -(b_1 + b_2) ; \quad C = c_1 + c_2 \quad (6.46)$$

$$\begin{aligned} b_1 = & \frac{\rho_G}{\alpha_G} \left[2 + CFL_G \Delta \Psi (C_G + 1) + \left(c_G - 1 + U_G \left(\frac{\partial C_G}{\partial U_G} - \frac{\alpha_G}{\alpha_L} \frac{\partial C_G}{\partial U_L} \right) \right) CFL_G \left(e^{\frac{i\phi}{2}} \Delta \phi \right) \right] \\ & + \frac{\rho_L}{\alpha_L} \left[2 + CFL_L \Delta \Psi (C_L + 1) + \left(c_L - 1 + U_L \left(\frac{\partial C_L}{\partial U_L} + \frac{\alpha_L}{\alpha_G} \frac{\partial C_L}{\partial U_G} \right) \right) CFL_L e^{\frac{i\phi}{2}} \Delta \phi \right] \\ & - \Lambda \left[\left(\frac{1}{\alpha_G} \frac{\partial \wp}{\partial U_G} - \frac{1}{\alpha_L} \frac{\partial \wp}{\partial U_L} \right) \right] \end{aligned} \quad (6.47)$$

$$\begin{aligned} c_1 = & \frac{\rho_G}{\alpha_G} \left[(1 + CFL_G \Delta \Psi) [1 + C_G CFL_G \Delta \Psi] \right. \\ & \left. + \frac{\rho_L}{\alpha_L} [(1 + CFL_L \Delta \Psi) [1 + C_L CFL_L \Delta \Psi]] \right. \\ & \left. + \frac{\rho_G}{\alpha_G} \left[CFL_G \left(e^{\frac{i\phi}{2}} \Delta \phi \right) \left(C_G \left(1 + U_G \frac{1}{C_G} \frac{\partial C_G}{\partial U_G} \right) - 1 - U_G \frac{\alpha_G}{\alpha_L} \frac{\partial C_G}{\partial U_L} (1 + CFL_L \Delta \Psi) \right) \right] \right. \\ & \left. + \frac{\rho_L}{\alpha_G} \left[CFL_L \left(e^{\frac{i\phi}{2}} \Delta \phi \right) \left(C_L \left(1 + U_L \frac{1}{C_L} \frac{\partial C_L}{\partial U_L} \right) - 1 + U_L \frac{\alpha_L}{\alpha_G} \frac{\partial C_L}{\partial U_G} (1 + CFL_G \Delta \Psi) \right) \right] \right. \\ & \left. + \frac{\rho_G}{\alpha_G} C_G CFL_G^2 e^{\frac{i\phi}{2}} \Delta \phi \left[\Delta \Psi \left(1 + U_G \frac{1}{C_G} \frac{\partial C_G}{\partial U_G} \right) - e^{\frac{i\phi}{2}} \Delta \phi \left(1 + \frac{\alpha_G}{C_G} \frac{\partial C_G}{\partial \alpha_L} \right) \right] \right. \\ & \left. + \frac{\rho_L}{\alpha_L} C_L CFL_L^2 e^{\frac{i\phi}{2}} \Delta \phi \left[\Delta \Psi \left(1 + U_L \frac{1}{C_L} \frac{\partial C_L}{\partial U_L} \right) - e^{\frac{i\phi}{2}} \Delta \phi \left(1 + \frac{\alpha_L}{C_L} \frac{\partial C_L}{\partial \alpha_L} \right) \right] \right. \\ & \left. - \Lambda \left(\frac{(1 + CFL_G \Delta \Psi)}{\alpha_G} \frac{\partial \wp}{\partial U_G} - \frac{(1 + CFL_L \Delta \Psi)}{\alpha_L} \frac{\partial \wp}{\partial U_L} \right) \right. \\ & \left. - \Lambda \frac{\partial \mathcal{F}}{\partial \alpha_L} \Delta t - \Delta t \left(\frac{(1 + CFL_G \Delta \Psi)}{\alpha_G} \frac{\partial \mathcal{F}}{\partial U_G} - \frac{(1 + CFL_L \Delta \Psi)}{\alpha_L} \frac{\partial \mathcal{F}}{\partial U_L} \right) \right. \\ & \left. - \Lambda^2 \left(\frac{\Delta P_{dynL}}{\alpha_L} + \frac{\Delta P_{dynG}}{\alpha_G} + \frac{\partial \wp}{\partial \alpha_L} - \sigma \left[\frac{1}{D \alpha_G^{1.5}} + \frac{D}{4\sqrt{\alpha_G}} e^{i\phi} \left(\frac{\Delta \phi}{\Delta x} \right)^2 \right] \right) \end{aligned} \quad (6.48)$$

$$b_2 = \Delta t \left(\frac{1}{\alpha_L} \frac{\partial \mathcal{F}}{\partial u_L} - \frac{1}{\alpha_G} \frac{\partial \mathcal{F}}{\partial u_G} \right) \quad (6.49)$$

$$c_2 = -\Lambda \frac{\partial \mathcal{F}}{\partial \alpha_L} \Delta t - \left[\frac{(1 + CFL_G \Delta \Psi)}{\alpha_G} \frac{\partial \mathcal{F}}{\partial u_G} - \frac{(1 + CFL_L \Delta \Psi)}{\alpha_L} \frac{\partial \mathcal{F}}{\partial u_L} \right] \Delta t \quad (6.50)$$

Equation (6.45) yields an amplification factor for a particular wavelength. The amplification factor can be converted into a temporal growth rate through the following equation

$$-\omega_i = \frac{G - 1}{\Delta t} \quad (6.51)$$

which allows a comparison between the differential stability analyses and the discrete von Neumann approach. Figure 6.3 shows a typical dispersion relation that can be obtained from a von Neumann analysis for different mesh refinements, represented by the colored continuous lines. As the mesh is refined, the von Neumann curves approach that of the differential analysis.

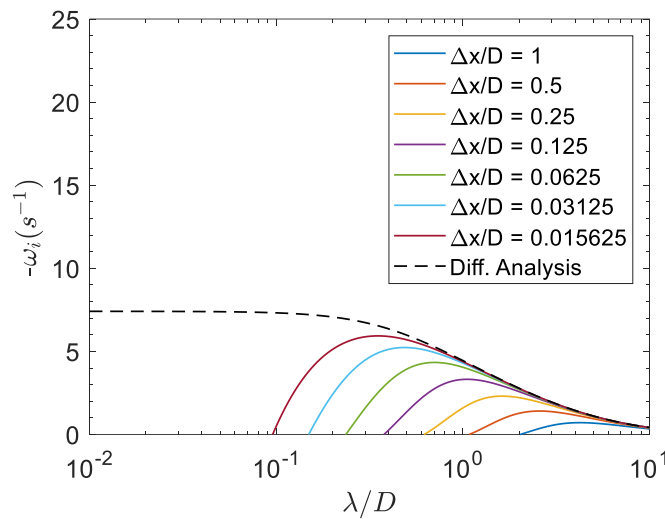


Figure 6.3 - Dispersion relation of the discrete stability analysis.

6.4 Closure Models

In order to evaluate the effects of the closure relations through the optics of linear stability theory, we define the perturbed quantities in terms of the selected closure modes.

6.4.1 Phase and interface pressure difference

In annular flow, the difference between the bulk pressure and the interface pressure are modeled with a dynamic pressure term defined in Eq. (3.31). In the present work, three models are considered. To account for the dynamic pressure term effect on the linear stability calculations, the combined term defined in Eq. (6.5) is a convenient starting point

$$p = \Delta P_{dyn_L} - \Delta P_{dyn_G} = (W_{fL} - W_{fG}) \rho_{ref} (U_L - U_i)^2 \quad (6.52)$$

Further, we define

$$\mathbb{Q} = -\rho_{ref} 2 (U_L - U_i)(W_{fL} - W_{fG}) \quad (6.53)$$

The derivatives of p are then defined in terms of \mathbb{Q}

$$\frac{\partial p}{\partial \alpha_L} = \mathbb{Q} \frac{\partial U_i}{\partial \alpha_L} ; \quad \frac{\partial p}{\partial U_G} = \mathbb{Q} \frac{\partial U_i}{\partial U_G} ; \quad \frac{\partial p}{\partial U_L} = \mathbb{Q} \left(\frac{\partial U_i}{\partial U_L} - 1 \right) \quad (6.54)$$

The interface velocity depends on the dynamic pressure model.

(i) Fowler & Lisseter (1992): $U_i = 2U_L$

$$\frac{\partial U_i}{\partial \alpha_L} = 0 ; \quad \frac{\partial U_i}{\partial U_L} = 2 ; \quad \frac{\partial U_i}{\partial U_G} = 0 \quad (6.55)$$

(ii) Bestion (1990): $U_i = U_G$.

$$\frac{\partial U_i}{\partial \alpha_L} = 0 ; \quad \frac{\partial U_i}{\partial U_L} = 0 ; \quad \frac{\partial U_i}{\partial U_G} = 1 \quad (6.56)$$

(iii) Fontalvo *et al.* (2020): $U_i = U_{Wave}$. The definition of U_{Wave} from Eq. (3.28) can be simplified by defining

$$U_i = \mathfrak{A} + \mathfrak{B} \quad (6.57)$$

where

$$\mathfrak{A} = \mathbb{P} \rho_G^{0.5} U_G^{0.62} \alpha_G^{0.62} U_L^{0.16} \alpha_L^{0.16} ; \quad \mathfrak{B} = \mathbb{P} \rho_L^{0.5} \frac{U_L^{1.16} \alpha_L^{1.16}}{U_G^{0.38} \alpha_G^{0.38}} \quad (6.58)$$

and the auxiliary term \mathbb{P} is defined as

$$\mathbb{P} = \frac{50 / ST_w^{0.13}}{\rho_G^{0.5} + \rho_L^{0.5}} \frac{\left(\frac{D}{v_L}\right)^{0.16}}{\left(\frac{D}{v_G}\right)^{0.38}} ; \quad v_\ell = \frac{\mu_\ell}{\rho_\ell} \text{ with } \ell = G \text{ and } L \quad (6.59)$$

The derivatives are calculated as a function of \mathfrak{A} and \mathfrak{B}

$$\frac{\partial U_i}{\partial U_L} = \frac{0.16 \mathfrak{A} + 1.16 \mathfrak{B}}{U_L} ; \quad \frac{\partial U_i}{\partial U_G} = \frac{0.62 \mathfrak{A} - 0.38 \mathfrak{B}}{U_G} \quad (6.60)$$

$$\frac{\partial U_i}{\partial \alpha_L} = \left(\frac{0.16 \mathfrak{A} + 1.16 \mathfrak{B}}{\alpha_L} - \frac{0.62 \mathfrak{A} - 0.38 \mathfrak{B}}{\alpha_G} \right) \quad (6.61)$$

6.4.2 Shear Stresses

The viscous approach of the linear stability analysis of this work incorporates the force term in the coefficient matrix \mathcal{C} . The perturbed force term is dependent on its derivatives in relation to the flow quantities. They are defined below

$$\begin{aligned} \frac{\partial \mathcal{F}}{\partial U_L} = & \frac{\tau_L S_L}{\alpha_L A} \left(\frac{2}{U_L} + \frac{1}{f_L} \frac{\partial f_L}{\partial U_L} \right) \\ & + \frac{\tau_i S_i}{A} \left(\frac{1}{\alpha_L} + \frac{1}{\alpha_G} \right) \left(\frac{\partial U_{lf}}{\partial U_L} \frac{2}{(U_G - U_{lf})} - \frac{1}{f_i} \frac{\partial f_i}{\partial U_L} \right) \end{aligned} \quad (6.62)$$

$$\frac{\partial \mathcal{F}}{\partial U_G} = -\frac{\tau_i S_i}{A} \left(\frac{1}{\alpha_L} + \frac{1}{\alpha_G} \right) \left[\left(1 - \frac{\partial U_{lf}}{\partial U_G} \right) \frac{2}{(U_G - U_{lf})} + \frac{1}{f_i} \frac{\partial f_i}{\partial U_G} \right] \quad (6.63)$$

$$\begin{aligned} \frac{\partial \mathcal{F}}{\partial \alpha_L} = & \frac{\tau_L S_L}{\alpha_L A} \left(\frac{1}{f_L} \frac{\partial f_L}{\partial \alpha_L} - \frac{1}{\alpha_L} \right) \\ & - \frac{\tau_i S_i}{A} \left(\frac{1}{\alpha_L} + \frac{1}{\alpha_G} \right) \left[\frac{1}{f_i} \frac{\partial f_i}{\partial \alpha_L} + \frac{1}{S_i} \frac{\partial S_i}{\partial \alpha_L} + \left(\frac{1}{\alpha_L} - \frac{1}{\alpha_G} \right) + \frac{\partial U_{lf}}{\partial \alpha_L} \frac{1}{(U_G - U_{lf})} \right] \end{aligned} \quad (6.64)$$

The derivative of the geometrical parameter for annular flow is

$$\frac{1}{S_i} \frac{\partial S_i}{\partial \alpha_L} = -\frac{1}{2 \alpha_G} \quad (6.65)$$

The liquid friction factor proposed by Kosky & Staub (1971) is defined in Eq. (3.20), and its derivatives are defined below

$$\frac{1}{f_L} \frac{\partial f_L}{\partial U_G} = 0 \quad ; \quad \frac{1}{f_L} \frac{\partial f_L}{\partial U_L} = -\frac{24}{U_L} \quad ; \quad \frac{1}{f_L} \frac{\partial f_L}{\partial \alpha_L} = -\frac{24}{\alpha_L} \quad (6.66)$$

The interfacial friction factor derivatives are defined below for each model considered in this work.

(i) Wallis (1969)

$$\frac{1}{f_i} \frac{\partial f_i}{\partial U_G} = 0 \quad ; \quad \frac{1}{f_i} \frac{\partial f_i}{\partial U_L} = 0 \quad ; \quad \frac{1}{f_i} \frac{\partial f_i}{\partial \alpha_L} = \frac{90}{\sqrt{\alpha_G}(1 + 180(1 - \sqrt{\alpha_G}))} \quad (6.67)$$

(ii) Whalley & Hewitt (1978)

$$\frac{1}{f_i} \frac{\partial f_i}{\partial U_G} = -\frac{0.25}{U_G} \quad ; \quad \frac{1}{f_i} \frac{\partial f_i}{\partial U_L} = 0 \quad (6.68)$$

$$\frac{1}{f_i} \frac{\partial f_i}{\partial \alpha_L} = \frac{0.25}{\alpha_G} + \frac{6 \left(\frac{\rho_L}{\rho_G}\right)^{\frac{1}{3}}}{\sqrt{\alpha_G}(1 + 12 \left(\frac{\rho_L}{\rho_G}\right)^{\frac{1}{3}} (1 - (1 - \sqrt{\alpha_G})))} \quad (6.69)$$

(iii) Belt *et al.* (2009)

$$\frac{1}{f_i} \frac{\partial f_i}{\partial U_L} = -\frac{1}{f_i} \frac{\partial f_i}{\partial U_G} = \frac{0.25}{|U_G - U_L|} \quad ; \quad \frac{1}{f_i} \frac{\partial f_i}{\partial \alpha_L} = \frac{0.25}{\alpha_G} + \frac{0.25}{S_i} \frac{\pi D}{2\sqrt{\alpha_G}} \quad (6.70)$$

Three models are examined for the liquid film velocity at the interface U_{lf} : For the first model, $U_{lf} = U_L$, thus $\partial U_{lf}/\partial U_L = 1$; for the second $U_{lf} = 2U_L$ and $\partial U_{lf}/\partial U_L = 2$. For these two models thus $\partial U_{lf}/\partial U_G = 0$, thus $\partial U_{lf}/\partial \alpha_L = 0$. For the third model $U_{lf} = U_{wave}$, and the three derivatives are shown in Eqs. (6.60) and (6.61), for the case that $U_i = U_{wave}$.

6.4.3 Momentum Flux Parameters

The momentum flux parameter can be considered as a constant value, or as a function of the local flow quantities. In Chapter 4, two models were suggested for a variable C_L . Both models are of the form

$$C_L = mRe_L^n + b \quad (6.71)$$

therefore

$$\frac{\partial C_L}{\partial \alpha_L} = 0 \quad ; \quad \frac{\partial C_L}{\partial U_L} = \frac{n}{U_L} mRe_L^n \quad ; \quad \frac{\partial C_L}{\partial U_G} = 0 \quad (6.72)$$

The coefficients are defined in section 4.3. Naturally, for a constant C_L , the derivatives are null. The gas parameter C_G was kept constant.

6.5 Numerical Stability Analysis

As mentioned in previous chapters, Linear Stability Theory (LST) can be used to analyze differential and discrete forms of mathematical formulations and provide valuable insights into their behavior in different conditions. Further, a direct comparison between results of a numerical simulation and the LST can also be obtained from the wave growth of the liquid film. The amplification rates can be extracted by applying a standard Fourier decomposition to the spatiotemporal data of the liquid height. This is performed using the *Fast Fourier Transform (fft)* of Matlab.

Initially, the linear region, i.e., the spatial region where the amplification of disturbances is mostly linear, is defined. The criterion employed to determine the linear region is that only positions where the film fluctuations are below 0.001m are considered. This methodology ensures that nonlinear stability mechanisms are negligible, i.e., only linear stability mechanisms are being captured (see Figure 6.4). For every streamwise location in the numerical mesh within the linear range, the available temporal data can be transformed into the Fourier domain for a frequency band from zero to the Nyquist frequency, defined as $1/(2\Delta t)$. The numerical simulations performed in this work acquire the flow field data at a sampling rate of 1kHz, or $\Delta t = 0.001s$.

From the Fourier decomposition of the temporal data, one can obtain the amplitudes associated with each frequency. By employing this procedure to every location, a spatial series of amplitudes for each frequency is obtained, as shown in Figure 6.5 The dashed red lines in the figures represent the limits of the linear region. By obtaining the derivative of the amplitude spatial evolution, the spatial growth rate k_i can be calculated. Figure 6.5 illustrates the procedure to obtain the spatial growth rate from slope of the wave amplitude data for a particular frequency.

The temporal growth rates can be converted from spatial growth rates through the Gaster transform (Gaster, 1962), based on the wave group velocity C_w

$$-\omega_i = C_w k_i \quad (6.73)$$

Here, C_w is the group velocity, defined as

$$C_w = \frac{d\omega_r}{dk_r} \quad (6.74)$$

where ω_r is the frequency and k_r is the wavenumber. Eq. (6.74) can be calculated numerically from the simulation data.

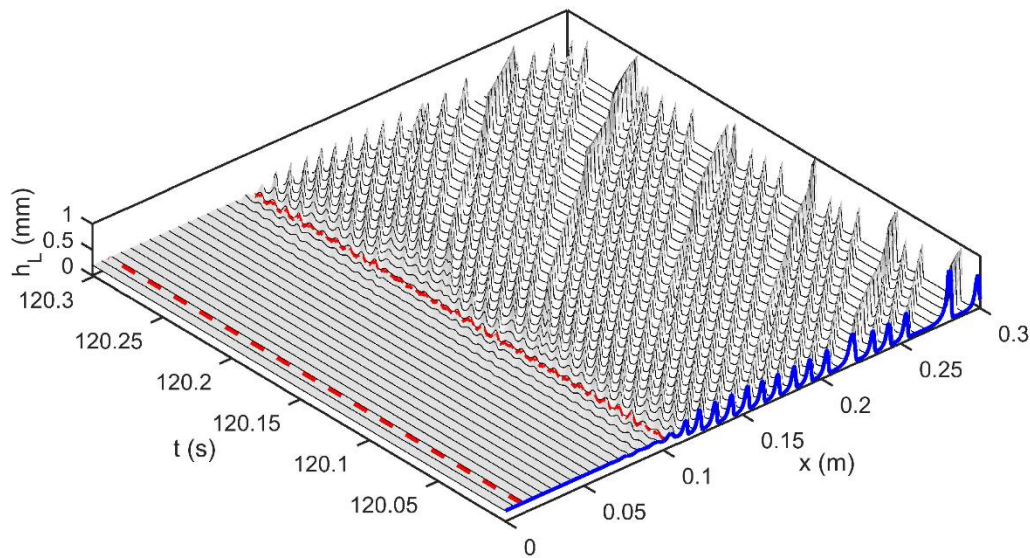


Figure 6.4 – Spatiotemporal wave evolution data, where dashed lines represent the linear growth region.

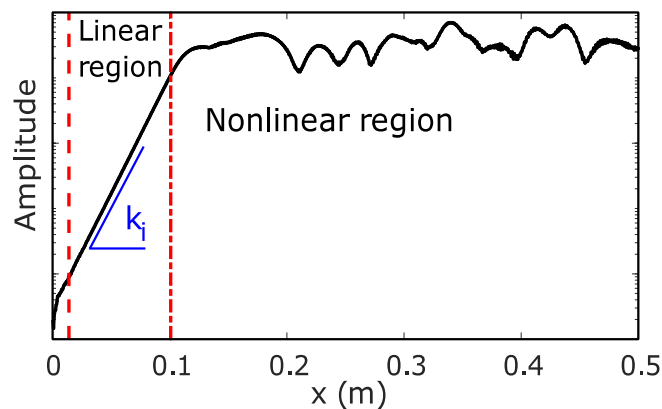


Figure 6.5 – Extraction of spatial growth rates from wave amplitude data.

7 RESULTS AND DISCUSSION

In this chapter, the Two-Fluid model augmented with different combinations of closure models is evaluated with annular flow experimental set-ups and flow parameters of several works. Initially, the experimental cases are selected from the available databases. Then, a set of commonly used closure models selected from the literature (see Chapter 3) are assessed in terms of their ability to stabilize the system of equations, through the optics of a differential and discrete stability analyses. Numerical simulations results are then used for a systematic comparison against the LST. Lastly, the momentum flux parameter models described in Chapter 4 are numerically evaluated against experimental data in terms of accuracy, and results are also compared to the commonly employed constant liquid momentum flux parameter C_L values. The tests are performed with statistical data for liquid film thickness, pressure drop and wave velocity as well as instantaneous timeseries of the liquid film, when available.

7.1 Case Selection

Six experimental works of vertical upward air-water annular flows were selected from the literature and are outlined in Table 7.1. The selected configurations have a reasonable range of diameters, from $D = 19$ mm to 50.8 mm. The cases also show a variability in lengths, where the configuration due to Zhao *et al.* (2013) has the shortest length ($L/D = 58$) and the configuration due to Belt *et al.* (2010) presents the longest pipe ($L/D = 240$). From these works, there is a significant number of available individual cases with varying gas and liquid superficial velocities. Figure 7.1 shows three flow pattern maps indicating the regions where the individual cases are located. The configurations with similar diameters were grouped together in the maps for the sake of simplicity.

Since the current formulation does not predict the entrainment and deposition of droplets into and from the gas core, cases that are too far into the entrainment region must be discarded. Some necessary criteria must be used to limit cases that fall into certain regions. Two criteria were employed to determine the entrainment limits, following the work of Fontalvo (2016).

Table 7.1: Experimental configurations and physical properties of the fluids.

Configuration	Geometry		Gas		Liquid	
	Diam. <i>D</i> (mm)	Length <i>L</i> (m)	Density (kg/m ³)	Viscosity (cP)	Density (kg/m ³)	Viscosity (cP)
I - Kaji (2008)	19.0	6.87	1.75	0.0179	998.2	1.00
II - Zhao <i>et al.</i> (2013)	34.5	2.00	1.18	0.0179	998.2	1.00
III - Fore & Dukler (1995)	50.8	3.50	1.27	0.01827	999.0	1.05
IV - Fershtman <i>et al.</i> (2020)	24.0	10.00	1.18	0.0179	998.2	1.00
V - Wolf <i>et al.</i> (2001)	31.8	10.80	1.95	0.0179	998.2	1.00
VI - Belt <i>et al.</i> (2010)	50.0	12.00	1.18	0.0179	998.2	1.00

Ishii & Grolmes (1975) proposed a critical liquid superficial Reynolds number of $Re_{sLcrit} = 160$ for the onset of entrainment, and a correlation for the gas superficial velocity, as shown below, for $Re_{sL} \leq 1635$

$$\frac{\mu_L U_{sG}}{\sigma} \sqrt{\frac{\rho_G}{\rho_L}} \geq 11.78 N_\mu^{0.28} Re_{sL}^{-\frac{1}{3}} ; \quad N_\mu \leq \frac{1}{15} \quad (7.1)$$

$$\frac{\mu_L U_{sG}}{\sigma} \sqrt{\frac{\rho_G}{\rho_L}} \geq 1.35 Re_{sL}^{-\frac{1}{3}} ; \quad N_\mu > \frac{1}{15} \quad (7.2)$$

For $Re_{sL} > 1635$, the following correlation applies

$$\frac{\mu_L U_{sG}}{\sigma} \sqrt{\frac{\rho_G}{\rho_L}} \geq N_\mu^{0.8} ; \quad N_\mu \leq \frac{1}{15} \quad (7.3)$$

$$\frac{\mu_L U_{sG}}{\sigma} \sqrt{\frac{\rho_G}{\rho_L}} \geq 0.1146 ; \quad N_\mu > \frac{1}{15} \quad (7.4)$$

where Re_{sL} and N_μ can be calculated from Eqs. (3.15) and (3.29), respectively.

A second set of criteria for the entrainment limit is devised in the works of Owen & Hewitt (1987). The critical liquid superficial Reynolds number is defined as

$$Re_{sLcrit} = \exp\left(5.8405 + 0.4249 \frac{\mu_G}{\mu_L} \left(\frac{\rho_G}{\rho_L}\right)^{0.5}\right) \quad (7.5)$$

and the gas superficial velocity restriction is given by

$$U_{sG} \geq \sqrt{\frac{(61.240 - 0.0312 Re_{sL}) \sqrt{\sigma g \rho_L}}{\rho_G}} \quad (7.6)$$

Both entrainment curves are also depicted Figure 7.1. It is clear that for lower superficial liquid velocities and intermediary superficial gas velocities, the two criteria somewhat differ in the representation of the entrainment limits.

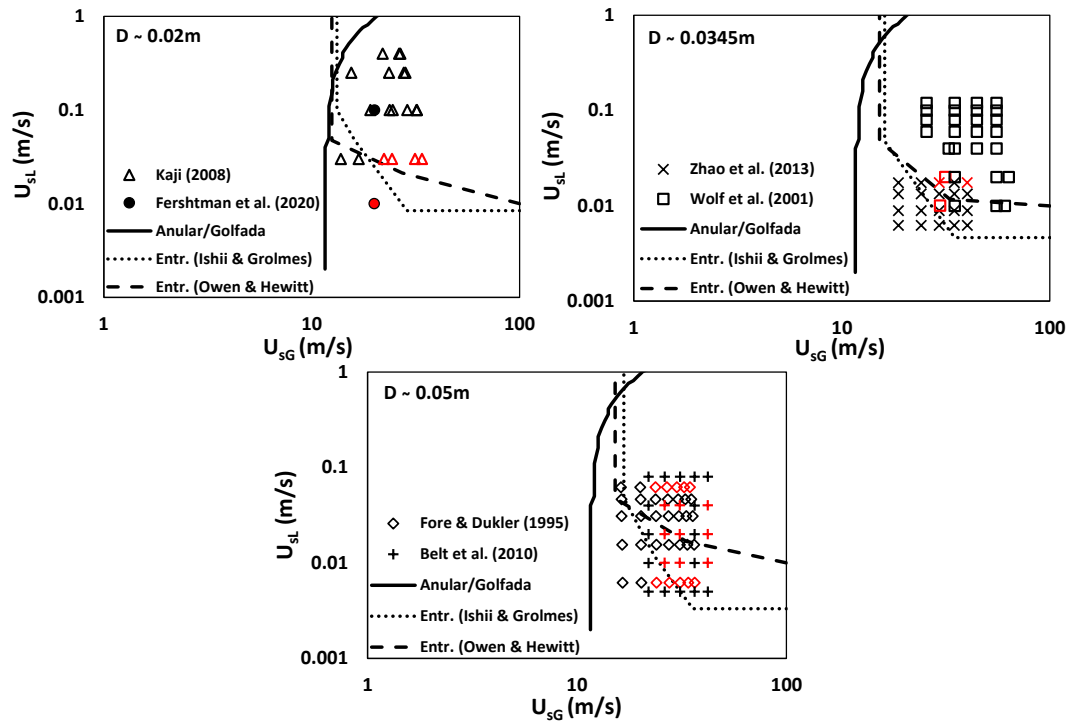


Figure 7.1 – Flow pattern maps of the investigated databases. Selected cases are highlighted in red.

Several cases of the Wolf *et al.* (2001) and Kaji (2008) dataset are far within the entrainment region. Therefore, from these two works, only cases that are in the transition region between the two criteria are selected (two cases from Wolf *et al.* and four cases from Kaji, shown in red in Figure 7.1). From the Zhao *et al.* (2013) configuration, two cases are selected. The cases from the Fore & Dukler *et al.* (1995) and Belt *et al.* (2010) are quite similar both in diameter and in superficial velocities, and a larger number of cases are selected from these configurations, covering a larger range of gas superficial Reynolds numbers. Lastly, the Fershtman *et al.* (2020) case that fell outside both entrainment regions was selected.

Table 7.2 lists the selected cases from each experimental work and their superficial Reynolds numbers, as well as the mean results for statistical quantities of liquid film thickness h_L , pressure drop dp/dx and wave group velocity U_w . The methods by which these quantities are extracted from numerical results are described in Appendix B.

A subgroup from the database shown in Table 7.2 is selected for a more thorough analysis (I-Kaji-1, II-Zhao-2, III-ForeDukler-3, and IV-Fershtman-1).

These cases will be used for the stability analyses results of the next section, as well as mesh convergence results in the numerical results section 7.3. The representative cases are highlighted in gray.

Table 7.2: Experimental database.

Configuration	Re_{sL}	U_{sG} (m/s)	Re_{sG} $\times 10^{-4}$	h_L (mm)	$-dp/dx$ (Pa/m)	U_w (m/s)
I-Kaji-1	569	22.30	4.14	0.2477	1712	2.25
I-Kaji-2	569	24.36	4.52	0.2027	1875	2.48
I-Kaji-3	569	31.42	5.84	0.1705	2451	2.87
I-Kaji-4	569	33.92	6.30	0.1787	2475	2.87
II-Zhao-1	603	29.42	6.69	0.1967	790	-
II-Zhao-2	603	40.10	9.12	0.1500	1055	-
III-Fore-Dukler-1	300	24.0	7.87	0.338	310	0.88
III-Fore-Dukler-2	300	27.6	9.06	0.308	378	0.89
III-Fore-Dukler-3	300	31.0	10.2	0.279	434	1.04
III-Fore-Dukler-4	300	34.0	11.2	0.265	490	1.54
III-Fore-Dukler-5	300	36.5	12.0	0.272	539	1.75
III-Fore-Dukler-6	3000	23.7	7.78	0.572	889	1.81
III-Fore-Dukler-7	3000	26.9	8.83	0.496	994	2.21
III-Fore-Dukler-8	3000	30.0	9.84	0.443	1100	2.42
III-Fore-Dukler-9	3000	32.5	10.7	0.405	1194	2.54
III-Fore-Dukler-10	3000	34.6	11.4	0.405	1273	2.67
IV-Fershtman-1	240	20	3.16	0.085	-	2.25
V-Wolf-1	317	29.72	6.23	0.142	1166	2.24
V-Wolf-2	635	31.43	6.59	0.1867	1479	2.54
VI-Belt-1	500	26.2	8.64	0.2664	-	1.53
VI-Belt-2	500	31	10.2	0.2206	-	1.85
VI-Belt-3	500	42.1	13.9	0.1641	-	2.41
VI-Belt-4	1000	26.2	8.64	0.3311	-	1.77
VI-Belt-5	1000	31	10.2	0.2720	-	2.07
VI-Belt-6	1000	42.1	13.9	0.1945	-	2.61
VI-Belt-7	2000	26.2	8.64	0.4413	-	1.96
VI-Belt-8	2000	31	10.2	0.3599	-	2.27
VI-Belt-9	2000	42.1	13.9	0.2486	-	2.80

7.2 Stability Analysis Results

The cases I-Kaji-1, II-Zhao-2, III-ForeDukler-3, and IV-Fershtman-1 were selected out of the group to be used in the stability analysis tests. As mentioned in previous sections, the viscous approach of the Kelvin-Helmholtz and the discrete von Neumann analyses are performed here to investigate the hydrodynamic

stability properties of commonly employed closure models.

In the discrete analysis, the second order TVD van Leer scheme was employed for all tests, with mesh spacings varying from $\Delta x/D = 1$ to 0.015625, and the CFL_G value, Eq.(6.40), is kept constant equal to 0.5.

7.2.1 The effect of surface tension

The pressure-jump term $P_{Gi} - P_{Li} = \sigma\kappa$ is known to have a stabilizing effect on the 1D Two-Fluid model. As mentioned, it counteracts wave growth by drawing the interface to a flat state. Since this effect is proportional to the curvatures, it is amplified when acting on short wavelength disturbances. As discussed in Chapter 3, there are two curvature directions in annular flow. The curvature in the axial direction has stabilizing effects in the flow through the surface tension term, whereas the radial direction holds a destabilizing effect. Nevertheless, the axial direction has a predominant effect, which determines the overall behavior.

Figure 7.2 shows the effect of the surface tension term against the standard 1D Two-Fluid Model (without any additional stabilizing term, i.e., neither dynamic pressure models nor momentum flux parameters $\neq 1$) for the different configurations. Here, the Whalley & Hewitt interfacial friction factor correlation f_{iII} , Eq. (3.23), was employed, with $U_{lf} = U_L$. The curves shown in the figure correlate the temporal growth rate $-\omega_i$ with frequency ω_R . The colored curves represent the von Neumann stability analyses for different levels of mesh refinement, whereas the dashed curve represents the VKH analysis. The left column represents the case without the surface tension term ($P_{iG} = P_{iL}$). The results clearly show that the cases without surface tension present unbounded growth of short wavelength (high frequency) disturbances, characterizing an ill-posed state in a stability sense. The inclusion of the surface tension term (right column) introduces a cut-off wavelength in the differential analysis, above which all disturbances are completely damped, characterizing a well-posed unstable scenario. Thus, mesh convergence can be clearly attained, as shown by the von Neumann curves. However, these results also suggest that additional regularization mechanisms are necessary to ensure that mesh convergence is attained at practical grid sizes.

Although a cut-off value is introduced in the differential curve, a small damping effect is observed in a von Neumann sense, i.e., the influence of surface tension is only ever significant for very refined meshes. For the IV-Fershtman-1 case, the observed effect was more significant for coarser meshes.

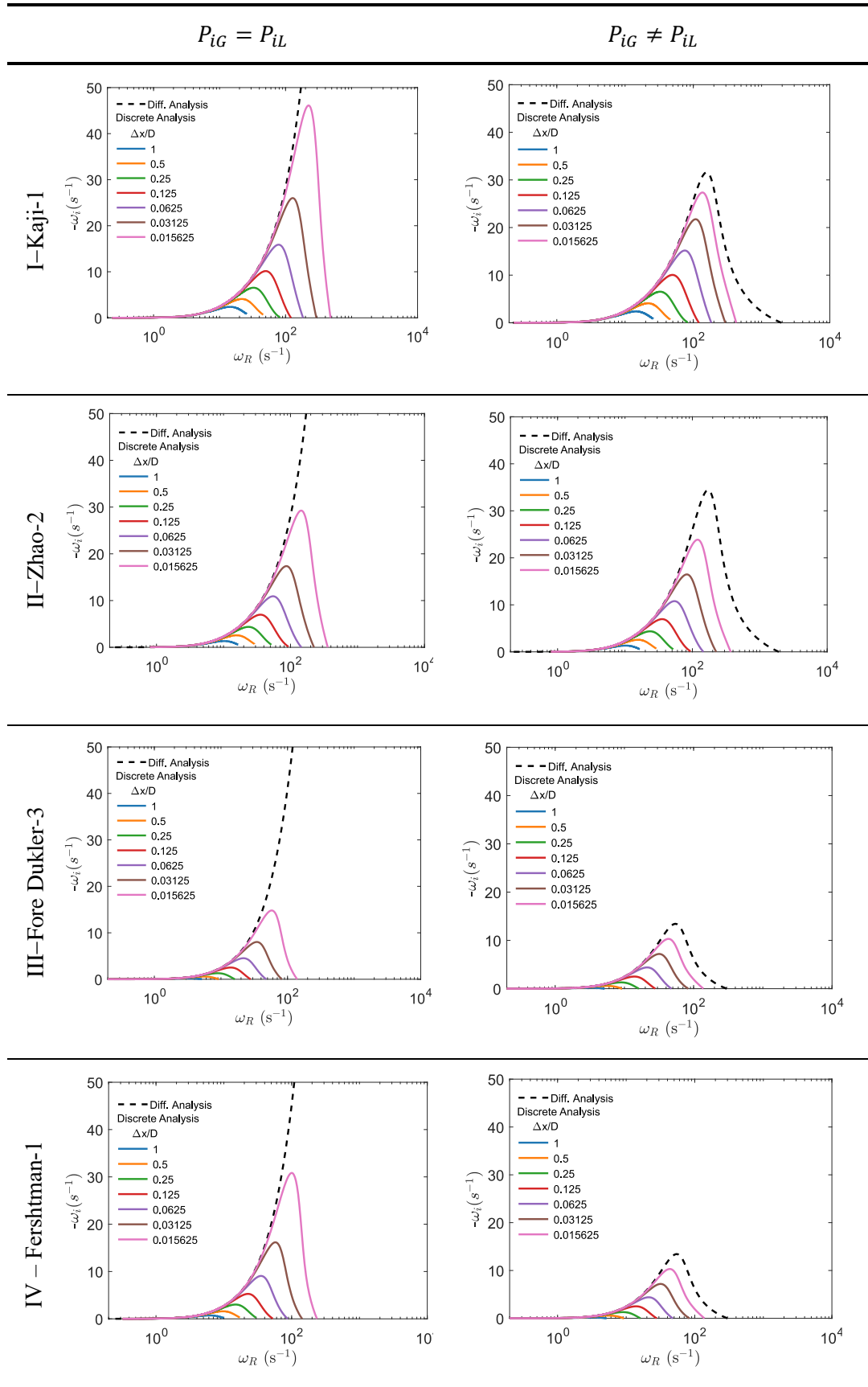


Figure 7.2 – Influence of surface tension in the amplification rates of all configurations.

$$\Delta P_{dyn_\ell} = 0; C_\ell = 1, \ell = G, L; U_{lf} = U_L.$$

7.2.2 Interfacial friction factor

The three interfacial friction factor correlations, combined with the three film velocities U_{lf} are evaluated here through the optics of linear stability theory. For this test, the surface tension term was included, but no other regularization term ($\Delta P_{dyn_\ell} = 0$, $C_\ell = 1$, $\ell = G, L$) was considered.

Initially the film velocity is maintained equal to the liquid velocity, and the different friction factor correlations were varied. The dispersion curves in Figure 7.3 show that, although there are some differences in the maximum growth rates achieved for each mesh refinement curves and for the differential analysis, the results are quite similar. The third friction factor model f_{iIII} yields the most unstable configuration, and the second friction factor model f_{iII} promotes higher damping of the differential growth rate curves. Nearly no difference is observed for discrete curves of coarse and intermediary grids, $\Delta x/D = 1$ to 0.125, which shows that this closure relation may not play as a significant role in guaranteeing well-posedness as others. From the Linear Stability Analyses, no information regarding the physical soundness of the models can be obtained, such that this evaluation is limited to whether the models influence wave growth, and in what way.

Next, the effect of the liquid film velocity U_{lf} in the stability properties of the 1D model is explored. Figure 7.4 shows a grid resolution test of the maximum growth rate $-\omega_{I_{max}}$ and its associated dominant frequency ν_{DOM} , extracted from dispersion relation curves of the von Neumann analysis for each friction factor model, combined with the three models for the liquid film U_{lf} . The results show that no influence in wave growth is observed for any of the evaluated cases. Very small variations in the $-\omega_{I_{max}}$ curve can be seen. Once again, the physical soundness of each model cannot be addressed through a stability analysis. For further sections, the standard $U_{lf} = U_L$ model was employed.

Fontalvo *et al.* (2020) performed an extensive analysis of these interfacial friction factors and concluded that a combination of a small momentum flux parameter of $C_L = 1.05$, the dynamic pressure model $\Delta P_{dyn_{III}}$ and the f_{iII} correlation yielded a better agreement with experimental data for a large dataset. The evaluations of other closure models performed in the following sections will therefore employ the Whaley & Hewitt f_{iII} correlation.

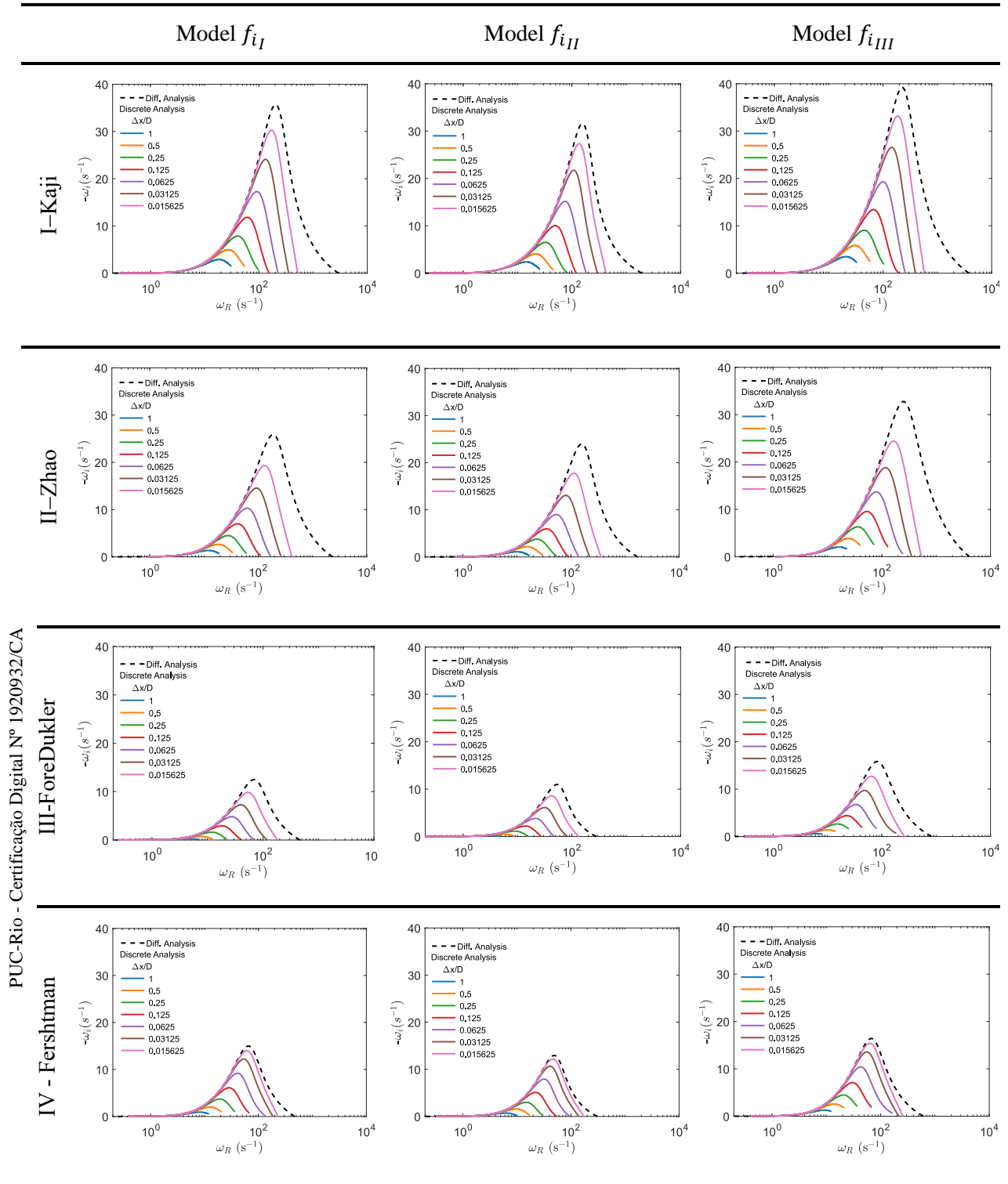


Figure 7.3 – Influence of interfacial friction factors f_i in the amplification rates of all configurations. $P_{iG} \neq P_{iL}$; $\Delta P_{dyn\ell} = 0$; $C_\ell = 1$, $\ell = G, L$; $U_{if} = U_L$.

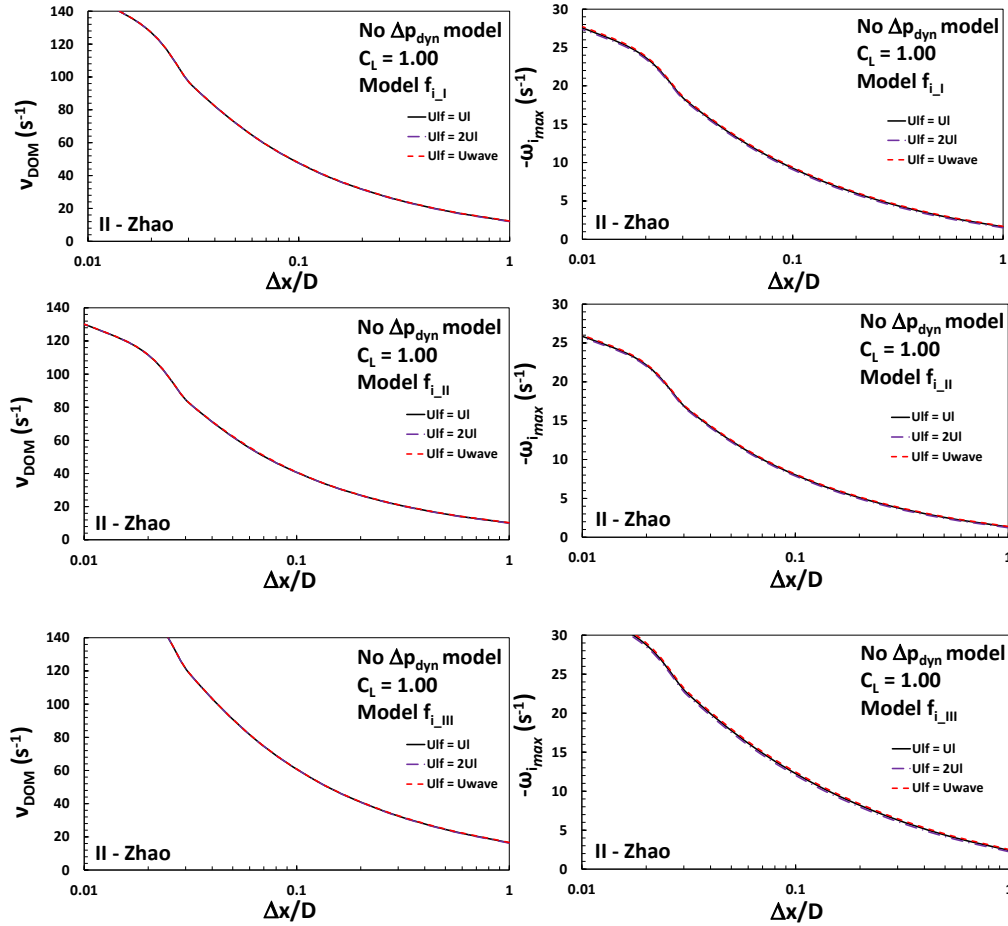


Figure 7.4 - Influence of the liquid film velocity model U_{lf} in the maximum amplification rates and dominant frequencies of all configurations.

$$P_{iG} \neq P_{iL}; \Delta P_{dyn_\ell} = 0; C_\ell = 1, \ell = G, L.$$

7.2.3 Dynamic pressure term

The stability effects of the inclusion of a dynamic pressure term are evaluated here for the different models selected from the literature. For the sake of brevity, we select one configuration to illustrate how each model works to stabilize the flow. Figure 7.5 shows the dispersion curves for the case with no regularization (Figure 7.5a) and the selected ΔP_{dyn} models (Figure 7.5b-d). The chosen configuration for this test was the II-Zhao-2. Results for the remaining three configurations are shown in Appendix C. We observe from the figures that the dynamic pressure models ΔP_{dyn_I} and $\Delta P_{dyn_{III}}$ had little to no damping effect in the discrete curves and were unable to halt the unbounded wave growth as seen in the differential curves. The $\Delta P_{dyn_{II}}$, however, showed significant damping effects for finer meshes ($\Delta x/D = 0.03125$ and 0.015625) and introduced a growth rate plateau at $-\omega_i = 35$ 1/s for very high frequencies, which would characterize the system as well-posed unstable. However, the grid refinement levels that would be required to achieve

mesh convergence with this regularization mechanism are virtually unattainable.

Additionally, for practical mesh sizes, no observable change in the discrete growth rate curves occurred. The small influence of the dynamic pressure model is likely caused by the low value of the empirical constant W_{fL} in the formulation of models ΔP_{dyn_I} and $\Delta P_{dyn_{III}}$ ($W_{fL} = 0.02$; $W_{fG} = 0$). Figure 7.6 shows effect of varying the W_{fL} constant in the aforementioned dynamic pressure models. Increasing its value yields a significant decrease in the maximum growth rates in the discrete analysis. In fact, a small increase to a value of 0.05 renders the system well-posed for $\Delta P_{dyn_{III}}$, with a growth rate plateau of approximately $-\omega_i = 22$ 1/s. Increasing the constant to 0.5 virtually stabilizes all wavelengths, particularly in the ΔP_{dyn_I} model. In this scenario, the system is well-posed stable, and wave formation does not occur. Thus, careful consideration of the W_{fL} parameter must be performed in terms of its physical soundness.

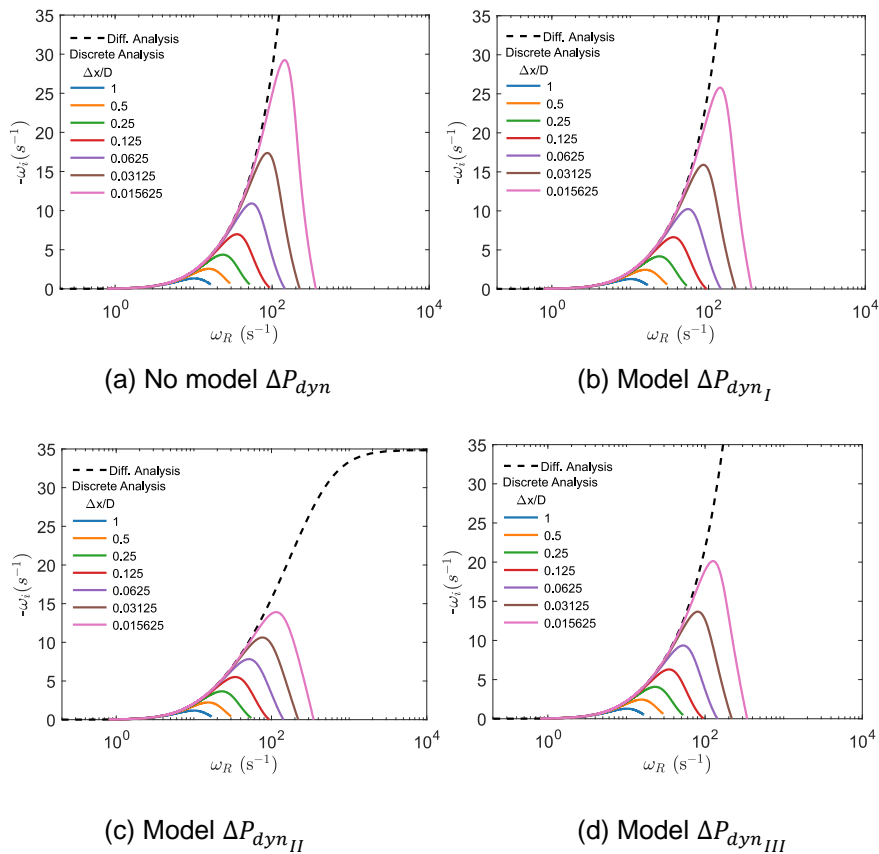


Figure 7.5 – Influence of the dynamic pressure model. Case II-Zhao-2. f_{iII} ; $U_{lf} = U_L$; $P_{iG} = P_{iL}$; $C_\ell = 1$, $\ell = G, L$.

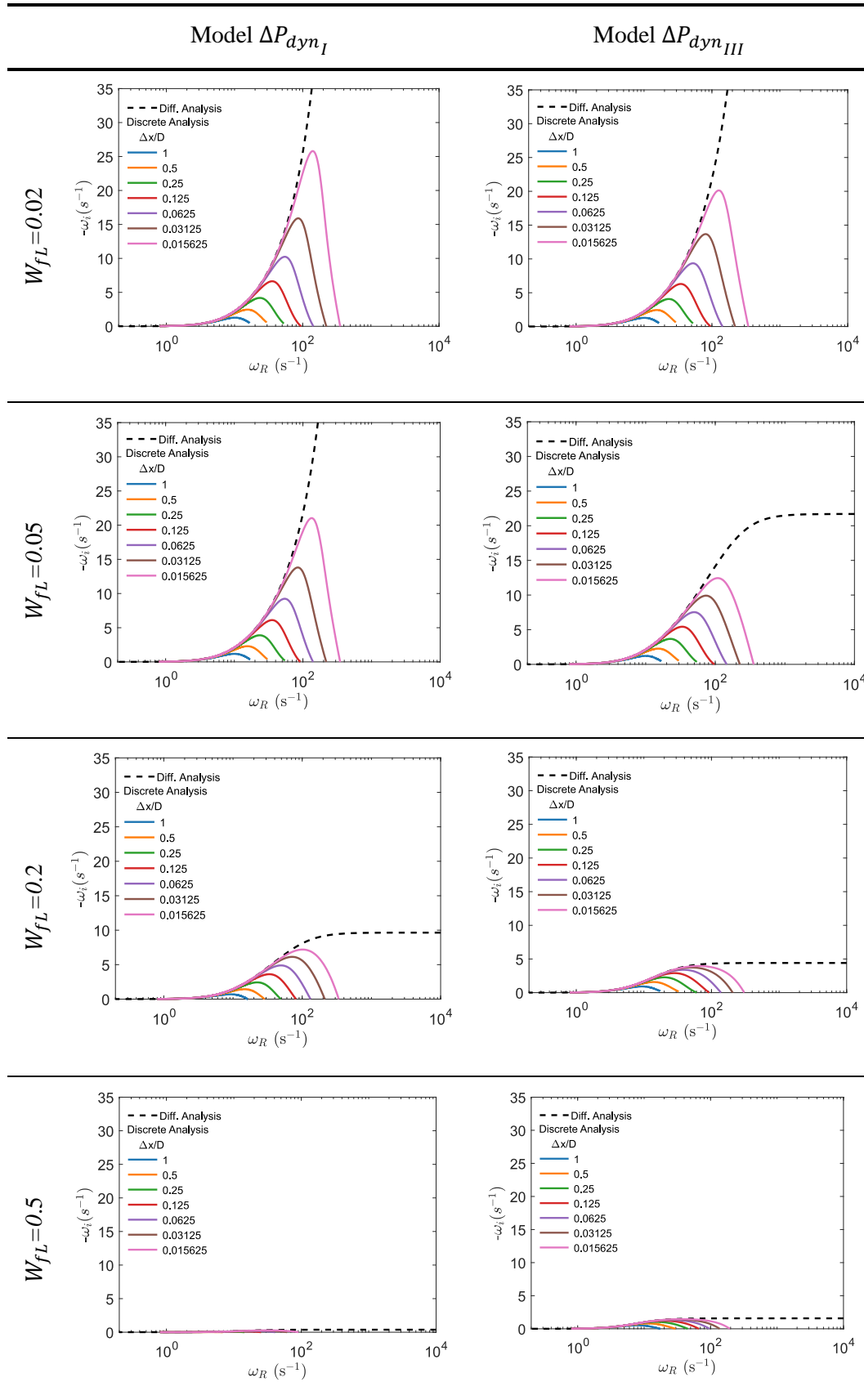


Figure 7.6 - Influence of the W_{fL} constant in the growth rates. Case II-Zhao-2. f_{iII} ; $U_{lf} = U_L$; $P_{iG} \neq P_{iL}$; $C_\ell = 1$, $\ell = G, L$.

7.2.4 Momentum flux parameter

The liquid momentum flux parameter is analyzed here in terms of its ability to guarantee well posedness for the standard 1D Two-Fluid model for the selected cases. No additional closure models were employed for this test ($P_{iG} = P_{iL}$; $\Delta P_{dyn_\ell} = 0$, $\ell = G, L$). Figure 7.7 shows the flow pattern and stability maps for the entire database, with colored curves showing the Inviscid Kelvin Helmholtz limit (i.e., the limit between the well-posed unstable and ill-posed systems) for different C_L values. The area below the curves represents the ill-posed region for that particular C_L . For most of the selected cases, the use of a momentum flux parameter without additional regularization is only enough to ensure well-posedness when the C_L values are high. For the II-ForeDukler-6, a value higher than 1.33 is required to ensure well-posedness. This suggests that, in a stability sense, a constant value of C_L may work well for a subset of cases but may also be exceedingly high or too low for others. This is part of the motivation behind the use of a varying C_L model.

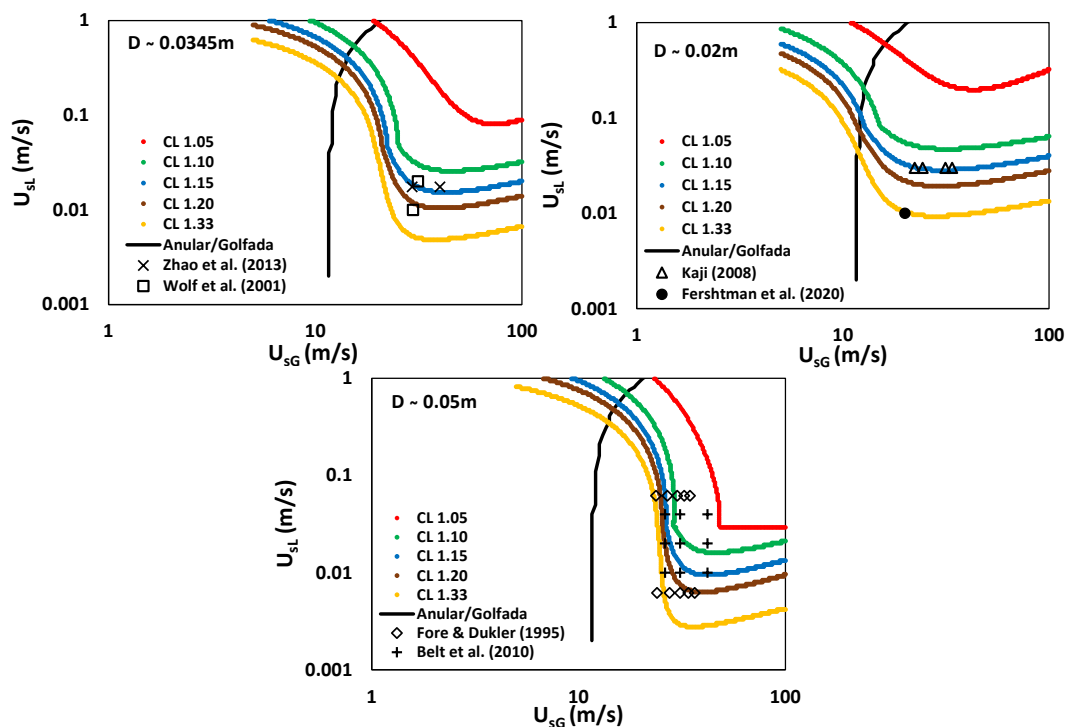


Figure 7.7 – Stability maps showing the IKH limit of well/ill-posed for all configurations.

$$f_{iII}; U_{lf} = U_L; P_{iG} = P_{iL}; \Delta P_{dyn_\ell} = 0, \ell = G, L.$$

Figure 7.9 presents the dispersion curves with varying C_L levels for the I-Kaji-1 configuration. As can be seen, an increase in C_L promotes damping of the discrete curves. The shape factor values of 1.05 and 1.10 yield an ill-posed system,

as evidenced by the unbounded growth of differential curves. The stability map of Figure 7.7 shows that C_L values above 1.15 render the system well-posed for all I-Kaji cases, which is in line with what is observed for the $C_L = 1.20$ and 1.33 dispersion curves, where a growth rate plateau is observed. Results for the other three configurations are shown in Appendix C.

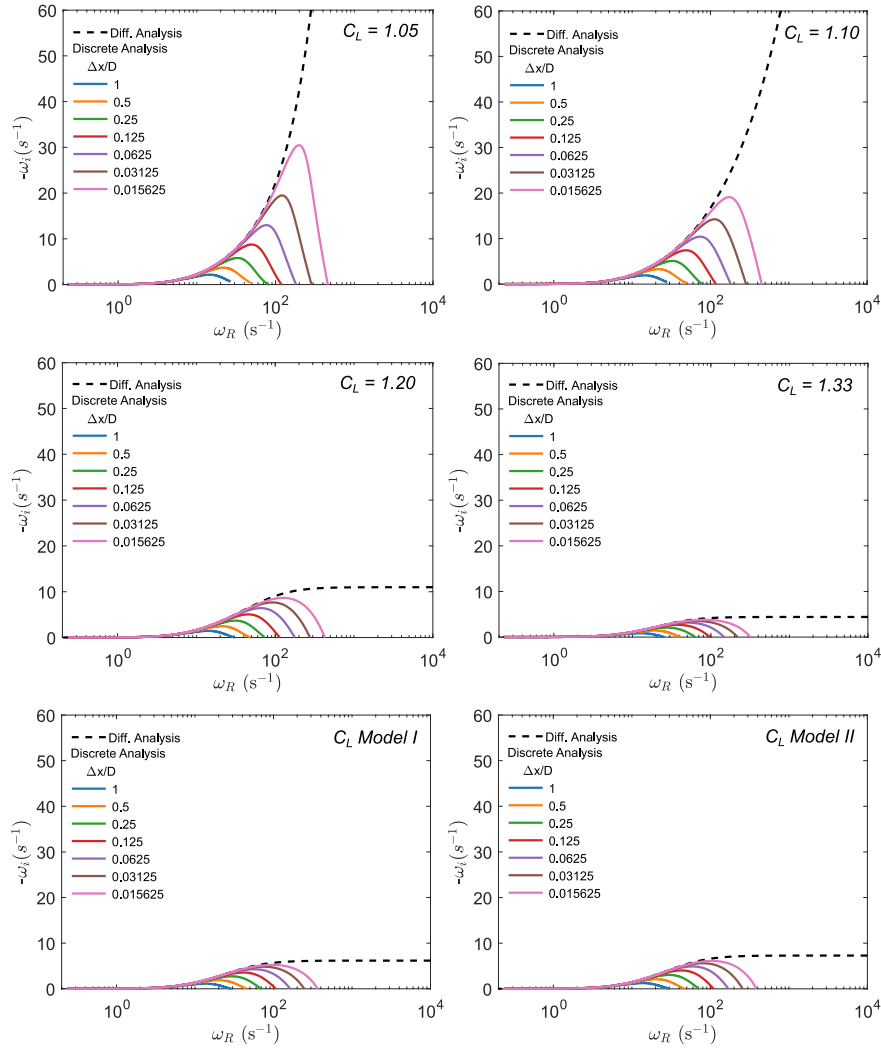


Figure 7.8- Influence of the momentum flux parameter in the growth rates. Case I-Kaji-1.

$$f_{iII}; U_{lf} = U_L; P_{iG} = P_{iL}; \Delta P_{dyn_\ell} = 0, \quad \ell = G, L.$$

The C_L models developed in Chapter 4 are also shown in Figure 7.9. Since there is no wave formation in a stability analysis, the dispersion curves are mostly influenced by the constant C_L values obtained from the variable C_L models. They are calculated from the equilibrium liquid film thickness and superficial velocities. The derivatives of the momentum flux parameters with the flow quantities, Eq.(6.72), also play a role in the dispersion relation curves. The shape factors for the I-Kaji-1 configurations were of 1.2975 and 1.275 for Model I and Model II, respectively. The models show good stability properties for the equilibrium case and can render the 1D Two-Fluid Model well-posed without other regularization

mechanisms. However, the use of additional physically sound closure models (e.g., surface tension) are desirable from a physical fidelity standpoint. In a stability sense, the use of surface tension in addition to the liquid shape factor will not excessively limit wave growth since it does not dissipate energy, and therefore does not damp instabilities.

Figure 7.9 presents the maximum growth rate $-\omega_{i_{max}}$ and the associated dominant frequency ν_{DOM} from the differential curve as a function of the liquid momentum flux parameter. The differential results can be considered as a critical case for when numerical meshes are very refined. The C_L value varies from 1.00 to 1.33 and the effect of surface tension was considered in this test. The results show that the effect of the MFP is small in the dominant frequencies of each configuration, particularly for the III-ForeDukler-3 and IV-Fershtman-1 cases, where growth rate curves are small. The maximum growth rate, however, undergoes radical change when the C_L values are increased, where for a value of 1.33 the values in the I-Kaji-1 and II-Zhao-2 drop from approximately 30 1/s to below 5 1/s.

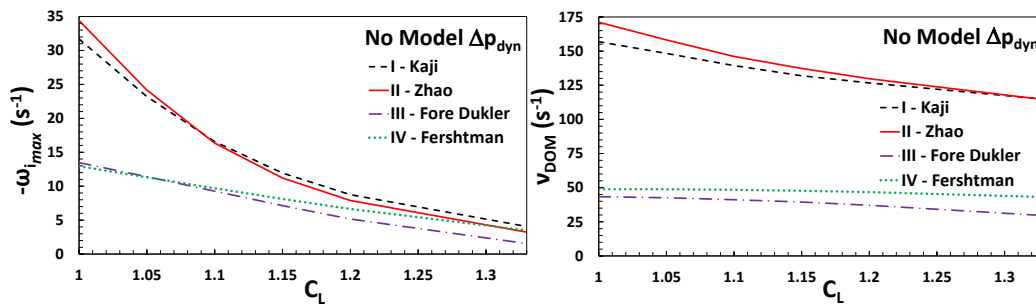


Figure 7.9 - Influence of the momentum flux parameter in stability properties. All cases.

$$f_{iI}; U_{if} = U_L; P_{iG} \neq P_{iL}; \Delta P_{dyn\ell} = 0, \ell = G, L.$$

A dynamic pressure model, however, has the same stability mechanisms as the momentum flux parameter, i.e., the relative velocity between the phases. Therefore, the combination of both parameters may cause some unphysical wave damping. For future tests with the momentum flux parameter, the interfacial pressure jump term will be considered.

7.2.5 Comparison with simulations

Considering the closure relation analysis of the current section, numerical simulations were performed with same configurations that have been evaluated with LST. The simulations were carried out with several constant C_L values within the optimal range (1.05 to 1.33) and the two proposed models. The interfacial

friction factor correlation and liquid film velocity were f_{iII} and $U_{lf} = U_L$, respectively and surface tension was considered ($P_{iG} \neq P_{iL}$). No dynamic pressure models were employed in this numerical study. Spatial growth rates were extracted from the simulation results through the methodology described in Section 6.5, at a frequency range around the maximum growth rate. Figure 7.10 presents the numerical growth rates for the II-Zhao-2 configuration (represented by the colored square symbols) against the discrete and differential growth rates (colored and dashed curves, respectively).

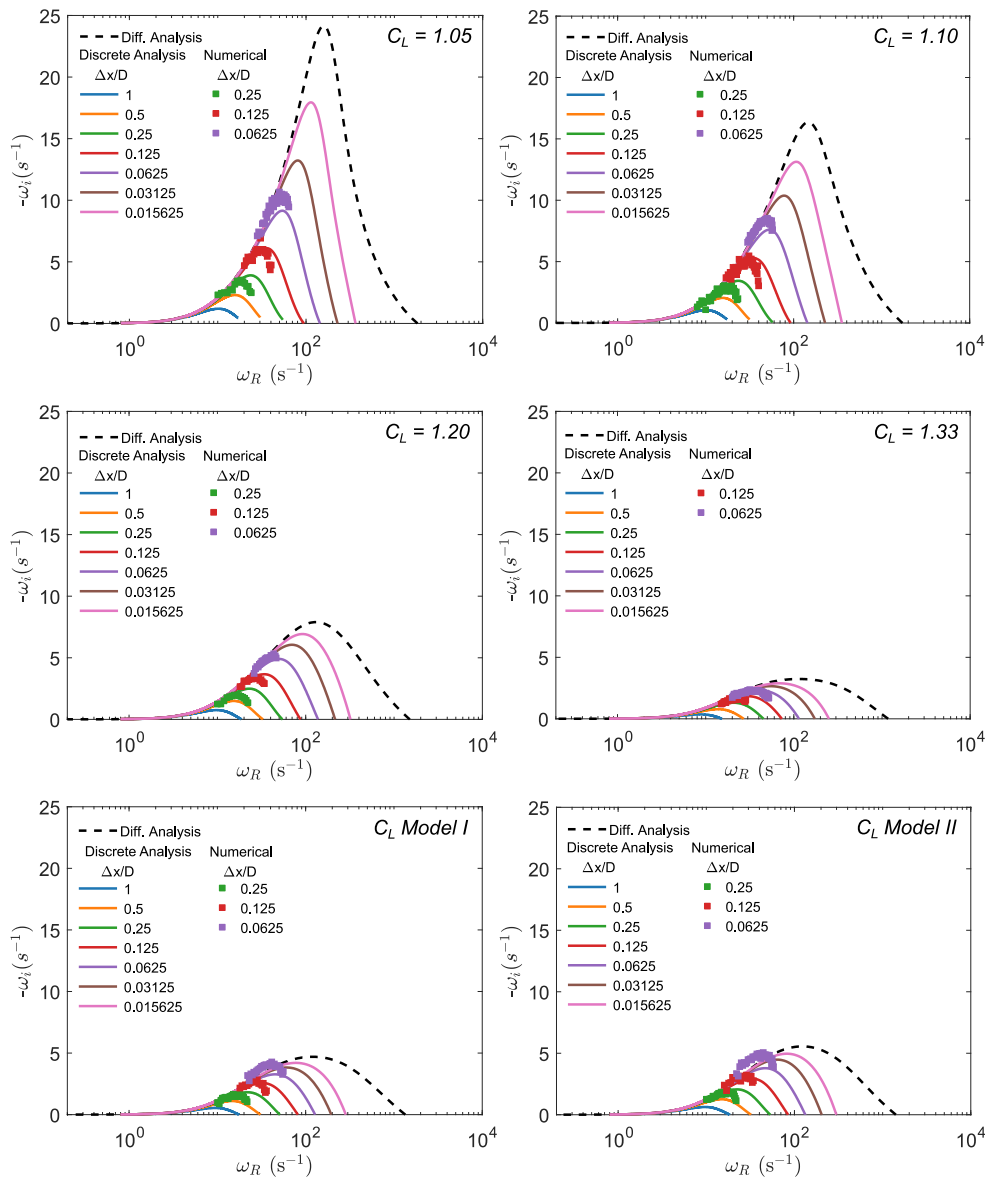


Figure 7.10- Comparison between linear stability analysis and numerical stability properties obtained from simulations. Case II-Zhao-2. f_{iII} ; $U_{lf} = U_L$; $P_{iG} \neq P_{iL}$;

$$\Delta P_{dyn\ell} = 0, \quad \ell = G, L.$$

Examining Figure 7.10, it can be seen that although the range of mesh refinements was $\Delta x/D = 1$ to 0.0625, the spatial growth rates for coarser meshes could not be extracted from the data, as the growth rate spectrum was noisy. The results for the finer meshes showed good agreement against the linear stability analyses, with slight overpredictions for the finer mesh in the variable C_L models. The damping effect of the momentum flux parameter is equivalent in both methodologies. These results suggest that the LST can accurately reproduce the behavior of the numerical model at the linear stage, where the onset of wave formation occurs. Further, linear stability analyses were shown to be an important tool to determine the effect of closure relations in the system and aid in the numerical modelling of multiphase flows in pipes.

7.3 Impact of the Momentum Flux Parameter in Simulation Results

The previous sections have shown, through LST, that the novel C_L models can regularize the 1D Two-Fluid model on their own and show good stability properties. A comparison against numerical growth rates has shown that the linear stability analyses can accurately predict the numerical behavior in the linear region. The current section aims to further evaluate the C_L models through rigorous mesh convergence tests and comparisons against experimental data for statistical quantities. The grid resolution tests were carried out with the configuration subgroup of I-Kaji-1, II-Zhao-2, III-ForeDukler-3, and IV-Fershtman-1.

In all tests discussed in this section regarding the momentum flux parameter, the friction factor f_{iH} correlation of Whalley & Hewitt (1978) was employed, and the liquid film velocity was set equal to the liquid velocity ($U_{lf} = U_L$). Further, surface tension was also included ($P_{iG} \neq P_{iL}$), but no dynamic pressure term $\Delta P_{dyn\ell} = 0$, $\ell = G, L$.

7.3.1 Numerical parameters

Before presenting the simulation results, the numerical parameters are defined. The spatial discretization is performed with a TVD scheme, since as mentioned in Chapter 5, the TVD van Leer discretization has been shown in previous works to be less diffusive, which prompts the formation of waves at coarser mesh refinements in comparison with a 1st order Upwind scheme (Fontalvo *et al.* 2020). For time integration, a 1st order implicit Euler is used, due to its stability properties. In order to validate the use of a first order time integration method, a

timestep convergence test is performed for a representative case of III-ForeDukler-3. Results are presented in Figure 7.11 in terms of the Courant number (Eq. (5.52)) for pressure gradient and mean liquid film thickness. The y axis is normalized by the experimental values, and dashed lines represent 20% error margins.

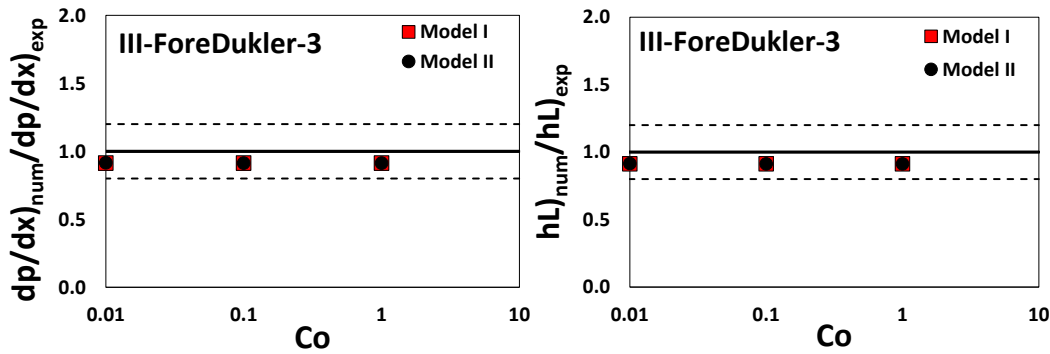


Figure 7.11- Timestep convergence test for pressure gradient and mean liquid film thickness. Case III-ForeDukler-3.

A clear convergent solution is obtained even for low Co numbers. For further tests, a $Co = 0.5$ is employed. The simulations were run for 100s to achieve a statistically steady state regime, and an additional 30s for the data acquisition and analysis of the flow parameters.

7.3.2 The effect of wave development

Firstly, a preliminary test is performed with numerical results to understand and evaluate the behavior of the novel momentum flux models and their influence on wave growth. The II-Zhao-2 configuration is selected as a representative case. An intermediary mesh refinement of $\Delta x/D = 0.125$ is selected.

Figure 7.12 shows a spatial variation of the instantaneous liquid film thickness at $t = 100$ s and the correspondent spatial series of the C_L values calculated by Model I and Model II. Naturally, for the linear region, a nearly constant C_L value is obtained. The onset of waves prompts a significant variation in the momentum flux parameter, to account for the changes in the velocity profiles due to the acceleration of the gas-liquid interface. For the liquid film height between waves, which is considerably narrower, the shape factor approximates that of a Couette flow, 1.334, as seen in both models. As the disturbance waves begin to form, the shape factor drops to lower values, 1.158 and 1.116 for Model I and II, respectively. The tendencies obtained with the simplified models are in line with the physical interpretation of the momentum flux parameter based on the shape of the velocity distribution.

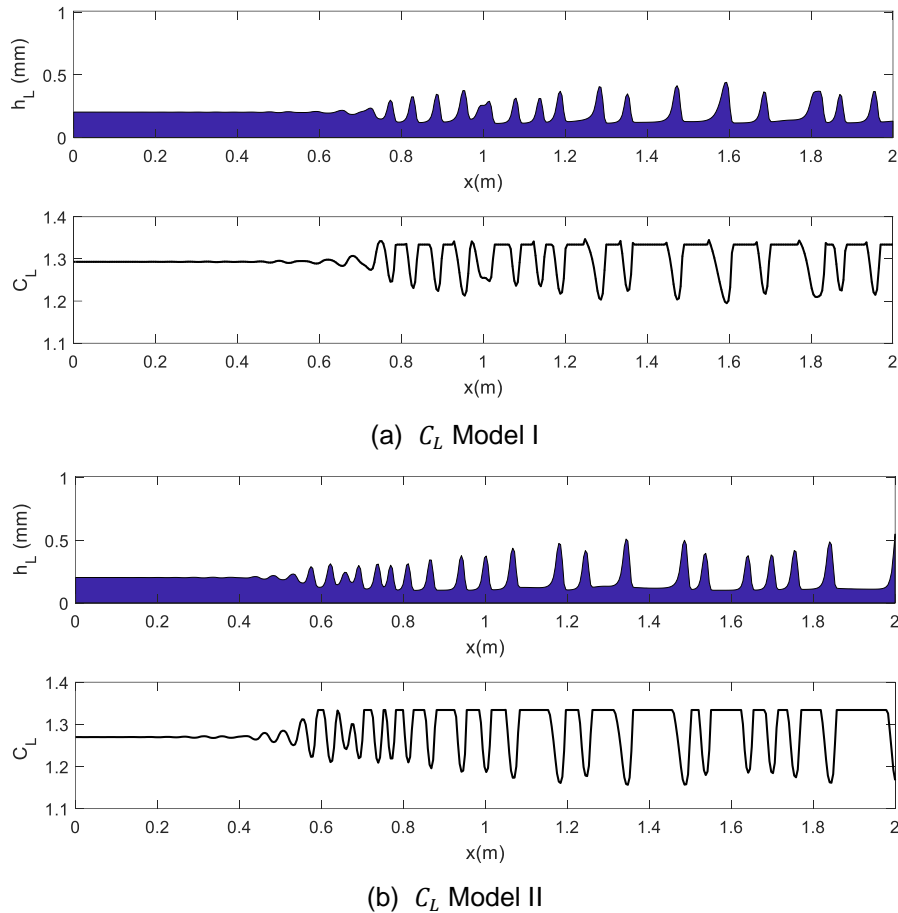


Figure 7.12- Spatial variation of the instantaneous liquid film thickness and the correspondent C_L values calculated by (a) Model I and (b) Model II. Case II-Zhao-2.

The liquid momentum flux parameter is known to damp the disturbances of the flow, thereby limiting wave growth. This has been seen in both numerical simulations with constant C_L values and through discrete and differential stability analyses. Castello Branco *et al.* (2021) have shown that in both linear and nonlinear regimes, the momentum flux parameter behaves as a low-pass filter, which suppresses short wavelength formations at the linear region and reduces the amplification factor of the flow. The result of that is a spatial delay in the onset of wave development, which can be seen in the spatiotemporal variations of the liquid film height, shown in Figure 7.13 for a constant 1.05 value and the two proposed models, for the II-Zhao-2 configuration. Only half of the domain is explored in this analysis. The lower C_L value (Figure 7.13a) has a limited effect in damping the instabilities, therefore an earlier development of disturbances and higher amplitude waves are obtained. The coalescence of waves and increase in wave velocity are seen in the intersection points between individual waves and the subsequent curved trajectories of the resulting structure. The C_L Model I (Figure 7.13b) yields a significant increase in damping of instabilities, as shown by the delay in wave formation and lower wave heights. Model II (Figure 7.13c) shows a

similar trend, although the damping effect is slightly smaller than for Model I, and wave formation occurs at a shorter distance from the inlet.

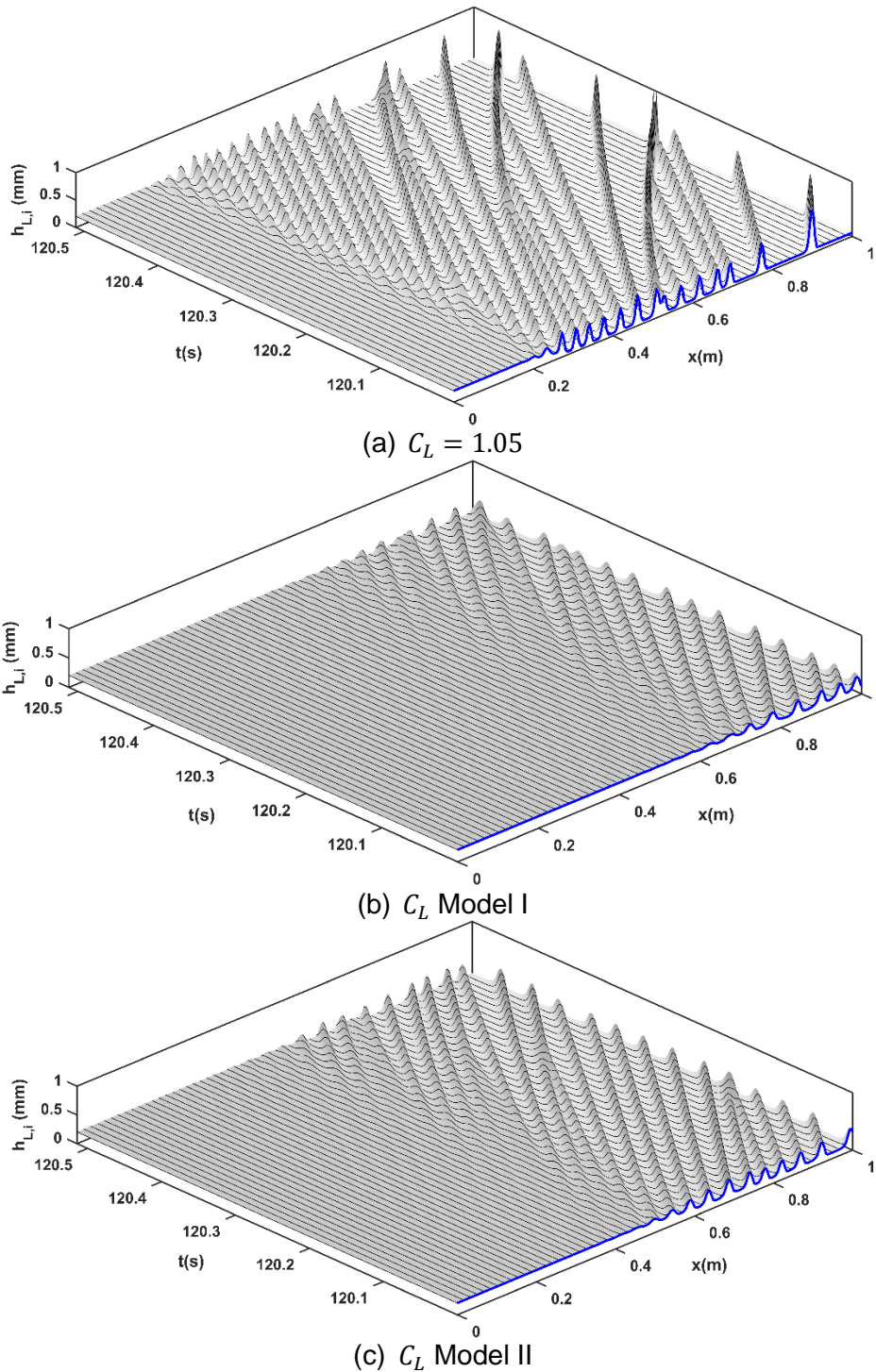


Figure 7.13- Spatiotemporal variation of the instantaneous liquid film thickness for a constant $C_L = 1.05$ and the proposed models. Case II-Zhao-2.

Although the C_L values of both models drop significantly when representing the velocity profile of roll waves, the range of C_L values of both models for this configuration are approximately of 1.15-1.33 and 1.12-1.33 for Model I and Model

II, respectively, which promotes the stabilizing effect seen in the spatiotemporal data. As discussed, the damping effect also increases the linear region of the flow, as the amplification factor is reduced, and waves develop more slowly. According to the criteria of section 6.5, the linear regions for Models I and II are 0-0.3283m and 0-0.2635m, respectively. For comparison, a constant $C_L = 1.05$ value produces a linear range of 0-0.1210m.

7.3.3 Pressure gradient

In this section, numerical results for pressure drop are evaluated against experimental data. Both models and constant C_L values are evaluated. The experimental work of IV-Fershtman-1 does not present data for pressure drop, therefore only data from the I-III sets are explored here.

In order to obtain the pressure gradient at the statistically developed region from the pressure field, some measures must be carried out. To limit entrance effects from influencing the data, a spatial region far from the inlet is selected. For the I-Kaji configuration, which has the longest pipe from this group, a region of 3.5-6.87m is selected; from II-Zhao, a region of 1-2m is chosen; and from III-ForeDukler, the selected range is 1-3.5m.

As mentioned, to ensure that a statistically steady state regime has been attained, the simulation is run for 100s before the data acquisition is commenced. Figure 7.14 shows the time variation of pressure at $x = 1$ m (in blue) and its mean value (in black). After an initial transient of about 60s, the statistically steady regime is attained. The dashed red line indicates the threshold of the data acquisition phase.

Figure 7.15 shows the results of the grid resolution test for the three configurations. The results are normalized by the experimental value, therefore more accurate predictions should approach the solid black line. The dashed lines indicate the 20% error margins.

For the I-Kaji-1 configuration, all C_L values have shown good convergence tendencies, with C_L 1.10 and the proposed models showing better agreement to experimental data, and lower C_L values of 1.05 and 1.10 presenting higher errors. For the II-Zhao-2 configuration, the opposite trend occurs, where lower C_L values better approach the experimental data. All models converge to solutions within the 20% error bracket. However, the convergence of C_L 1.05 is less stable, as intermediary meshes ($\Delta x/D = 0.25$ and 0.125) predict significantly different solutions from the other mesh refinements levels.

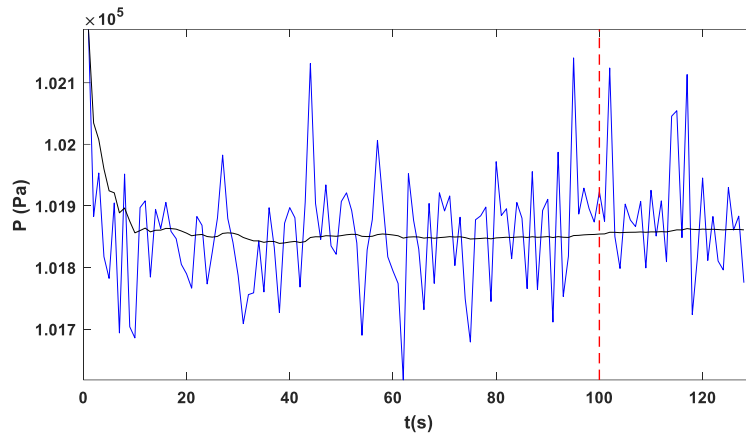


Figure 7.14- Temporal data of the pressure field and mean pressure. Case II-Zhao-2.

Lastly, for the III-ForeDukler-3 case, the C_L Models I and II, and constant C_L values of 1.20 and 1.33 show excellent convergence and good agreement to the experimental pressure gradient. The good convergence trend occurs because the higher C_L values hinder wave formation; thus, the solutions do not vary with mesh refinement. For C_L 1.05 and 1.10, the convergence trend promptly shifts for $\Delta x/D \leq 0.25$ and the solution appears to stabilize outside of the 20% error bracket.

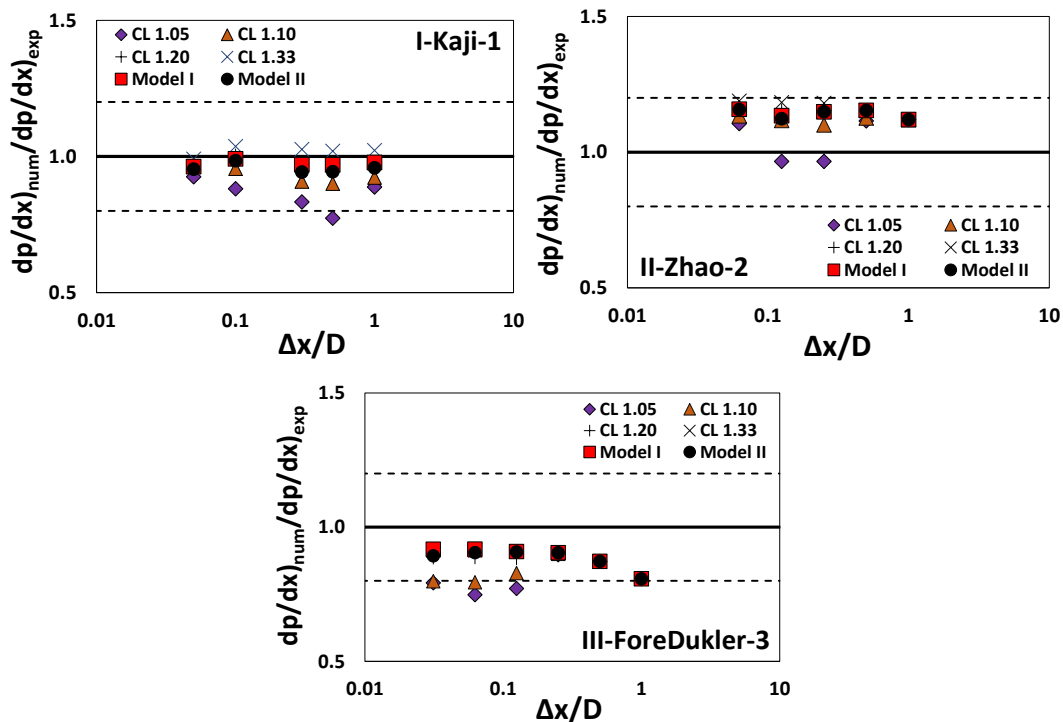


Figure 7.15- Grid resolution tests for pressure gradient, normalized by the experimental value. Dashed lines indicate 20% error margins.

Figure 7.16 presents the numerical versus experimental pressure gradient plot for all C_L values evaluated, with all configurations in the selected dataset where experimental pressure gradient measurements were available. All momentum flux

parameter values and models obtained most predictions within the 20% error margins.

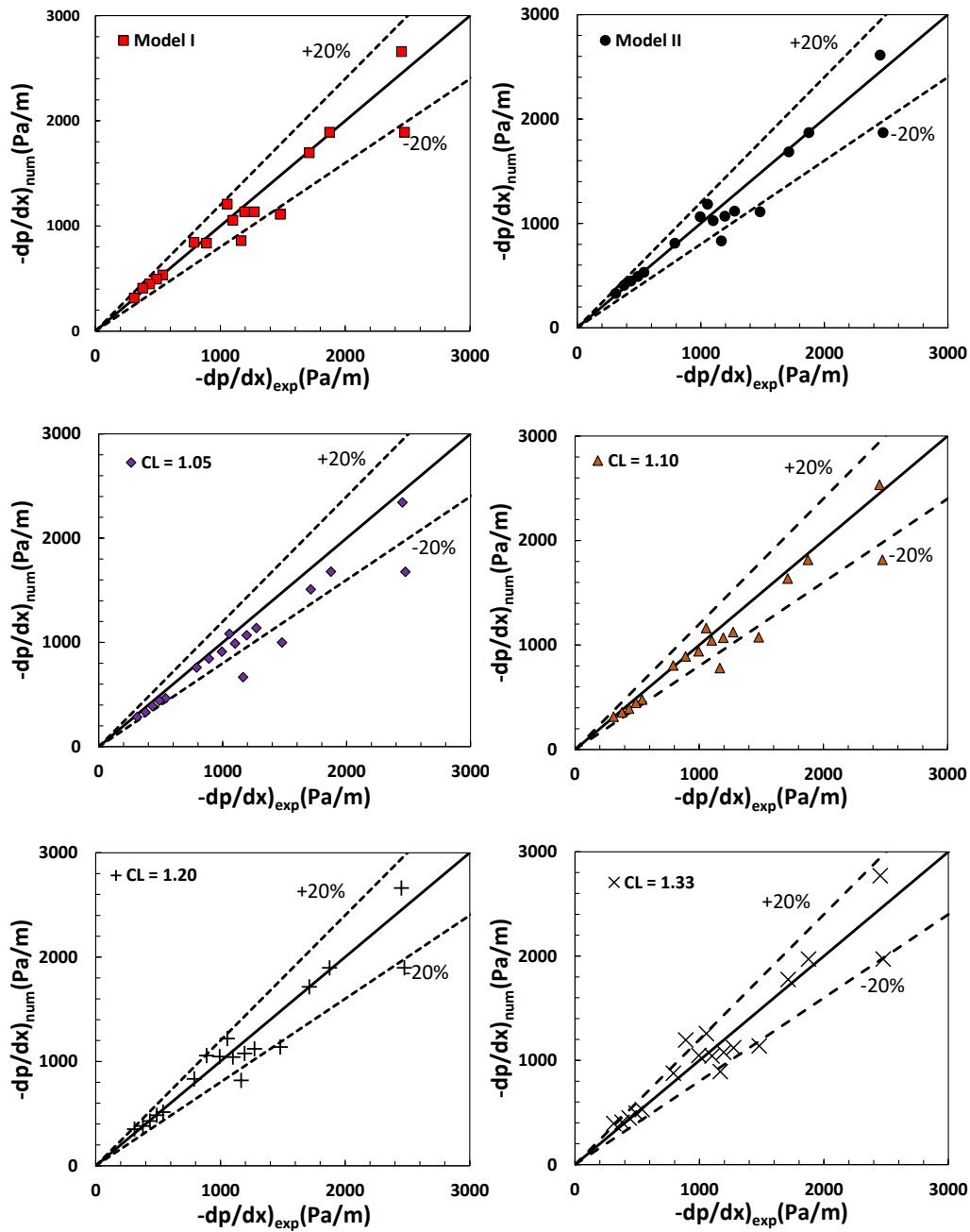


Figure 7.16- Experimental versus Numerical comparisons for pressure gradient. All cases.

It is not possible to visually assert which method had a better performance. Table 7.3 shows the percentage of cases of the database that had prediction errors within the 10% error margin, for each C_L . The variable C_L models have clearly attained better agreement with experimental data, where Model I had 71% of the database in the 10% error bracket. Model II presented a similar trend, with 65% of the configurations. C_L 1.05 had the worst performance, with 39% of the cases.

The trend in varying the constant C_L models, as seen from the errors in Table 7.3, shows that increasing the momentum flux parameter has a positive effect in accuracy, up to a point (i.e., C_L 1.33 overdamps the waves and worsens the predictions). The higher shape factors tend to reduce amplitudes and increase wave frequencies, affecting the shear in the gas stream, which in turn influences the pressure drop. The variable C_L models provide the necessary damping to the waves, as they consider the influence of the film thickness on the velocity shape, with a direct impact in the wall and interface frictions, which explains their good performance.

Fontalvo *et al.* (2020) performed a similar numerical analysis of the constant momentum flux parameter in combination with the $\Delta P_{dyn_{III}}$ model with a large dataset. In their work, C_L values of 1.00, 1.05, 1.20 and 1.33 were assessed. The combined effect of both regularization mechanisms yielded a better performance with $C_L = 1.05$ in comparison to other models, where 96% of the cases fell into the 20% error bracket for pressure gradient predictions. However, for simulations with shape factor values higher than $C_L = 1.05$, the accuracy of the model decreased, as was obtained here in the absence of the dynamic pressure model. In the present work, the constant C_L 1.05 also presented good agreement with experimental data (83% within the 20% error range), however, a lower discrepancy was obtained when compared to other higher constant C_L values (~ 60% for both formulations). The additional stabilizing effect of the dynamic pressure model (which is dependent on an empirical constant, as discussed in section 7.2.3) may have artificially increased the stabilizing mechanisms of the model.

It should be mentioned here that the entrainment of droplets, which is not modelled in the formulation presented in this work, also plays a significant role in the flow. The momentum transfer generated by the presence of droplets in the gas flow can be important in some cases, accounting for up to 20% of the pressure gradient (Fore & Dukler, 1995; Belt, 2007). Thus, the positive effect of shape factors greater than one, may also be attributed to offsetting the effect of entrainment in the flow.

Table 7.3: Percentage of cases within the 10% error margin for pressure gradient.

C_L	0-10% Error margin $-dp / dx$
1.05	39%
1.10	61%
1.20	61%
1.33	50%
Model I	71%
Model II	65%

7.3.4 Film thickness

Numerical results for mean film thickness predictions are also compared against reference experimental data. Both models and constant C_L values are evaluated. The film thickness measurements in the datasets I-III and V were obtained at several conductance probes along the axial direction. The databases IV and VI presented measurements at only one position near the exit.

For the cases with more than one measurement position, two comparisons were performed: (i) an average film thickness h_L from all probes is calculated from both experimental data and numerical simulations; (ii) only the local measured data of the probe farthest from the inlet ($h_{L,i}$) is used for comparisons. In a similar manner to the pressure drop, data from the initial transient is discarded and the 100-130s temporal range is evaluated.

Initially, a grid resolution test of the mean film thickness h_L is performed for representative cases. The results are shown in Figure 7.17. For the I-Kaji-1 configuration, the C_L 1.05 value presents the least accurate solution and worst convergence trend. The momentum flux parameter values of 1.10, 1.20 and the variable C_L models all showed good convergence properties and obtained solutions with errors below 20%.

For the II-Zhao-2 case, C_L 1.05 obtained excellent agreement to experimental data. All methods appear to achieve mesh convergence, however, higher C_L values and the variable models presented higher errors. For the III.ForeDukler-3 case, C_L 1.05 and 1.10 presented errors above 20%, whereas the other models stayed within the 20% margin. Lastly, for the IV-Fershtman-1 configuration, the variable C_L models obtained both good agreement to experimental data and stable mesh convergence.

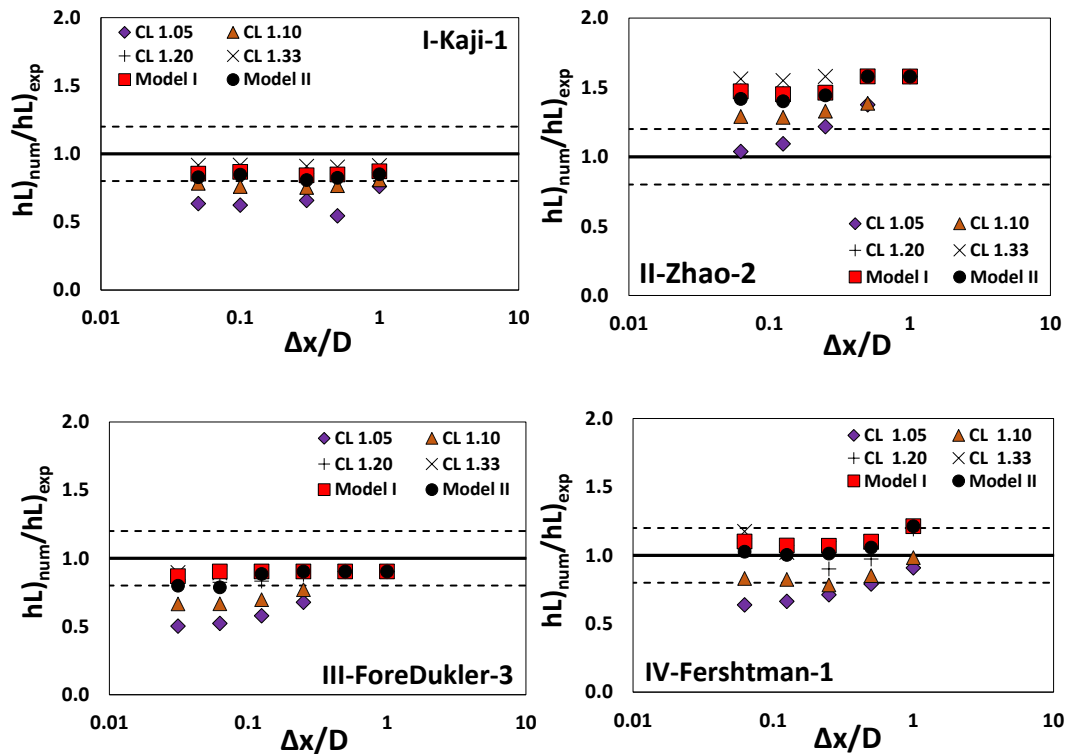


Figure 7.17- Grid resolution tests for mean film thickness normalized by the experimental value. Dashed lines indicate 20% error margins.

Figure 7.18 shows the experimental versus numerical plots for all methods. A visual analysis shows that higher film thickness values are overpredicted by virtually all models. For lower film thickness cases, lower C_L values underpredict the experimental measurements, especially for C_L 1.05. The same analysis was performed for the local film thickness, and results are shown in the Appendix C.

Table 7.4 shows the percentage of cases of the dataset that had prediction errors of liquid film thickness within the 10% error range, for each C_L . Both mean and instantaneous film height data are shown. Again, the variable C_L models have clearly attained better agreement with experimental data, with 33% and 41% of the mean height and local height predictions within the 10% error margin for Model I, and 44% for both mean and local height for Model II. The least accurate model was $C_L = 1.33$, with 18% and 11% of the cases in the 10% range.

The effect of constant C_L values in the mean and local film thickness predictions follows a clear trend. Lower shape factors, i.e., 1.05, tend to underpredict the liquid film height values because the film mass is largely distributed throughout the high amplitude roll waves, which results in a narrow film between wave structures. As the shape factor is increased, e.g., $C_L = 1.10$, the average liquid film increases, and the errors naturally decrease. Stronger damping from constant $C_L > 1.10$ parameters will tend to excessively reduce the wave

amplitudes and promote an overprediction of the average quantities. The non-constant C_L models tackle this issue by introducing a more accurate representation of the velocity and phase fraction distribution, and the damping effect of the shape factor will vary locally. From the data thus far, the proposed models have shown promising improvements to the accuracy of the 1D Two-Fluid Model for annular flows.

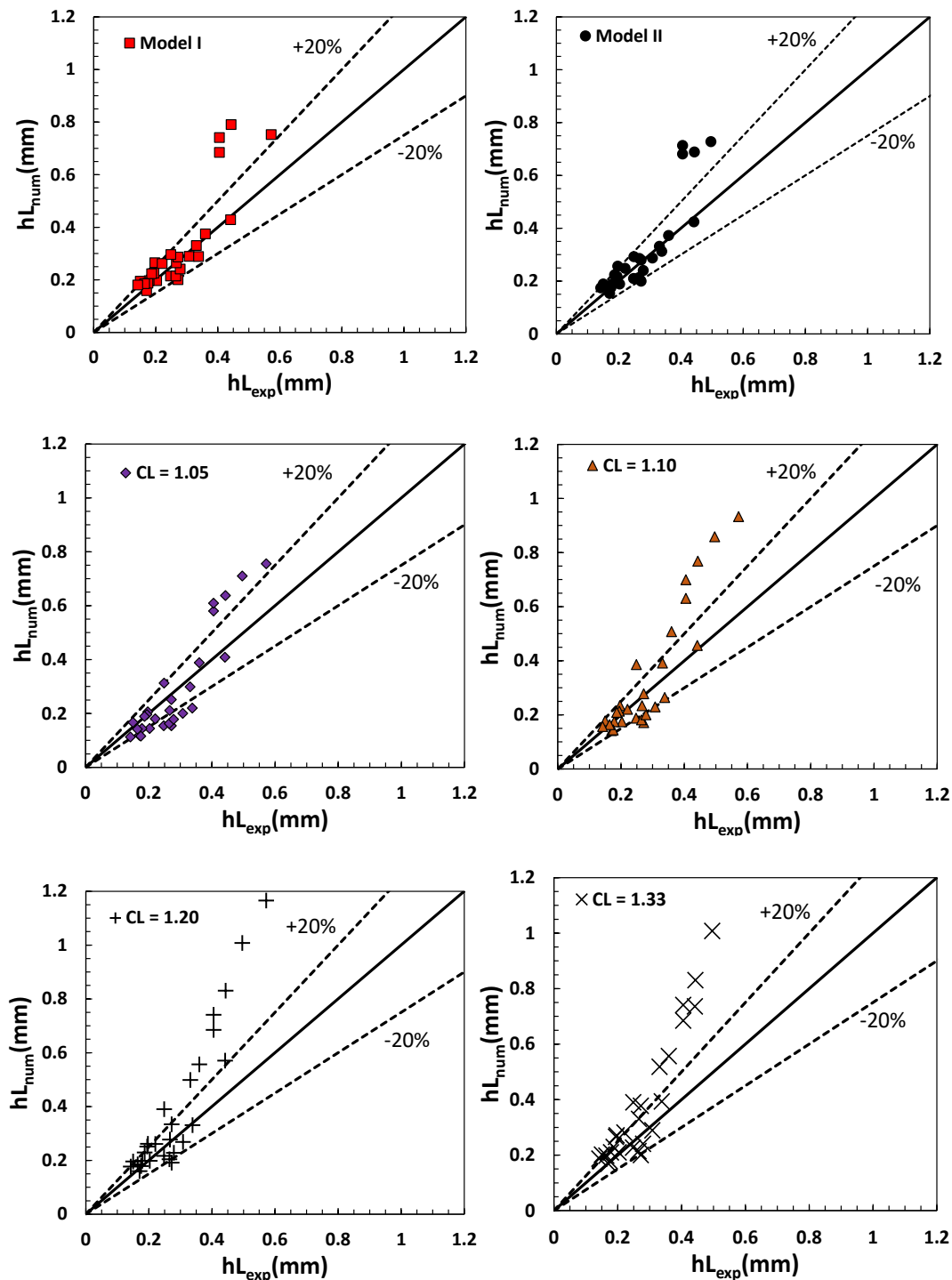


Figure 7.18- Experimental versus Numerical comparisons for mean film thickness.

The influence of increasing the momentum flux parameter in the liquid film thickness prediction can also be compared with the analysis of Fontalvo *et al.* (2020), where a dynamic pressure modelling was included in their study. The best performance was also obtained with $C_L = 1.05$, with 63% of cases within the 20% error bracket. For simulations with $C_L > 1.05$, the accuracy of the model also decreased, with approximately 40% of the cases within the 20% error range. In the present work, the constant $C_L = 1.05$ also presented good agreement with experimental data (54% for local film height), however, a lower discrepancy was obtained when compared to other constant values. As mentioned, the empirical dynamic pressure model may have artificially increased the stabilizing mechanisms of the model, with a direct impact on the wave formation, and consequently in the liquid film thickness.

Table 7.4: Percentage of cases within the 10% error margin for film thickness.

C_L	0-10% Error margin	
	h_L	$h_{L,i}$
1.05	25%	29%
1.10	21%	36%
1.20	18%	18%
1.33	18%	11%
Model I	33%	41%
Model II	44%	44%

From an analysis of Figure 7.18, inaccurate results were obtained for all models with a particular group of experimental cases within the same database, namely the III.ForeDukler-6 to III.ForeDukler-10 configuration. These cases correspond to high superficial liquid Reynolds numbers. To better understand the discrepancies, one can take advantage of the similarity in diameter, fluid properties and superficial velocities of database III and VI, and perform a comparison between the predictions of the models against the two experimental works. Groups with similar superficial Reynolds numbers, i.e., $Re_{sL} = 250$ and 300 , $Re_{sL} = 2000$ and 3000 , were selected from database III and VI, respectively. Additional cases were run for the $Re_{sL} = 250$ configuration of database VI. The comparison is shown in Figure 7.19 for the variable models, and constant C_L values of 1.05 and 1.10. For the lower Re_{sL} , similar results were obtained with the Two-Fluid Model with different C_L values. Visually, the prediction errors do not seem to improve when using one database or the other. However, for the higher Reynolds number, significantly

different results were obtained, where the predictions of database VI were more accurate for all C_L values shown. These results suggest that the experimental values for film thickness of database VI are more precise, due to their use of more modern measuring techniques. From this comparison, the discrepancy obtained in the previous analysis is seen to be caused by the experimental data, and not the numerical model.

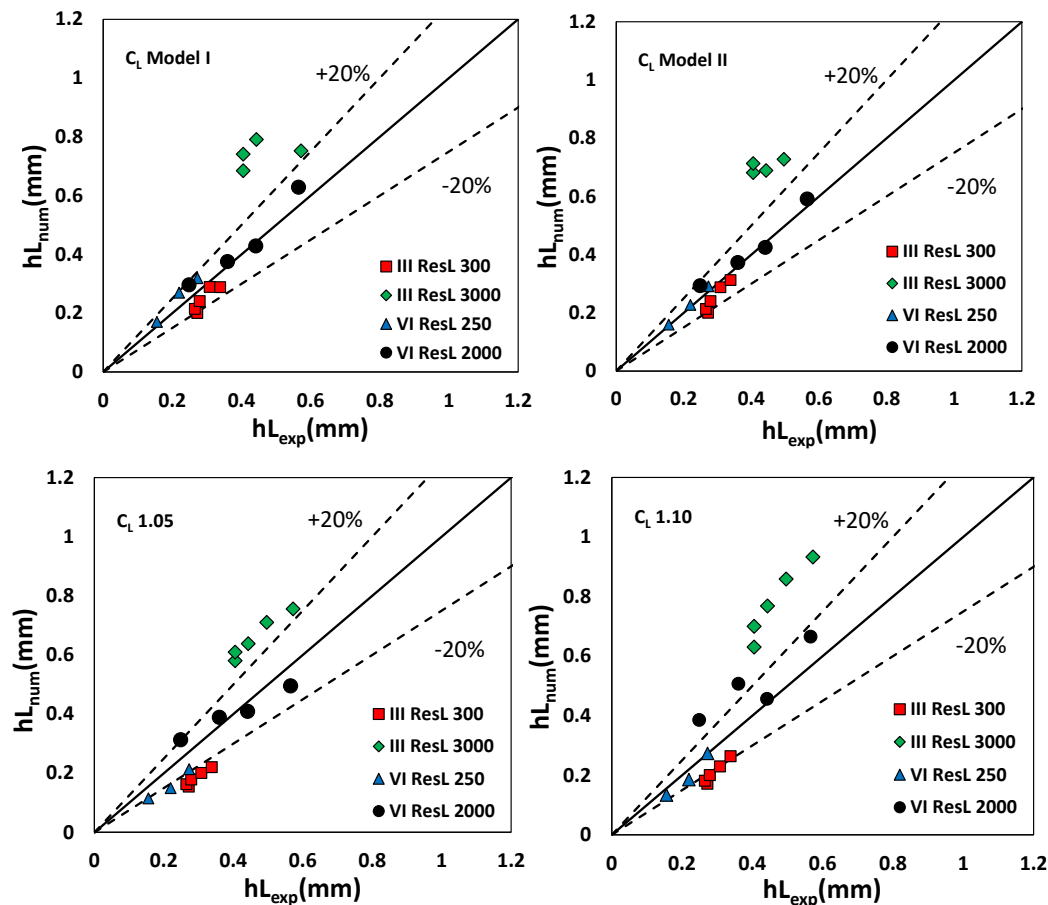


Figure 7.19- Experimental versus Numerical comparisons of databases III and VI for mean film thickness - C_L 1.05, 1.10, Model I and Model II.

The timeseries of the film height for the II-Zhao-2 case are shown in Figure 7.20 and Figure 7.21 at probe locations of $x = 0.62\text{m}$ and $x = 2.00\text{m}$. The configuration of IV-Fershtman-1 also has temporal data for the liquid film height at $x = 7.5\text{m}$ (Figure 7.22).

All C_L models are evaluated in their ability to predict the base liquid film thickness and wave amplitudes in Figure 7.20 and Figure 7.21. The tendency of the measured data is clear, in the first probe ($x = 0.62\text{m}$) the waves are shorter, and the base film is thicker, such that the average film thickness value is relatively high ($h_{L_{exp}} = 0.151\text{mm}$). At the second probe ($x = 2\text{m}$), the waves undergo an increase in amplitude and the base film becomes thinner, which naturally prompts

a decrease in the mean film thickness ($h_{Lexp} = 0.131\text{mm}$). This trend is reasonably predicted by all C_L values and models.

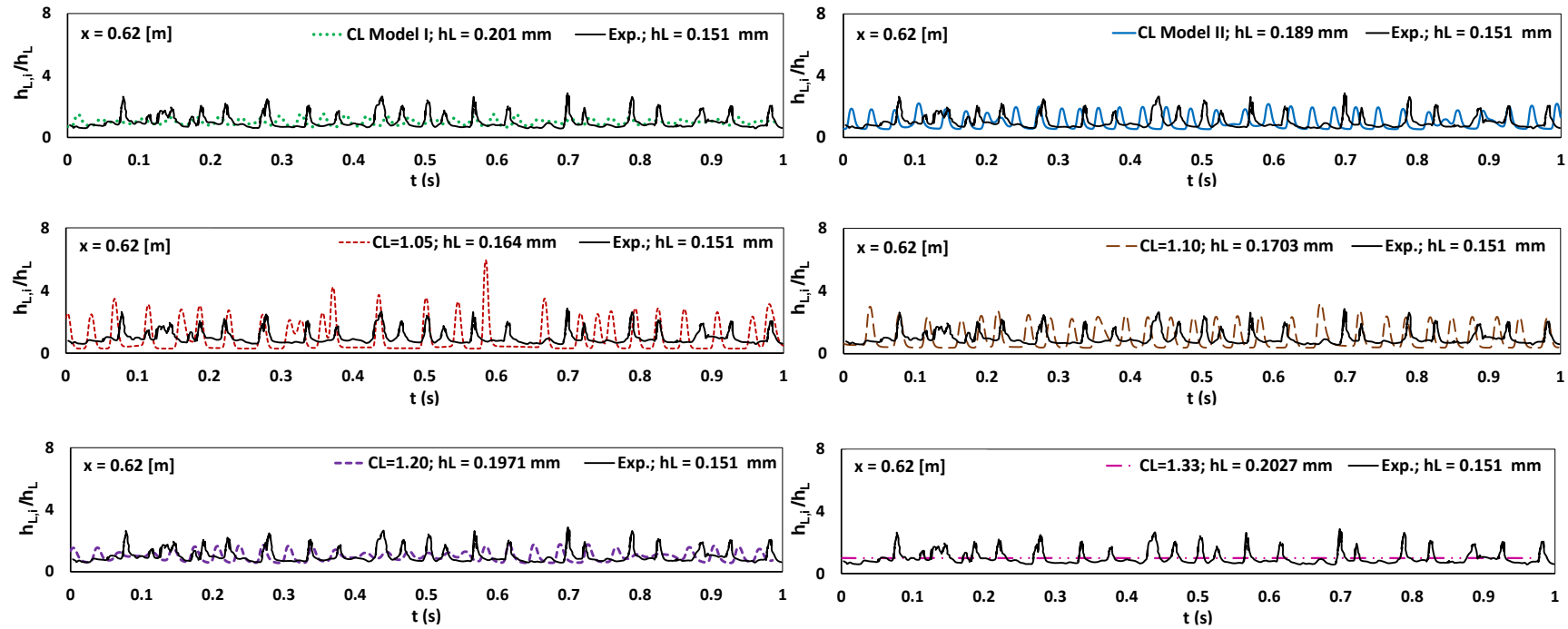


Figure 7.20- Temporal liquid film thickness data at $x = 0.62$ m. II-Zhao-2 case.

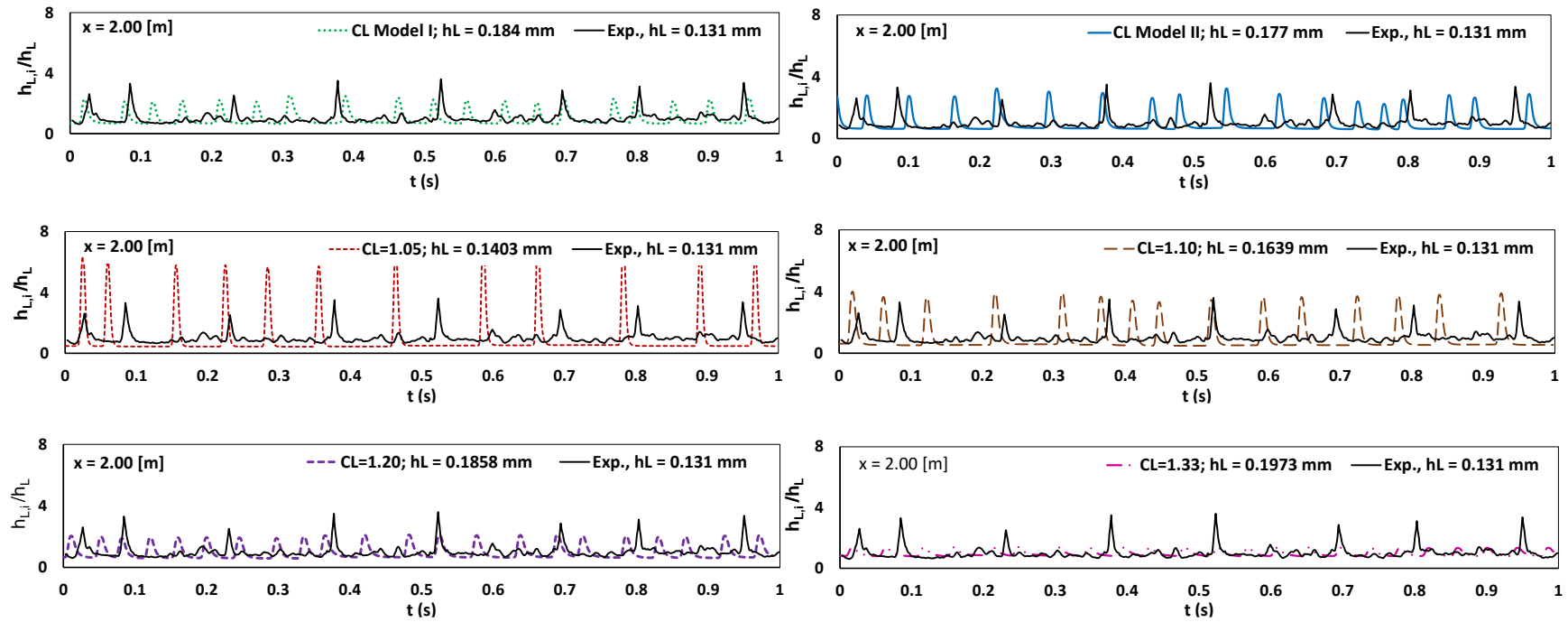


Figure 7.21- Temporal liquid film thickness data at $x = 2.00$ m. II-Zhao-2 case.

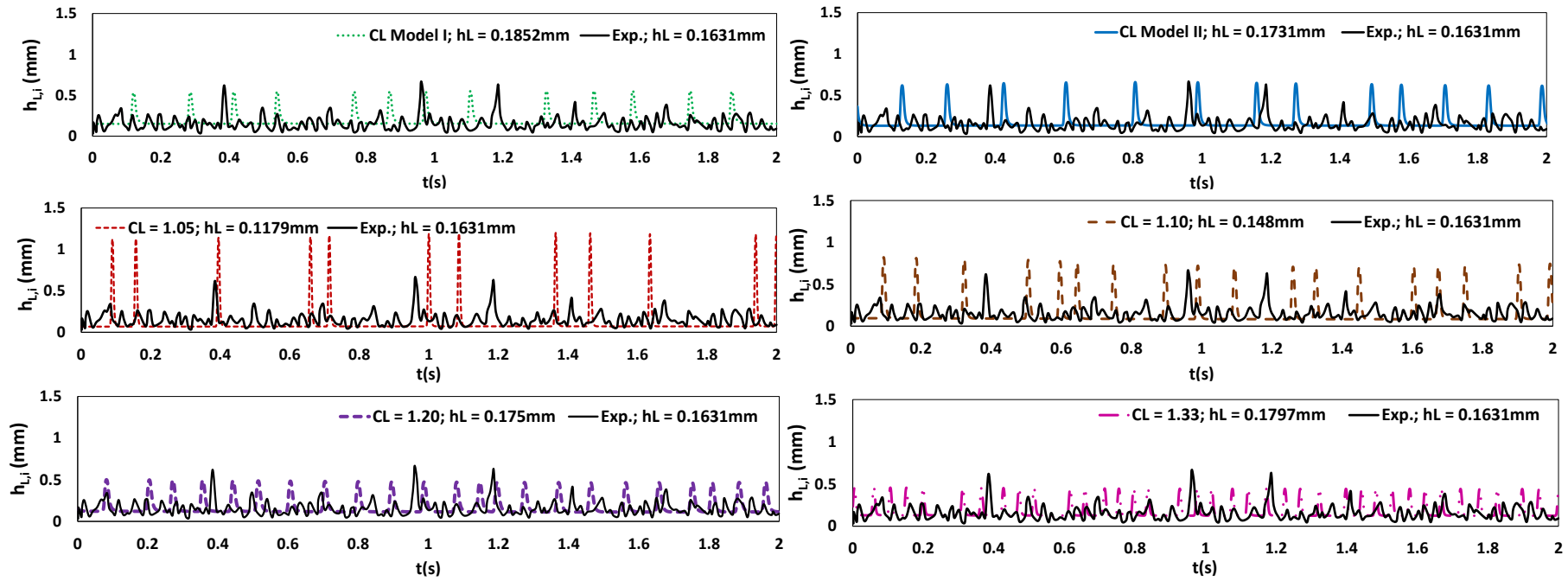


Figure 7.22- Temporal liquid film thickness data at $x = 7.5$ m. IV-Fershtman-1 case.

The use of a constant $C_L = 1.05$ both overpredicts the wave amplitudes and underpredicts the film thickness between waves, particularly for $x = 2\text{m}$. A $C_L = 1.10$ shows a more accurate prediction of wave heights, but slightly underpredicts the base film thickness. Further increase of the C_L value promotes an overdamping of waves, and $C_L = 1.33$ blocks the formation of waves altogether for $x = 0.62\text{m}$ and predicts very short ripple waves at $x = 2\text{m}$. The variable C_L Model I also promotes excessive damping of disturbances, and therefore underpredicts wave amplitudes. Model II, however, obtained the best agreement to experimental data: it showed accurate results for both wave heights and base film thickness, for the two positions.

Figure 7.22 presents the timeseries of the predicted liquid film height with all C_L models, comparing results with the experimental data. A similar trend in the numerical models from the II-Zhao-2 analysis is observed here, where low constant C_L values show a tendency to promote excessively high amplitude waves and very thin films, and an increase in the constant C_L can improve the numerical results up to a certain point. A constant $C_L = 1.10$ shows very good agreement to the experimental curve, and higher C_L values excessively damp the waves. The C_L Model II devised in the present work shows excellent agreement for both wave amplitude and base film thickness.

7.3.5 Frequency

Here, a brief discussion on the frequency spectrum of the film thickness signal is carried out. The configuration of II-Zhao-2 is selected to evaluate the Power Spectral Density (PSD) function of the film height temporal data. The methodology to obtain the PSD spectrum from simulation results is outlined in Appendix B.

Three axial locations were chosen for this test, namely $x = 0.62, 0.92$ and 2m , which are shown in Figure 7.23 for the different C_L models. The overall trend of the experimental energy spectrum is that the peak decreases along the axial direction, whereas the opposite occurs in the numerical PSD data. As suggested in Zhao *et al.* (2013), the decrease in the energy spectrum is due to the coalescence of waves and the entrainment of droplets in the gas core. The entrainment phenomenon is not modeled in the present work, which may partly explain the discrepancies with the simulated data. The wave damping effect of higher C_L values can be clearly seen from the PSD data, where the energy spectrum for the $x = 0.62$ and 0.92m suggest that the onset of waves occurs

farther into the spatial domain. This effect is responsible for the increasing trend of the PSD spectrum, where the spatial amplification of waves induces an increase in energy, which can also be the cause of the inaccurate results of higher shape factor values. C_L 1.05 obtains the closest agreement for the first two positions, but for the last position a C_L of 1.10 obtains the best prediction.

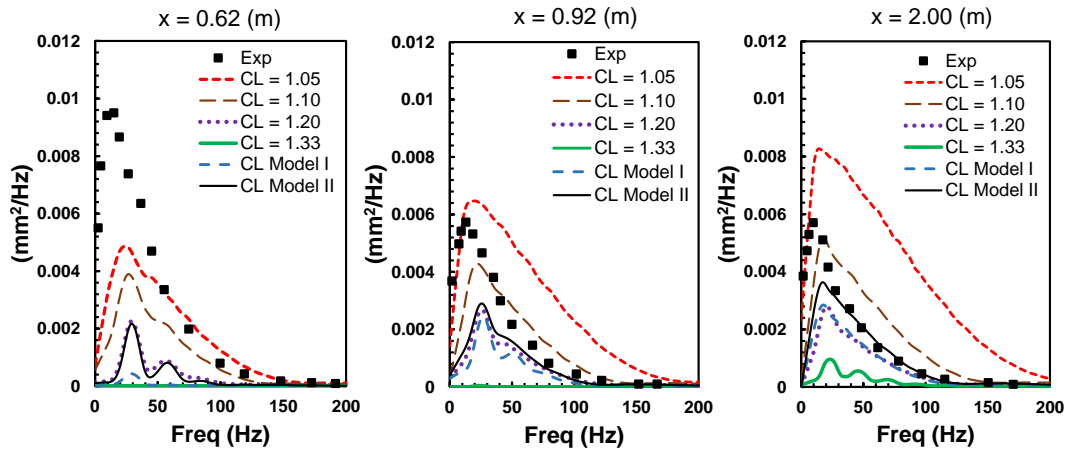


Figure 7.23- Power Spectral Density (PSD) function of the liquid film height timeseries. II-Zhao-2 case.

The numerical results for the dominant frequency ν_{PSD} , i.e., the frequency associated with the peak of the PSD spectrum, agree better to the measured data than the peaks of the PSD spectra. Figure 7.24 shows a comparison between the numerical and experimental dominant frequencies at the different probe locations. All cases show a decrease of the dominant frequency along the pipe. Again, the lower C_L 1.05 value obtains the most adherent result to the measurements, with a slight overprediction of the experimental results but with an agreeing overall trend. Also, an increase of C_L values yields a greater overprediction of the dominant frequency.

While the experimental PSD frequency stabilizes at $x= 1\text{m}$, all numerical predictions show a slower decay, as a reflection of the delayed axial development of waves caused by higher C_L numbers. Experimentally, the waves start forming at the inlet, while numerically, there is a development length from the non-perturbed entrance condition. At the exit probe, all numerical curves still show a developing trend, which suggests that a domain length increase is necessary to obtain a stabilized solution, possibly in better agreement with the experimental PSD spectra. Castello Branco *et al.* (2021) performed domain length tests with the configuration of Zhao *et al.* (2013) to investigate its effect in numerical growth rates at the linear region of the pipe. The actual Zhao *et al.* (2013) configuration pipe length is 2m, Castello Branco *et al.* (2021) have tested pipes with 1, 2 and 4 m,

and they have shown that the numerical growth rates are independent of the domain's length, with perfect agreement in the same region. However, if the flow is not yet stabilized, it might stabilize in a longer pipe. Additional work may be required to investigate if the spatial stabilization of the numerical solution with stronger regularization mechanisms matches the experimental data, given a longer domain. That would shed additional light into the physical soundness of these models.

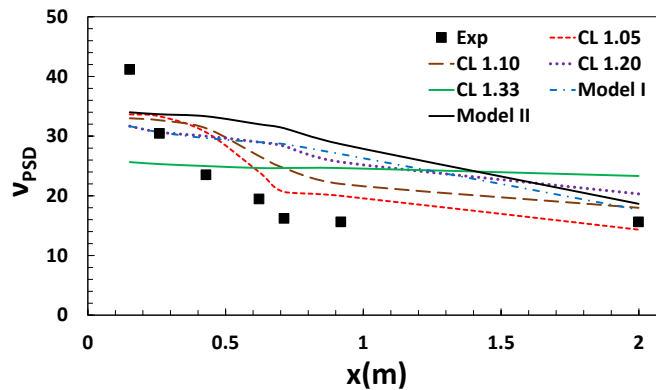


Figure 7.24- Development of the Power Spectral Density (PSD) dominant frequency along the domain. II-Zhao-2 case.

7.3.6 Group velocity

All configurations except the II-Zhao present group velocity data (C_w), obtained from the cross correlation of the timeseries measured at two probes at a certain distance. The numerical group velocity is calculated in a similar manner and is shown in more detail in Appendix B.

The configurations of I-Kaji1, III.ForeDukler-3 and IV-Fershtman-1 were once again selected for the grid resolution tests. Figure 7.25 shows the mesh resolution test for the mean group velocity of all probe positions, where once again the numerical results have been normalized by the experimental value. Results for the I-Kaji-1 configuration show that all models obtain fairly similar predictions, except for the C_L 1.05 value, where a large discrepancy is obtained for $\Delta x/D = 0.25$. For the III.ForeDukler-3 case, the coarser meshes are unable to detect the formation of waves with all C_L values. However, for finer grids, mesh convergence is roughly attained for all models, where Model I, Model II and C_L 1.10 had good agreement with measured data (within the 20% error margin). For the IV-Fershtman-1 case, grid convergence is attained for all models, however, the errors were particularly high. $C_L = 1.05$ obtained slightly better predictions than the other models.

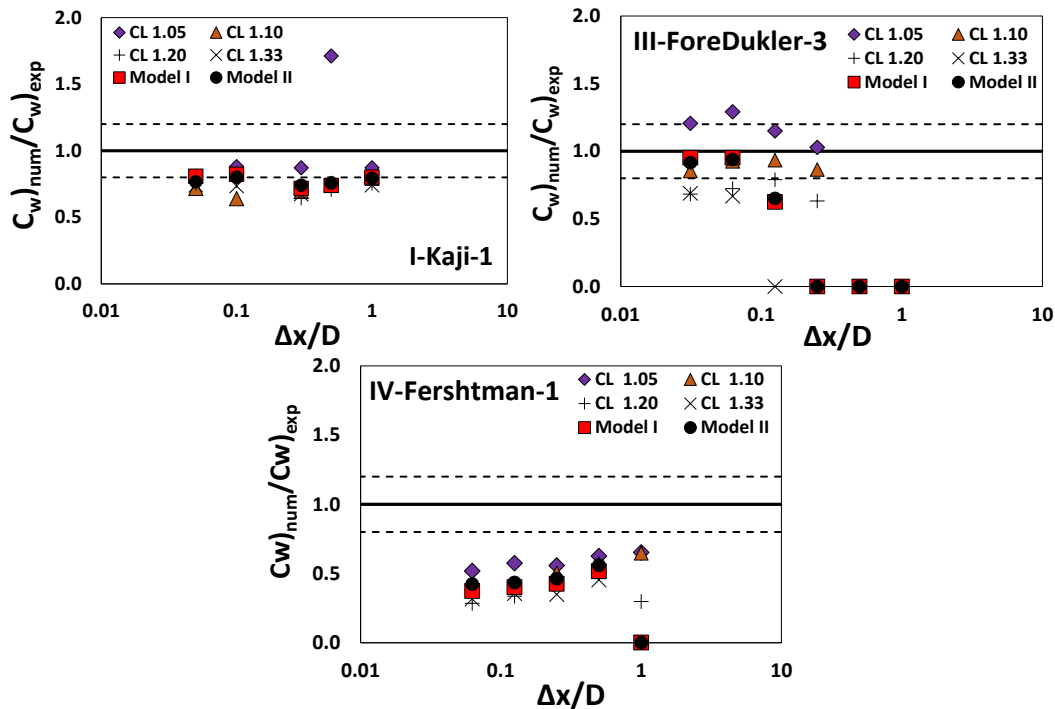


Figure 7.25- Grid resolution tests for group velocity, normalized by the experimental value. Dashed lines indicate 20% error margins.

Figure 7.26 presents the experimental versus numerical plot for the group velocity. The best agreement is clearly obtained with the $C_L = 1.05$, where most of the cases were within the 30% error margins. As has been extensively discussed, the increase of the liquid shape factor introduces higher damping into waves, and smaller waves tend to present lower velocities due to the reduced shear. Thus, all datapoints of group velocity results are naturally underpredicted for higher C_L values in comparison to 1.05. C_L values of 1.20 and 1.33 completely damped the wave formation in some cases, such that the calculated group velocity was zero. Lastly, the variable C_L models obtained inaccurate predictions for most of the cases, with a large spread of data predictions, as can be seen in the figure.

Table 7.5 displays the percentage of cases of the database that had prediction errors within the 30% error range, for each C_L . Clearly, a constant value of 1.05 has obtained highly accurate results in comparison to the other models, where 81% of the cases fell within the margin. However, Model I and II have shown a slight improvement from the higher C_L values of 1.20-1.33.

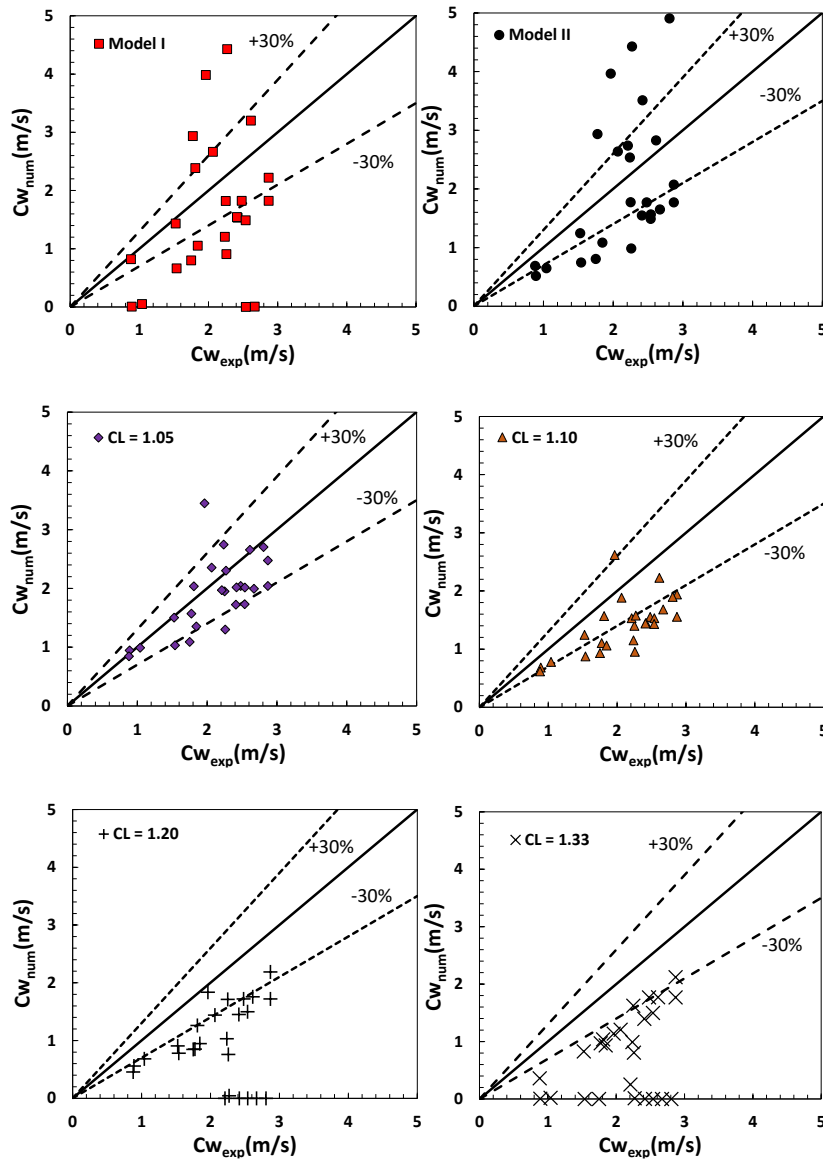


Figure 7.26- Experimental versus numerical graph for Group velocity

Table 7.5: Percentage of cases within the 30% error margin for group velocity.

C_L	0-30% Error margin	
	C_w	
1.05	81%	
1.10	27%	
1.20	12%	
1.33	12%	
Model I	28%	
Model II	36%	

7.3.7 Global evaluation of numerical predictions

The mean errors for pressure gradient, mean film thickness, local film thickness and group velocity are displayed in Table 7.6. For $-dp/dx$, the C_L Models I and II obtained the smallest average error of the set, 9%, followed by C_L 1.10 and 1.20 with 10% errors. For mean and local film thicknesses, Model I and II also presented the smallest errors, with 21% and 20% for Model I and 20% and 16% for Model II. From the constant shape factor values, C_L 1.05 obtained the most accurate results, with 25% and 22% errors. For the group velocity C_w , the constant 1.05 value also performed best, with 17% average error. Model II obtained an average error of 42%, which is satisfactory, considering the performance of the other models. The overall trend shows that the variable C_L models showed consistency in their accuracy, achieving the best prediction for pressure gradients and film thickness, and satisfactory predictions for group velocity with Model II.

Table 7.6: Average error for all quantities.

C_L	Mean Error			
	$-dp/dx$	h_L	$h_{L,i}$	C_w
1.05	13%	25%	22%	19%
1.10	10%	27%	22%	34%
1.20	10%	34%	33%	53%
1.33	13%	40%	41%	64%
Model I	9%	21%	20%	53%
Model II	9%	20%	16%	42%

Furthermore, a combined relative error of pressure drop, local film thickness and group velocity is calculated and shown in Table 7.7. The error is defined as

$$\varepsilon_c = \frac{1}{m} \sum_{j=1}^m \left(n \sqrt{\prod_{i=1}^n \varepsilon_i} \right) \quad (7.7)$$

where ε_i is the relative error of the variable i , n is the number of variables, j represents a case from the database, and m is the total number of cases. From the combined error results, the $C_L = 1.10$ obtained the best results out of the constant value cases. Model I presented a slight improvement in comparison to 1.10, and Model II presented the most accurate solution, with a mean combined error of 14,89%.

Lastly, a simulation time test is carried out to determine the additional computational cost of the C_L calculations of the proposed models. The simulations were run on an Intel Core i9-10900F 2.80GHz machine with 16 GB of RAM. A C_L test of the II-Zhao-2 configuration with a mesh refinement level of $\Delta x/D = 0.25$ was selected. Table 7.8 shows the simulation time for each case, and the relative runtime in comparison to the $C_L = 1.05$ case. The results show that a similar runtime was obtained for all cases, where the increase in C_L number yields faster simulations. This effect is due to the stabilizing nature of the momentum flux parameter, which results in the need for fewer iterations to achieve convergence within a timestep. The proposed models naturally require more computational power to perform the additional calculations, but since the solutions are more stable than with a low C_L number, the increase in simulation time is not as high. Although Model II obtained the highest simulation time, there was only a 3% increase in comparison to the $C_L = 1.05$ and Model I presented a 2% reduction from the 1.05 run. Overall, the differences in simulation time were not significant.

Table 7.7: Combined error.

C_L	ϵ_c
1.05	17.96%
1.10	17.61%
1.20	22.02%
1.33	26.97%
Model I	17.52%
Model II	14.89%

Table 7.8: Simulation time test.

C_L	Simulation time (s)	Relative runtime
1.05	4416	1
1.10	4250	0.9624
1.20	4213	0.9541
Model I	4330	0.9805
Model II	4560	1.0326

8 CONCLUSION

The present work evaluated the hydrodynamic stability properties of commonly employed closure relations for vertical annular flows with the 1D Two-Fluid Model. Differential and discrete stability analyses were carried out to evaluate the mathematical and discretized system of equations. The closure relations were evaluated through their differential and discrete growth rate curves in the frequency (or wavelength) spectrum. Mesh refinements of $\Delta x/D = 1$ to 0.015625 were selected to generate the discrete dispersion relation curves. The stability analysis results showed that closure models such as the interface pressure jump, the dynamic pressure model and the momentum flux parameter worked to stabilize the flow and ensure the hyperbolicity of the system of equations.

The pressure jump introduces a cut-off frequency above which no growth rates are present. Thus, it promptly regularizes the system, and the unbounded growth of perturbations, characteristic of the standard model, is blocked. In this case, mesh refinement can be attained. The surface tension term, however, does not provide any meaningful damping of perturbations for the majority of the configurations analyzed. Additional regularization mechanisms are then required to ensure that mesh convergence can be attained at practical grid resolutions.

Three interfacial friction factor correlations and three liquid film models were assessed. Results from the LST were inconclusive as no significant effect was observed in the growth rates by varying the f_i and U_i models.

Three dynamic pressure models were evaluated through LST. Results have shown that the addition of any dynamic pressure formulation works to stabilize the flow, introducing a small amount of damping into the growth rate curves. However, no meaningful change in the hyperbolicity of the system has been observed in a stability sense for Models ΔP_{dyn_I} and $\Delta P_{dyn_{III}}$. For the representative case of II-Zhao-2, the second dynamic pressure model $\Delta P_{dyn_{II}}$ was able to introduce a growth rate plateau, which regularizes the flow. However, the level of mesh refinement required to achieve convergence is prohibitively high.

Four constant momentum flux parameter values (1.05 through 1.33) and two proposed models were tested in this work. The momentum flux parameter has proved to be a very important tool in regularizing the system, where values above

1.10 managed to introduce appropriate regularization of the flow by introducing a plateau at low growth rate values. The use of models that depend on local flow quantities proved to also be very effective in blocking unbounded growth of disturbances. However, the stability analysis results are restricted to the linear region, and further assessment were carried out in terms of the nonlinear behavior of the C_L models. It can be concluded from the LST results that the analyzed closure models had positive effects in ensuring the hyperbolicity of the 1D Two-Fluid Model. The combined used of the closure relations must be done with caution to ensure the physical soundness and appropriate stability properties.

The variable C_L models were evaluated numerically against an extensive database composed of experimental works from the literature. Statistical quantities of pressure gradient, liquid film thickness and group velocity were used, when available. Rigorous grid resolution tests for a representative subset of configurations were carried out, and an experimental versus numerical comparison was performed for the entire dataset. Mesh refinements of $\Delta x/D = 1$ to 0.0625 were selected to compose the grid test. Results have shown that all momentum flux parameter models obtained good mesh convergence properties. The proposed Models I and II showed improvements on pressure gradient and film thickness data but underperformed against $C_L = 1.05$ on the group velocity tests. However, reasonable agreement was obtained for Model II. It can be concluded that the proposed models have improved the predictions of the 1D Two Fluid Model and showed consistency in accuracy across the database.

Further studies must be carried out to shed light into the missing physics in the modeling, aiming to improve the predictions of group velocity and frequencies. The database should also be expanded to include experimental works with larger diameters, higher (and lower) superficial velocities. In cases of higher gas and liquid superficial velocities, the impact of the entrainment of droplets in the gas core must be modeled.

The effect of entrainment on the gas velocity profile and turbulence is also significant, as has been shown in works from the literature. Further, a small increase in the shape factor has proved to have a profound impact on the flow for the liquid phase. Therefore, the development of a model for the gas momentum flux parameter must be a goal for future studies. Turbulence modelling may also be a promising addition to the 1D model.

Additionally, the C_L models must be further developed to contemplate the flow reversal effect that occurs in the liquid loading phenomenon, where the velocity profile undergoes complex changes.

Another future improvement to the present model is to implement a periodic domain. It is a promising alternative to the use of refined meshes in longer pipes, where the computational cost might be prohibitive, especially for analyzing the impact of closure models on wave stability properties.

References

ALEKSEENKO, S., CHERDANTSEV, A.V., KHARLAMOV, S., MARKOVICH, D., 2009. Two-wave structure of liquid film and wave interrelation in annular gas-liquid flow with and without entrainment. *Physics of Fluids* 21, 061701. Doi:10.1063/1.3151999

ALEKSEENKO, S., CHERDANTSEV, A.V., HEINZ, O., KHARLAMOV, S., MARKOVICH, D., 2013. Analysis of spatial and temporal spectra of liquid film surface in annular gas-liquid flow. *Experiments in Fluids* 54, 1590. Doi: 10.1007/s00348-013-1590-7.

ALEKSEENKO, S., CHERDANTSEV, A.V., CHERDANTSEV, M.V., ISAENKOV, S.V., MARKOVICH, D.M., 2015. Study of formation and development of disturbance waves in annular gas-liquid flow. *International Journal of Multiphase Flow* 77, 65-75. Doi: .10.1016/j.ijmultiphaseflow.2015.08.007.

ALIYU, A.M., BABA, Y.D., LIAO, L., YEUNG, H., KIM, K.C., 2017. Interfacial friction in upward annular gas-liquid two-phase flow in pipes. *Experimental Thermal and Fluid Science* 84, 90-109. Doi: 10.1016/j.expthermflusci.2017.02.006

ALVES, M. V. C., BARBOSA JR, J., FALCONE, G., 2012. Modeling the transient behavior of churn-annular flow in a vertical pipe. In: 3rd Brazilian Conference on Boiling, Condensation and Multiphase flow, vol. 400.

ALVES, M.V.C., 2014. Modelagem numérica do escoamento transiente churn-annular em tubulações verticais e sua aplicação na simulação de carga de líquido em poços de gás. D.Sc. thesis, Federal University of Santa Catarina.

ALVES, M.V.C., WALTRICH, P.J., GESSNER, T.R., FALCONE, G., BARBOSA JR., J.R., 2017. Modeling transient churn-annular flows in a long vertical tube. *International Journal of Multiphase Flow* 89, 399-412. Doi: 10.1016/j.ijmultiphaseflow.2016.12.001.

ASHWOOD, A.C., VANDEN HOGEN, S.J., RODARTE, M.A., KOPPLIN, C.R., RODRÍGUEZ, D.J., HURLBURT, E.T., SHEDD, T.A., 2015. A multiphase, micro-scale PIV measurement technique for liquid film velocity measurements in annular two-phase flow. *International Journal of Multiphase Flow* 68, 27-39. Doi:

10.1016/j.ijmultiphaseflow.2014.09.003.

AZZOPARDI, B.J., 1986. Disturbance wave frequencies, velocities and spacing in vertical annular two-phase flow. *Nuclear Engineering Design* 92, 121–133.

AZZOPARDI, B.J., TEIXEIRA, J.C.F., 1994. Detailed Measurements of Vertical Annular Two-Phase Flow—Part I: Drop Velocities and Sizes. *Journal of Fluids Engineering* 116, 792. Doi: 10.1115/1.2911851

AZZOPARDI, B.J., 1997. Drops in annular two-phase flow. *International Journal of Multiphase Flow* 23, 1-53. Doi: 10.1016/S0301-9322(97)90087-2

BADIE, S., HALE, C.P., LAWRENCE, C.J., HEWITT, G.F., 2000. Pressure gradient and holdup in horizontal two-phase gas-liquid flows with low liquid loading. *International Journal of Multiphase Flow* 26, 1525-1543. Doi: 10.1016/S0301-9322(99)00102-0.

BANERJEE, S., CHAN, A.M.C., 1980. Separate flow models – I Analysis of the averaged and local instantaneous formulations. *International journal of multiphase flow*, 6, 1-24. Doi: 10.1016/0301-9322(80)90036-1

BARBEAU, S., 2008. Improved Models for Transient One-dimensional Simulations of Multiphase Slug Flows. PhD thesis, Mech. Eng. Dept., Imperial College London.

BARNEA, D. TAITEL, Y., 1988. Transient-formulation modes and stability of steady-state annular flow. *Chemical Engineering Science* 44(2), 325-332.

BARNEA, D., 1991. On the effect of viscosity on stability of stratified gas—liquid flow—application to flow pattern transition at various pipe inclinations. *Chemical Engineering Science* 46(8), 2123-2131. Doi:10.1016/0009-2509(91)80170-4.

BARNEA, D. TAITEL, Y., 1993. Kelvin-Helmholtz stability criteria for stratified flow: viscous versus non-viscous (inviscid) approaches. *International journal of multiphase flow*, 19(4), 639–649, doi:10.1016/0301-9322(93)90092-9.

BELT, R. F., 2007. On the liquid film in inclined annular flow. Ph.D. Thesis, Institut National Polytechnique de Lorraine.

BELT, R.J., VAN'T WESTENDE, J.M.C., PRASSER, H.M., PORTELA, L.M., 2009. Prediction of the interfacial shear-stress in vertical annular flow. *International Journal of Multiphase Flow* 35, 689–697. doi: 10.1016/j.ijmultiphaseflow.2008.12.003.

BELT, R.J., VAN'T WESTENDE, J.M.C., PRASSER, H.M., PORTELA, L.M., 2010.

Time and spatially resolved measurements of interfacial waves in vertical annular flow. *International Journal of Multiphase Flow* 36, 570–587. Doi: 10.1016/j.ijmultiphaseflow.2010.03.004.

BENDIKSEN, K.H., 1984. An experimental investigation of the motion of long bubbles in inclined tubes. *International Journal of Multiphase Flow* 10(4), 467–483. Doi: 10.1016/0301-9322(84)90057-0.

BENDIKSEN, K.H., MALNES, D., MOE, R., NULAND, S., 1991. The dynamic two-fluid model OLGA: theory and application. *SPE Production Engineering* 6(2), 171–180. Doi: <https://doi.org/10.2118/19451-PA>.

BERNA, C., ESCRIVÁ, A., MUÑOZ-COBO, J., HERRANZ, L., 2014. Review of droplet entrainment in annular flow: interfacial waves and onset of entrainment. *Progress in Nuclear Energy*. 74, 14–43. doi: 10.1016/j.pnucene.2014.01.018.

BESTION, D., 1990. The physical closure laws in the CATHARE code. *Nuclear Engineering and Design*, vol. 124, n. 3, p. 229-245. Doi: 10.1016/0029-5493(90)90294-8

BIBERG, D., 2007. A mathematical model for two-phase stratified turbulent duct flow. *Multiphase Science and Technology* 19(1), 1-48. Doi:10.1615/MultScienTechn.v19.i1.10

BONIZZI, M., ISSA, R.I., 2003. A model for simulating gas bubble entrainment in two-phase horizontal slug flow. *International Journal of Multiphase Flow* 29(11), 1685-1717. Doi: 10.1016/j.ijmultiphaseflow.2003.09.001.

BONIZZI, M., 2003. Transient one-dimensional modelling of multiphase slug flows. Ph.D. thesis, Imperial College, London.

BONNIZI, M., ANDREUSSI, P. & BANERJEE, S., 2009. Flow regime independent, high resolution multi-field modelling of near-horizontal gas liquid flows in pipelines. *Int. J. Multiphase Flow* 35(1), 34–46. doi: 10.1016/j.ijmultiphaseflow.2008.09.001.

BONZANINI, A., PICCHI, D., FERRARIC, M., POESIO, P., 2019. Velocity profiles description and shape factors inclusion in a hyperbolic, one-dimensional, transient two-fluid model for stratified and slug flow simulations in pipes. *Petroleum* 5(2), 191–198. doi:10.1016/j.petlm.2018.03.005

BRENNEN, C., 2005. *Fundamentals of Multiphase Flow*. Pasadena, CA: Cambridge University Press, Inc.

CARNEIRO, J.N.E., 2006. Simulação Numérica de Escoamentos Bifásicos no Regime de Golfadas em Tubulações Horizontais e Levemente Inclinadas. M.Sc. Dissertation, PUC-Rio, Brazil.

CARNEIRO, J.N.E., FONSECA JR., R., ORTEGA, A.J., CHUCUYA, R.C., NIECKELE, A.O., AZEVEDO, L.F.A., 2011. Statistical characterization of two-phase slug flow in a horizontal pipe. *Journal of the Brazilian Society of Mechanical Sciences and Engineering* 33, 251-258. doi:10.1590/S1678-58782011000500007

CASTELLO BRANCO, R.L.; FONTALVO, E.M.G., DE PAULA, I.B., CARNEIRO, J.N.E., NIECKELE, A.O., 2021. Stability analysis of vertical annular flows with the 1D Two-Fluid Model: effect of closure relations on wave characteristics. *Int. J. Multiphase Flow* 103947. Doi: 10.1016/j.ijmultiphaseflow.2021.103947.

CHU, K.J., DUKLER, A.E., 1974. Statistical characteristics of thin, wavy films: Part II. Studies of the substrate and its wave structure. *AIChE Journal* 20(4), 695-706. Doi: 10.1002/aic.690200410.

CIONCOLINI, A., DEL COL, D., THOME, J.R., 2015. An indirect criterion for the laminar to turbulent flow transition in shear-driven annular liquid films. *International Journal of Multiphase Flow* 75, 26-38. Doi: 10.1016/j.ijmultiphaseflow.2015.05.002.

DANIELSON, T.J., BANSAL, K.M., HANSEN, R., LEPORCHER, E., 2005. LEDA: The Next Multiphase Flow Performance Simulator. In: 12th International Conference on Multiphase Production Technology, Barcelona, Spain, May 2005.

DOBRAN, F., 1983. Hydrodynamic and heat transfer analysis of two-phase annular flow with a new liquid film model of turbulence. *Int. J. Heat Mass Transfer* 26(8), 1159-1171. Doi:10.1016/S0017-9310(83)80170-7.

DRAZIN, P.G., 2002. *Introduction to Hydrodynamic Stability*. Cambridge University Press, Cambridge. Doi: 10.1017/CBO9780511809064

DUKLER, A.E., HUBBARD, M.G., 1975. A model for gas-liquid slug flow in horizontal and near horizontal tubes. *Ind. Eng. Chem. Fundam.* 14, 337. Doi: 10.1021/i160056a011

EMAMZADEH, M., ISSA, R.I., 2013b. A model for predicting the transition between stratified and annular flow in horizontal pipes. *Multiphase Science and Technology* 25, 79-100.

FAN, W., LI, H., ANGLART, H., 2019. Numerical investigation of spatial and temporal structure of annular flow with disturbance waves. *International Journal of*

Multiphase Flow 110, 256-272. Doi: 10.1016/j.ijmultiphaseflow.2018.10.003.

FAN, W., CHERDANTSEV, A.V., ANGLART, H., 2020. Experimental and numerical study of formation and development of disturbance waves in annular gas-liquid flow. Energy 207, 118309. Doi:10.1016/j.energy.2020.118309.

FERRARI, M., BONZANINI, A., POESIO, P., 2017. A five-equation, transient, hyperbolic, one-dimensional model for slug capturing in pipes. International Journal for Numerical Methods in Fluids 85, 327-362. doi:10.1002/flid.4387.

FERSHTMAN, A., ROBERS, L., PRASSER, H., BARNEA, D., SHEMER, L., 2020. Interfacial structure of upward gas-liquid annular flow in inclined pipes. International Journal of Multiphase Flow 132, 103437. doi: 10.1016/j.ijmultiphaseflow.2020.103437.

FONTALVO, E.M.G., 2016. Avaliação da Pressão Dinâmica no Modelo de Dois Fluidos Unidimensional Aplicado ao escoamento Anular Vertical. M.Sc. Dissertation, PUC-Rio, Brazil.

FONTALVO, E.M.G., NIECKELE, A.O., CARNEIRO, J.N.E., 2016. Assessment of the dynamic pressure effect in 1D Two-Fluid Model for a vertical annular gas-liquid flow. In: 16th Brazilian Congress of Thermal Sciences and Engineering, Vitória, Brazil, 7-10 Nov.

FONTALVO, E.M.G., BRANCO, R.L.C., CARNEIRO, J.N.E., NIECKELE, A.O. 2020. Assessment of closure relations on the numerical predictions of vertical annular flows with the Two-Fluid Model. Int. J. Multiphase Flow 126, 103243 (19 pages). doi: 10.1016/j.ijmultiphaseflow.2020.103243.

FORE, L.B., DUKLER, A.E., 1995. Droplet deposition and momentum transfer in annular flow. AIChE J. 41(9), 2040-2046. doi:10.1002/aic.690410904.

FORE, L.B., BEUS, S.G., BAUER, R.C., 2000. Interfacial friction in gas-liquid annular flow: analogies to full and transition roughness. International Journal of Multiphase Flow 26, 1755-1769. Doi:10.1016/S0301-9322(99)00114-7.

FOWLER, A.; LISSETER, P., 1992. Flooding and flow reversal in annular two-phase flows. SIAM J. App. Mathematics, 52(1), 15-33. doi:10.1137/0152002

FULLMER, W.D., RANSOM, V. H., BERTODANO, M. A. L., 2014. Linear and nonlinear analysis of an unstable, but well-posed, one-dimensional Two-Fluid Model for two-phase flow based on the inviscid Kelvin-Helmholtz instability. Nuclear Eng. and Design 268, 173-184. doi: 10.1016/j.nucengdes.2013.04.043.

GALLEN, F., ISSA, R.I., 2015. Linear stability analysis of the discretized one-dimensional Two-Fluid Model equations for slug capturing in vertical flow. *Multiphase Sc. Tech.* 27 (2–4), 215–227. doi:10.1615/MultScienTechn.v27.i2-4.80.

GASTER, M., 1962. A note on the relation between temporally-increasing and spatially-increasing disturbances in hydrodynamic stability. *Journal of Fluid Mechanics*, 14(2), 222–224. doi:10.1017/S0022112062001184

GILL, L.E., HEWITT, G.F., HITCHON, J.W., LACEY, P.M.C., 1964. Sampling probe studies of the gas core in annular two-phase flow— Studies of the effect of phase flow rates on phase and velocity distribution. *Chem. Eng. Sci.* 19, 665– 682.

HADAMARD, J., 1902. On the problem of partial derivatives and their physical significance. *Princeton University Bulletin*, 13(4), 49-52.

HALL TAYLOR, N.S., HEWITT, I.J., LACEY, P.M.C., 1963. The motion and frequency of large disturbance waves in annular two-phase flow of air-water mixtures. *Chemical Engineering Science* 18, 537-552. Doi:10.1016/0009-2509(63)85014-9.

HALL TAYLOR, N.S., HEWITT, I.J., OCKENDON, J.R., WITELSKI, T.P., 2014. A new model for disturbance waves. *Int. J. Multiphase Flow* 66, 38-45. doi: 10.1016/j.ijmultiphaseflow.2014.06.004

HAN, H., GABRIEL, K., 2007. A Numerical Study of Entrainment Mechanism in Axisymmetric Annular Gas-Liquid Flow. *J. Fluids Eng.* 129(3), 293-301. Doi: 10.1115/1.2427078.

HAN, P., GUO, L., 2015. Numerical simulation of terrain-induced severe slugging coupled by hydrodynamic slugs in a pipeline-riser system. *International Journal of Heat and Fluid Flow* 56, 355-366. Doi: 1016/j.ijheatfluidflow.2015.10.005

HAZUKU, T., TAKAMASA, T., MATSUMOTO, Y., 2008. Experimental study on axial development of liquid film in vertical upward annular two-phase flow. *International Journal of Multiphase Flow* 34, 111–127. doi: 10.1016/j.ijmultiphaseflow.2007.10.008

HEWITT, G.F., JAYANTI, S., HOPE, C.B., 1990. Structure of thin liquid films in gas-liquid horizontal flow. *International Journal of Multiphase Flow* 16(6), 951-957. Doi: 10.1016/0301-9322(90)90100-W.

HEWITT, G.F., NICHOLS, B., 1969. Film thickness measurement in annular two-phase flow using a fluorescence spectrometer technique. Part II. Studies of the

shape of disturbance waves. UKAEA Report AERE-R 4506.

HIRT, C.W., NICHOLS, B.D., 1981. Volume of Fluid (VOF) Method for the Dynamics of Free Boundaries. *Journal of Computational Physics*, 39, 201-225. Doi: 10.1016/0021-9991(81)90145-5

INÁCIO, J.R.G., CARNEIRO, J.N.E., NIECKELE, A.O., 2012. Investigation of closure relations for 1D-Two Fluid model in vertical pipes. In: 14th Brazilian Congress of Thermal Sciences and Engineering, Rio de Janeiro, RJ, Brazil, November 18-22.

INADA, F., DREW, D.A., LAHEY JR., R.T., 2004. An analytical study on interfacial wave structure between the liquid film and gas core in a vertical tube. *Int. J. Multiphase Flow* 30, 827–851. doi: 10.1016/j.ijmultiphaseflow.2004.03.002

ISHII, M., 1975. Thermo-fluid dynamic theory of two-phase flow. NASA STI/Recon Technical Report A, 75, 29657.

ISHII, M., GROLMES, M., 1975. Inception criteria for droplet entrainment in two-phase concurrent film flow. *AIChE Journal*, 21(2), 308–318.

ISHII, M., HIBIKI, T., 2011. *Thermo-Fluid Dynamics of Two-Phase Flow*, Springer Sc, USA.

ISHII, M., MISHIMA, K., 1984. Two-fluid model and hydrodynamic constitutive relations. *Nuclear Engineering and Design*, 82(2), 107-126. Doi: 10.1016/0029-5493(84)90207-3

ISSA, R. I.; GALLEN, F., 2015. Mechanistic simulation of slug flow in vertical pipes using the one-dimensional Two–Fluid Model. *Multiphase Sc. Tech.*, 27(2–4), 229–245. doi:10.1615/MultScienTechn.v27.i2-4.90

ISSA, R.; KEMPF, M., 2003. Simulation of slug flow in horizontal and nearly horizontal pipes with the Two–Fluid Model. *Int. J. Multiphase Flow*, 29(1), 69–95. doi:10.1016/S0301-9322(02)00127-1.

ISSA, R.I., MONTINI, M., 2010. Applicability of the momentum–flux–parameter closure for Two–Fluid Model to slug flow. In: *Proc. 6th Int. Symp. Multiphase Flow, Heat Mass Transfer and Energy Conversion*. AIP, 712–722. doi:10.1063/1.3366452.

JU, P., LIU, Y., BROOKS, C.S., ISHII, M., 2019. Prediction of interfacial shear stress of vertical upward adiabatic annular flow in pipes. *International Journal of*

Heat and Mass Transfer 133, 500-509. Doi: 10.1016/j.ijheatmasstransfer.2018.12.057.

KAJI, R., 2008. Characteristics of two-phase flow structures and transitions in vertical upward flow. Ph.D. Thesis, University of Nottingham.

KORDYBAN, E. S. & RANOV, T., 1970. Mechanism of slug formation in horizontal two-phase flow. J. Basic Eng. 92(4), 857-864. Doi:10.1115/1.3425157.

KOSKY, P. G.; Staub, F. W., 1971. Local condensing heat transfer coefficients in the annular flow regime, AIChE J., 17(5), 1037–1943. doi:10.1002/aic.690170505

KUMAR, P., DAS, A.K., MITRA, S.K., 2016. Physical understanding of gas-liquid annular flow and its transition to dispersed droplets. Physics of Fluids 28, 072101. doi: 10.1063/1.4954999

KUSHNIR, R.; SEGAL, V.; ULLMAN, A.; BRAUNER, N., 2017. Closure relations effects on the prediction of the stratified two-phase flow stability via the two-fluid model. Int. J. Multiphase Flow 97, 78–93. doi: 10.1016/j.ijmultiphaseflow.2017.07.010

LIAO, J., MEI, R., KLAUSNER, J.F., 2008. A study on the numerical stability of the two-fluid model near ill-posedness. Int. J. Multiphase Flow 34, 1067–1087. doi:10.1016/j.ijmultiphaseflow.2008.02.010.

LINÉ, A., BELT, R., MUNOZ, J.M., ALLAIN, O., GUEGAN, D., 2013. Data processing of full 3D numerical simulation of slug flow to improve Unit Cell Model. In: 16th International Conference on Multiphase Production Technology, Cannes, France, 12-14 June.

LEPORINI, M., BONZANINI, A., FERRARI, M., POESIO, P., 2021. The extension of the one-dimensional two-fluid slug capturing method to simulate slug flow in vertical pipes. International Journal of Numerical Methods in Fluids 93, 816–833. Doi:10.1002/fld.4909.

MALISKA, C.R., 1981. A Solution Method for Three-Dimensional Parabolic Fluid Flows Problems in Nonorthogonal Coordinates. Ph.D. Thesis, University of Waterloo, Waterloo.

MICAELLI, J.C., 1987. CATHARE An advanced best-estimate code for PWR safety analysis. SETH/LEML-EM/87-58.

MILNE-THOMSON, L.M., 1968. Theoretical Hydrodynamics. 5th Edition, Dover

Publications, New York

MOECK, E.O., 1970. Annular-dispersed two-phase flow and critical heat flux. Atomic Energy Canada Limited AECL-3656, 337–346.

MONTINI, M., 2011. Closure relations of the one-dimensional two-fluid model for the simulation of slug flows. Ph.D. Thesis, Imperial College London. doi:10.25560/6319

MORAES, J.P.O., NIECKELE, A.O., CARNEIRO, J.N.E., 2020. Development and validation of an algebraic slip model for water-in-oil dispersed flow. In 18th Brazilian Congress of Thermal Sciences and Engineering (Online), November 16-20.

NIECKELE, A.O., CARNEIRO, J.N.E., CHUCUYA, R.C., AZEVEDO, J.H.P., 2013. Initiation and statistical evolution of horizontal slug flow with a Two-Fluid Model. ASME J. Fluids Eng. 135 (12), 121302 (11 pages). doi:10.1115/1.4025223.

NIECKELE, A.O., CARNEIRO, J.N.E., 2017. On the numerical modeling of slug and intermittent flows in oil and gas production. In: 36th Int. Conf. Ocean, Offshore and Arctic Eng. OMAE2017. Trondheim, Norway doi:10.1115/ OMAE2017–62407.

NYDAL, O.J., 2012. Dynamic models in multiphase flow. Energy & Fuels 26(7), 4117-4123. Doi: 10.1021/ef300282c

OKAWA, T., KATAOKA, I., 2000. Characteristic and stability of a two-fluid model for bubbly two-phase flow. In: Proceedings of ICONE 8, 8th International Conference on Nuclear Engineering, Baltimore, MD USA, 2-6 April.

ORTEGA, A.J.M., 2004. Análise do Padrão Slug em Tubulações Horizontais Utilizando o Modelo de Dois Fluidos. M.Sc. Dissertation, PUC-Rio, Brazil.

ORTEGA, A.J.M., NIECKELE, A.O., 2005. Simulation of horizontal two-phase slug flows using the two-fluid model with a conservative and non-conservative formulation. In: 18th International Congress of Mechanical Engineering. November 6-11, Ouro Preto, MG, Brazil.

OSHER, S., SETHIAN, J.A., 1988. Fronts Propagating with Curvature- Dependent Speed: Algorithms Based on Hamilton-Jacobi Formulation. Journal of Computational Physics, 79, 12-49. Doi: 10.1016/0021-9991(88)90002-2

OWEN, D., HEWITT, G., 1987. An improved annular two-phase flow model. Proceedings of the 3rd International Conference on Multiphase Flow, the Hague, the Netherlands.

PASQUALETTE, M.A., CARNEIRO, J.N.E., NIECKELE, A.O., JOHANSEN, S.T., 2017. Optimization of the interfacial shear stress for the simulation of horizontal viscous oil-gas flows with the 1D Two-Fluid Model. In: 4th Journeys in Multiphase Flow, São Paulo, Brazil, 27-31 March.

PASQUALETTE, M.A., 2017. Optimization of the interfacial shear stress and assessment of closure relations for horizontal viscous oil-gas flows in the stratified and slug regimes. M.Sc. Dissertation, PUC-Rio, Brazil.

PASQUALETTE, M.A., CARNEIRO, J.N.E., RIBEIRO, G.G., SOPRANA, A.B., GIRARDI, V., BASSANI, G.S., MERINO-GARCIA, D., 2019. 1D Numerical Simulations of Hydrate Formation and Transport in Oil-Dominated Systems with a Population Balance Framework. In: BHR 19th International Conference on Multiphase Production Technology, Cannes, France, June.

PATANKAR, S.V., 1980. Numerical Heat Transfer and Fluid Flow. 1st ed., McGraw-Hill, USA.

PROSPERETTI, A., TRYGGVASON, G., 2007. Computational methods for multiphase flow. 1st ed., Cambridge University Press, USA.

RIBEIRO, J.X.F, LIAO, R., ALIYU, A.M., AHMED, S.K.B., BABA, Y.D., ALMABROK, A.A., ARCHIBONG-ESO, A., LIU, Z., 2021. A Two-Fluid Model for High-Viscosity Upward Annular Flow in Vertical Pipes. *Energies* 14, 3485. Doi:10.3390/en14123485.

ROCHA, P.R.B., 2020. Numerical study of statistically developed gas-liquid intermittent flows by the lens of three-dimensional simulations. M.Sc. Dissertation, PUC-Rio, Brazil.

RODRIGUEZ, J.M., 2009. Numerical Simulation of two-phase annular flow. Ph.D. thesis, Rensselaer Polytechnic Institute Troy, New York.

SANDERSE, B., SMITH, I.E. and HENDRIX, M.H., 2017. Analysis of time integration methods for the compressible two-fluid model for pipe flow simulations. *International Journal of Multiphase Flow*, 95, 155–174. doi: 10.1016/j.ijmultiphaseflow.2017.05.002.

SAXENA, A., PRASSER, H., 2020. A study of two-phase annular flow using unsteady numerical computations. *International Journal of Multiphase Flow*, 126, 103037. doi: 10.1016/j.ijmultiphaseflow.2019.05.003.

SCHUBRING, D., SHEDD, T.A., 2007. Wave behavior in horizontal annular air–

water flow. *International Journal of Multiphase Flow* 34, 636-646. Doi: 10.1016/j.ijmultiphaseflow.2008.01.004.

SERIZAWA, A., KATAOKA, I., 1987. Phase distribution in two-phase flow. *ICHMT International Seminar on Transient Phenomena in Multiphase Flow*, Dubrovnik, Former Yugoslavia.

SIQUEIRA, J.G.C., 2019. Modelagem de gotas dispersas em escoamento anular vertical. M.Sc. Dissertation, PUC-Rio, Brazil.

SIQUEIRA, J.G.C., NIECKELE, A.O., CARNEIRO, J.N.E., 2019. Comparison of droplet entrainment models in 1D numerical simulations of vertical annular two-phase flow. In *10th International Conference on Multiphase Flow (ICMF)*, Rio de Janeiro, Brazil, May 19 – 24.

SONG, J.H.; ISHII, M., 2000a. The well-posedness of incompressible one-dimensional two-fluid model. *Nucl. Eng. Des.* 43, 2221-2231. Doi:10.1016/S0017-9310(99)00287-2.

SONG, J.H.; ISHII, M., 2001a. On the stability of a one-dimensional two-fluid model. *Nucl. Eng. Des.* 204, 2221-2231. Doi: 10.1016/s0029-5493(00)00253-3.

SONG, J.H.; ISHII, M., 2001b. The One-dimensional two-fluid model with momentum flux parameters. *Nucl. Eng. Des.* 205, 145-158. Doi:10.1016/S0029-5493(00)00351-4

SONG, J.H., 2003. The remedy for the ill-posedness of the one-dimensional two-fluid model. *Nucl. Eng. Des.* 222, 40-53. Doi:10.1016/S0029-5493(02)00391-6

STUHMILLER, J., 1977. The influence of interfacial pressure forces on the character of two-phase flow model equations. *Int. J. Multiphase Flow* 3(6), 551-560. Doi:10.1016/0301-9322(77)90029-5

SUN, B., ZHANG, Z., WANG, Z., XIANG, H., 2018. Interfacial Friction Factor Prediction in Vertical Annular Flow Based on the Interface Roughness. *Chemical Engineering Technology* 41(9), 1833-1841. Doi:10.1002/ceat.201800085.

TAITEL, Y., DUKLER, A.E., 1976. A model for predicting flow regime transitions in horizontal and near horizontal gas-liquid flow. *AIChE Journal*, 22(1), 47-55.

TRAPP, J. A., 1986. The mean flow characteristics of two-phase flow equations, *International Journal of Multiphase Flow*, 12, 263-276. Doi: 10.1016/0301-9322(86)90029-7.

VAN LEER, B., 1974. Towards the ultimate conservative difference scheme. II. Monotonicity and conservation combined in a second-order scheme. *Journal of computational physics* 14(4), 361–370.

VASSALO, P., 1997. Velocity and phase distribution measurements in vertical air-water annular flows. KAPL Atomic Power Laboratory, Schenectady, New York.

VASSALO, P., 1999. Near wall structure in vertical air-water annular flows. *International Journal of Multiphase Flow* 25, 459-476.

VERSTEEG, H.K., MALALASEKERA, W., 2007. *An Introduction to Computational Fluid Dynamics: The Finite Volume Method*, Prentice Hall, 2nd Edition.

VON NEUMANN, J., RICHTMEYER, R.D., 1949. A method for the numerical calculation of hydrodynamic shocks. *J. Appl. Physics* 21, 232–237. doi:10.1063/1.1699639.

WALLIS, G.B., 1969. *One-dimensional two-phase flow*. 1st ed., McGraw-Hill, USA.

WANG, Z., GABRIEL, K.S., MANZ, D.L., 2004. The influences of wave height on the interfacial friction in annular gas–liquid flow under normal and microgravity conditions. *International Journal of Multiphase Flow* 30, 1193–1211. Doi: 10.1016/j.ijmultiphaseflow.2004.06.003.

WANG, G., DANG, Z., ISHII, M., 2021. Wave structure and velocity in vertical upward annular two-phase flow. *Experimental Thermal and Fluid Science* 120, 110205. Doi: 10.1016/j.expthermflusci.2020.110205.

WHALLEY, P.; HEWITT, G. F., 1978. The correlation of liquid entrainment fraction and entrainment rate in annular two-phase flow. UKAEA Atomic Energy Research Establishment.

WOLF, A., JAYANTI, S., HEWITT, G.F., 2001. Flow development in vertical annular flow. *Chemical Engineering Science* 56, 3221-3235. Doi:10.1016/S0009-2509(00)00546-7.

WOODMANSEE, D.E., HANRATTY, T.J., 1969. Mechanism for the removal of droplets from a liquid surface by a parallel air flow. *Chemical Engineering Science* 24, 299-307. doi:10.1016/0009-2509(69)80038-2.

WROBEL, J.R., MCMANUS, H.N., 1961. An analytic study of film depth, wave height, and pressure drop in annular two-phase flow. *Develop. Mech.* 1, 578–58.

ZHAO, Y.; MARKIDES, C. N.; MATAR, O. K.; HEWITT, G. F., 2013. Disturbance

wave development in two-phase gas-liquid upwards vertical annular flow. *Int. J. Multiphase Flow*, 55, 111–129. doi: 10.1016/j.ijmultiphaseflow.2013.04.001.

Appendix A

In this section, the procedure to calculate the equilibrium film height from the superficial velocities and fluid properties is outlined

- (i) From the superficial velocities, estimate α_G

$$\alpha_G = \frac{U_{sG}}{U_{sG} + U_{sL}} \quad (\text{A.1})$$

- (ii) From α_G , calculate an estimate for h_L and define a $dh_L = 1e^{-6}$

- (iii) Calculate the residual for h_L

- a) From Eqs. (3.9) to (3.11), calculate the geometrical parameters in terms of h_L
- b) Calculate phase velocities, Reynolds number, friction factors, and shear stresses
- c) Solve the equation below to obtain the residue

$$res = (\rho_L - \rho_G)g \sin \beta - \frac{\tau_L S_L}{A_L} - \frac{\tau_i S_i}{A} \left(\frac{1}{\alpha_L} + \frac{1}{\alpha_G} \right) \quad (\text{A.2})$$

- (iv) Repeat step (iii) for $h_L + dh_L$, obtaining a new residual $dres$

- (v) Calculate the residual variation with $dr/dh_L = (dres - res)/dh_L$

- (vi) Update $h_L = h_L^o - res/(dr/dh_L)$

- (vii) Check physical limits

- a) $h_L > D$
- b) $h_L < 0$

- (viii) Repeat step (iii) for the new h_L

- (ix) Check residuals

- a) If $res < 1e^{-6}$, go to
- b) If $res \geq 1e^{-6}$, go to (iii)

- (x) Finish

Appendix B

The current section outlines the procedure to obtain the statistical quantities from the numerical simulations of section 7.3.

B.1. Group velocity

As shown in Fontalvo (2016), the group velocity is calculated through the cross correlation of the time signal of the liquid film. First, two positions x_1 and x_2 are defined, then, a timeseries from each position is obtained (Figure B.1). With both time signals, the cross correlation can be calculated.

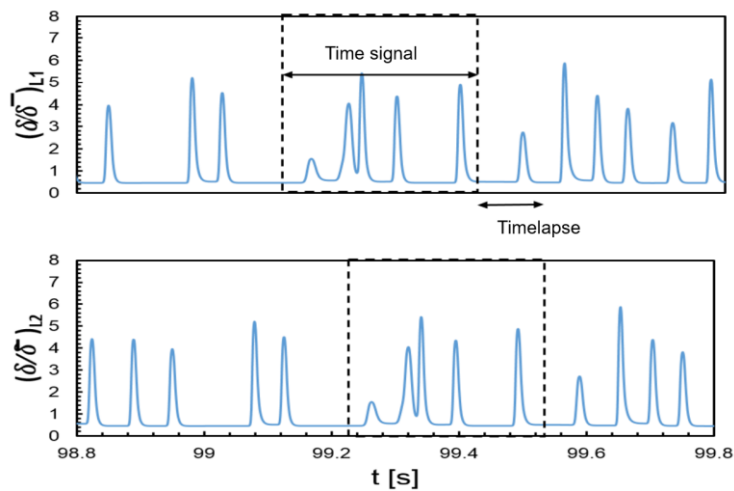


Figure B.1- Time signal delay from two probe positions. Fontalvo (2016).

From the cross-correlation data, the time delay can be extracted from the peak of the $R_{x,y}$ timeseries, which is associated to the temporal offset Δt that grants the highest correlation between the two signals. From the delay, one can obtain the structure velocity from the following equation

$$C_w = \frac{x_2 - x_1}{\Delta t} \quad (\text{B.1})$$

We note that the distance between x_1 and x_2 is very important to correctly evaluating of the cross-correlation. The distance must be large enough not to generate a very small time delay and narrow enough in order for the time signals in both probes to be sufficiently similar (the waves may coalesce and significantly

alter the structure of the group).

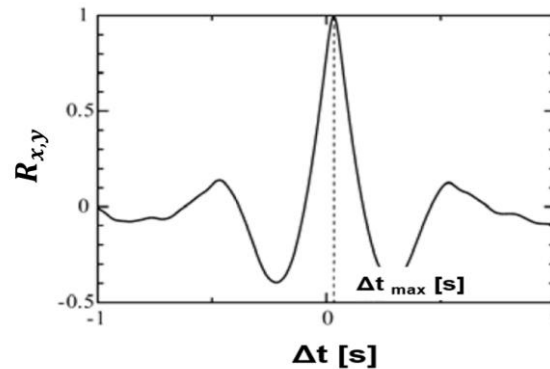


Figure B.2- Cross-correlation signal. Fontalvo (2016).

B.2. PSD Spectrum

The PSD is the Power Spectral Density of the signal, which calculates the amount of power/energy content for each frequency of the spectrum. It can be obtained from the Welch periodogram. For this, we rely on the fast Fourier transform (*fft*) of the liquid film thickness signal. As mentioned in Section 6.5, the sampling frequency f_s of the simulations' data acquisition time is of 1kHz. The spectrum spans from 0Hz to the Nyquist frequency, i.e., $f_s/2$. The Welch methodology proposes the *fft* to be performed to individual smaller time signals blocks, with an overlap. In that way, the obtained spectrum is smoother. From the PSD spectrum (Figure B.3), the dominant frequency ν_{PSD} is obtained as the frequency associated with the peak of the spectrum.

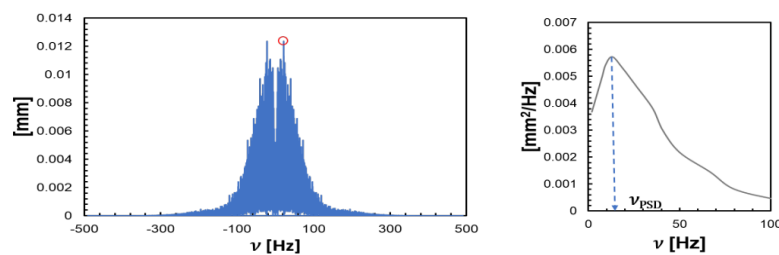


Figure B.3- PSD spectrum and dominant frequency. Fontalvo (2016).

Appendix C

The following section presents the stability analysis results omitted from Chapter 7 for brevity. The dynamic pressure model test was carried out using the configuration II-Zhao-2 as a representative case. The momentum flux parameter test was performed for the I-Kaji-1 case. The remaining cases are shown here.

C.1. Dynamic Pressure model test

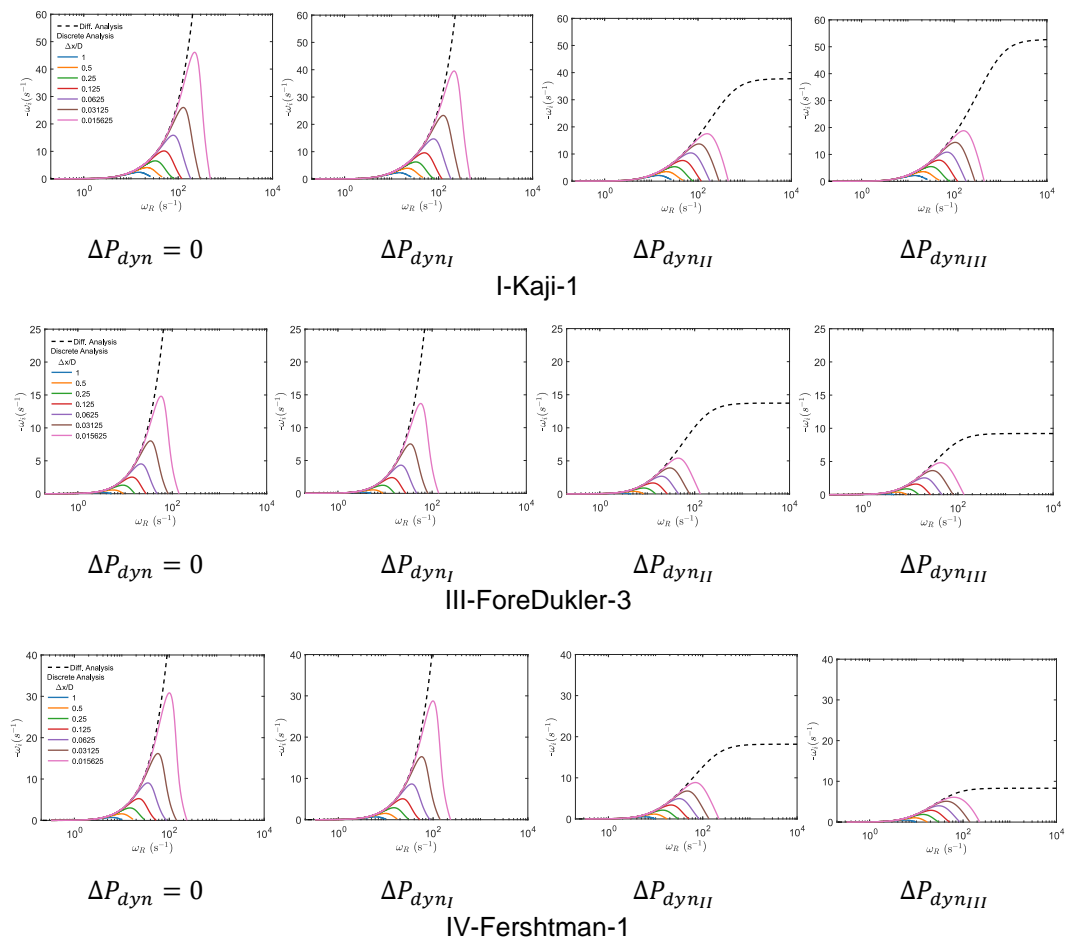


Figure C.1- Stability Analysis: Dynamic Pressure model test.

C.2. Momentum flux parameter test

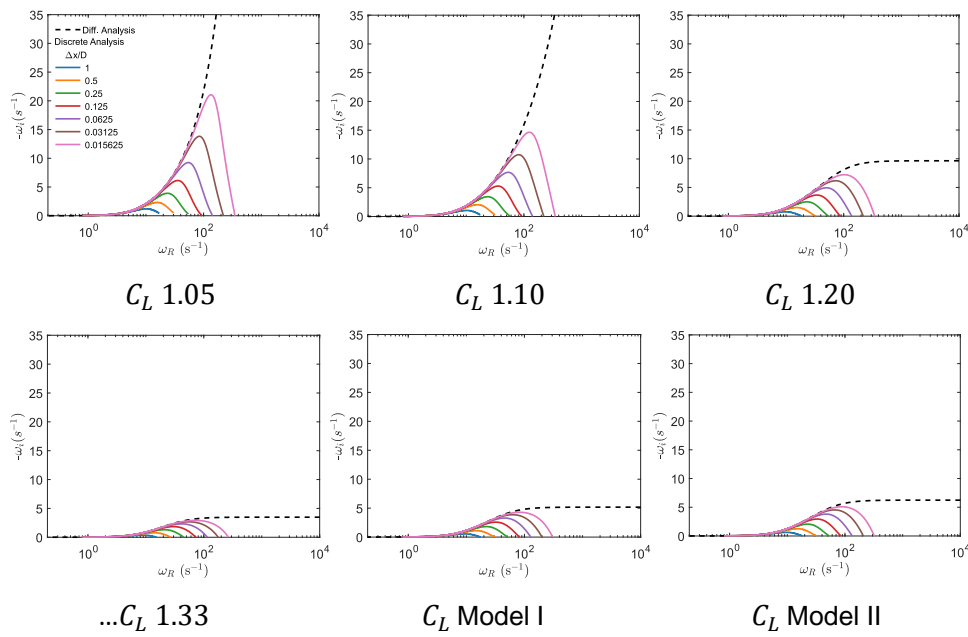


Figure C.2- Stability Analysis: Momentum flux parameter test. II-Zhao-2

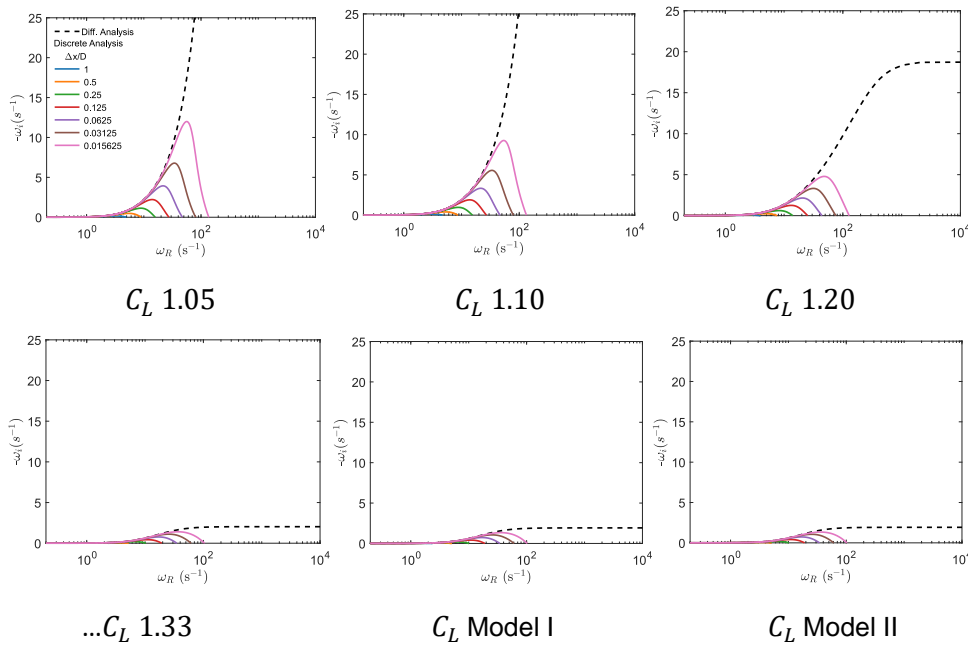


Figure C.3- Stability Analysis: Momentum flux parameter test. III-ForeDukler-3

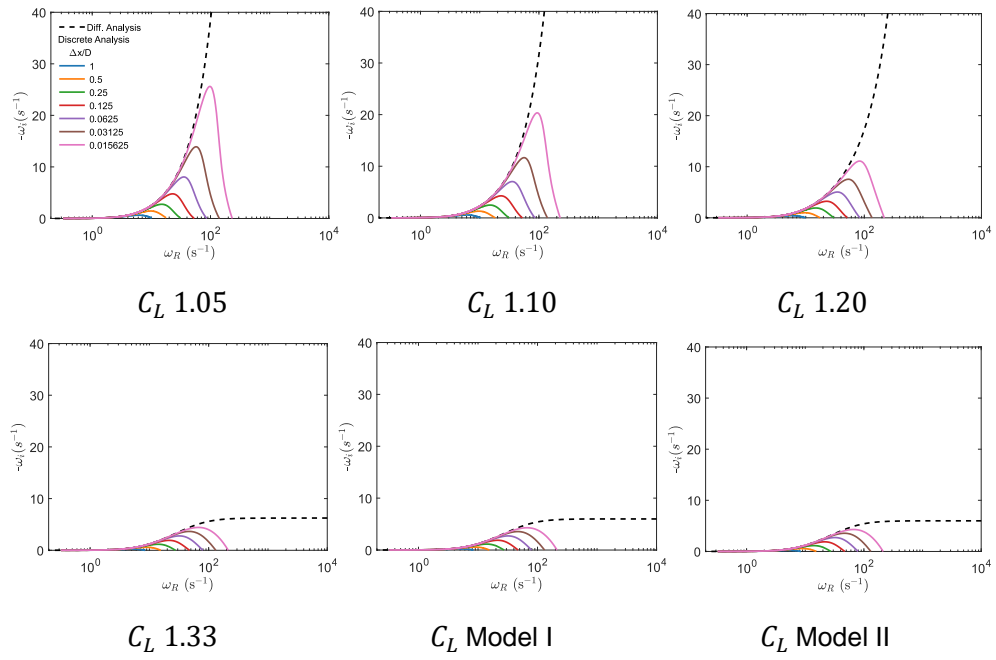


Figure C.4- Stability Analysis: Momentum flux parameter test. IV-Fershtman-1

C.3. Numerical versus Experimental test for the local film thickness

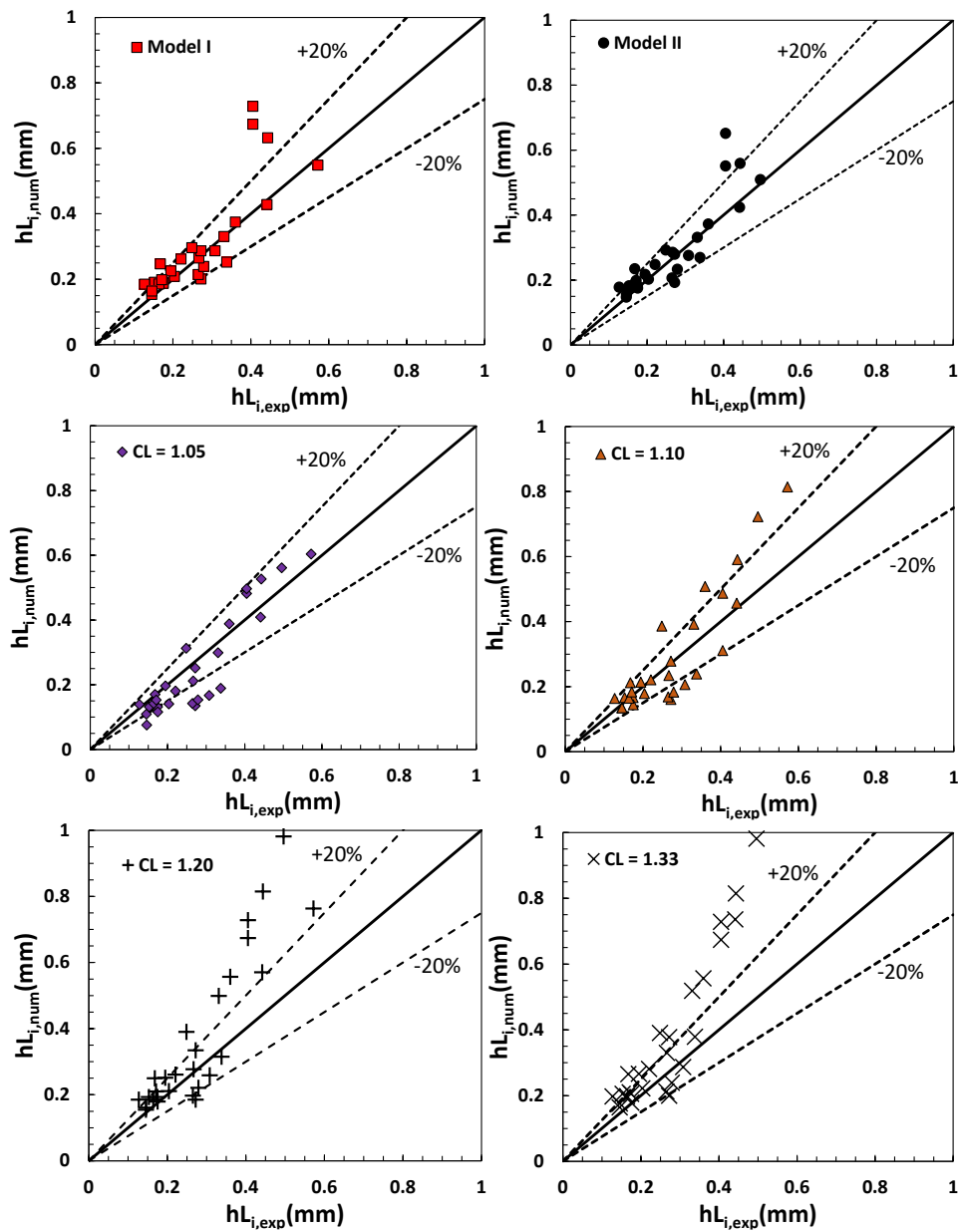


Figure C.5- Numerical Analysis: Experimental vs Numerical plot for instantaneous liquid film thickness at the probe location closest to the exit.